博士論文

Electrode design and reaction analysis of electrochemical promotion of ammonia synthesis using protonic ceramic fuel cells

（プロトン伝導性セラミック燃料電池を用いたアンモニア合成の電気化学的促進に対する電極設計と反応解析）

李　建毅

Chien-I Li

Contents

1. Background

1.1. **Development of renewable energy in the world**

In recent years, with rapidly developing industry, the annual carbon emission into the atmosphere has increased from 19.4 in 1980 to 36.2 billion tons in 2017.[1] Compared to 1980, the global average temperature increased by approximately 0.7°C in 2018 due to large amounts of CO_2 emission.[1] According to the Intergovernmental Panel on Climate Change (IPCC), if the global average temperature increases by 1.5°C, it results in serious alterations to human and natural systems, including extreme weather, climate change, and sea-level rise.[2] Therefore, to reduce carbon emissions, developed countries have been developing renewable energies, such as hydropower, wind energy, and solar energy to replace fossil fuels.[3]

The International Renewable Energy Agency (IRENA) reported that the total renewable energy production increased by around 160% from 2009 to 2017.[3] However, the instability of renewable energy supply is a significant issue because it depends on the weather or atmospheric conditions. The unreliable supply may cause systems to run out of electricity and broke or reduce the reliability of the system. To solve this problem, scientists are developing an alternative route to store renewable energy by transferring electricity from an excess of renewable energy to chemicals of hydrogen carriers, such as hydrogen, methane, and ammonia.

1.2. **Role and types of hydrogen carriers**

Although the electricity from renewable energy can be transferred into hydrogen carriers, the limitation of physical properties (e.g. boiling point) of hydrogen carriers affects the cost of storage, transport, and utilization. Hydrogen carriers include several chemicals, such as hydrogen gas, hydrocarbons (methane and methanol), and ammonia, whose volumetric and gravimetric energy density are shown in Table 1-1.[4] Although hydrogen gas has the highest gravimetric energy density, the volumetric energy density is relatively low even at 700 bar. For natural gas or methanol, the volumetric energy and gravimetric energy densities are moderate, but they will produce carbon emissions when they are combusted. Ammonia also has moderate volumetric and gravimetric energy density. Furthermore, the advantages, including liquefication at low pressure for easy storage, non-carbon emissions, and no explosion, make ammonia have potential as an alternative choice of hydrogen carrier.

In addition, ammonia is a multi-functional chemical. Ammonia is an essential chemical in agriculture as a fertilizer.[1] With population increasing in the world, the demand for ammonia production also increases every year. Ammonia can also be used for removing nitric oxide by a reduction reaction. Lastly, due to its good chemical stability and high energy density, ammonia is considered as an energy carrier in the ShipFC project, which is run by a consortium of 14 European companies and institutions.[5]

1.3. Introduction of ammonia production process

1.3.1. Haber-Bosch Process

Currently, ammonia is fabricated by the Haber−Bosch process (> 96% of ammonia is produced by this route), in which N_2 and H_2 react to form NH_3 over Fe−based catalysts at high temperature and high pressure (Eqs. 1-1−1-5).[6] The reaction is followed by a dissociative mechanism, which is described by the following equations:

$$N_2\,(g) + * \rightarrow N_2* \qquad 1\text{-}1$$

$$N_2* + * \rightarrow 2N* \qquad 1\text{-}2$$

$$H_2\,(g) + 2* \rightarrow 2H* \qquad 1\text{-}3$$

$$N* + 3H* \rightarrow NH_3\,(g) + 4* \qquad 1\text{-}4$$

$$\text{Overall reaction: } N_2\,(g) + \frac{3}{2}H_2\,(g) \rightarrow NH_3\,(g) \qquad 1\text{-}5$$

Firstly, the N_2 molecules adsorb on the Fe surface and dissociate to 2N*, and then the N* react with H* from H_2 to form NH_3 on the Fe surface.[7, 8] Previous studies indicated that the rate-determining step was considered as the dissociation of N_2* into 2N* on the catalyst surface (a two-phase boundary) (Eq. 1-2).[9, 10] In the previous study, the ammonia formation rates of 250 μg mg^{-1}_{Fe} h^{-1} at 7 MPa and 976 μg mg^{-1}_{Fe} h^{-1} at 10 MPa were reported.[8] Nowadays, the production rate of an ammonia formation plant can reach around 1500 tons/day. However, the drawback of the Haber−Bosch process is the carbon emissions. The feedstock N_2 is obtained by air separation, whereas the feedstock H_2 is produced through the steam methane reforming method, which releases a large amount of CO_2.[6] It is estimated that the Haber-Bosch process releases 1.5–1.6 t_{CO2} t_{NH3}^{-1}, which contributes to 1.2% of the global CO_2 emission every year.[11, 12]

The technology for the Haber-Bosch process has been developed for around a century. Before the 1970s, the energy consumption was between 40−60 GJ t_{NH3}^{-1} when ammonia was formed using coal as feedstock. With the introduction of the steam methane reforming process, the energy consumption decreased to around 30 GJ t_{NH3}^{-1}. Since the 1990s, the improvements in energy consumption of the Haber-Bosch process with the steam methane reforming have slowed down to 27.4–31.8 GJ t_{NH3}^{-1}.[6] To reduce the carbon emissions and energy consumption for ammonia formation, scientists have developed the process of electrochemical ammonia synthesis, in which H_2O and N_2 react to form ammonia using proton-conductive fuel cells.[13]

1.3.2. Electrochemical Synthesis of Ammonia

To reduce the carbon emissions during ammonia formation, the electrochemical process of ammonia formation integrated with renewable energy was proposed. The process of electrochemical ammonia formation can be divided into two types: 1) direct electrochemical reaction of ammonia synthesis using proton-conductive fuel cells with N_2 and H_2O (case 1 in Fig. 1-1); 2) indirect electrochemical of ammonia synthesis using proton-conductive fuel cell with N_2 and H_2 (case 2 in Fig. 1-2). The reactions are described by the following equations:

Case 1

Anode: $H_2O\,(g) \rightarrow 1/2O_2\,(g) + 2H^+ + 2e^-$ 1-6

Cathode: $N_2\,(g) + 6H^+ + 6e^- \rightarrow 2NH_3\,(g)$ 1-7

Overall: $3H_2O\,(g) + N_2\,(g) \rightarrow 2NH_3\,(g) + 3/2O_2\,(g)$ 1-8

Case 2

Anode: $H_2\,(g) \rightarrow 2H^+ + 2e^-$ 1-9

Cathode: $N_2\,(g) + 6H^+ + 6e^- \rightarrow 2NH_3\,(g)$ 1-7

Overall: $N_2\,(g) + \frac{3}{2}H_2\,(g) \rightarrow NH_3\,(g)$ 1-5

In case 1, the reactor must have two compartments, where N_2 and H_2O are flowed into the cathode and the anode, respectively. In the anode, H_2O decomposed to protons, oxygen, and electrons. The protons pass through the proton-conductor electrolyte to the cathode and react with nitrogen molecule to form NH_3 via a charge-transfer reaction at a triple phase boundary (TPB),

which is between gas, proton-conductor, and electrical conductor. The charge-transfer reaction is similar to that electrochemical reaction of oxygen ion, hydrogen gas, and electrons in the anode in solid oxide fuel cells.[14]

In case 2, to reduce the carbon emission, the hydrogen feedstock in case 2 need to be supplied by water electrolysis and renewable energy. Therefore, two reactors, one is for water electrolysis and the other is for electrochemical ammonia formation, are necessary in case 2. A mixture of N_2 and H_2 formed by water electrolysis is flowed into the single compartment reactor of ammonia electrosynthesis. Notably, the reactions in case 2 for ammonia formation involve the surface reaction on the Fe surface (Eq. 1-5) and charge-transfer reaction at TPB in case 2 (Eq. 1-9). The mechanism of the surface reaction in case 2 is the same as that in the Haber-Bosch process (Eqs. 1-1−1-5). And the mechanism of charge-transfer reaction in case 2 is the same as that in case 1, in which protons react with nitrogen gas and electron at the TPB.

Fig. 1-3 shows the Gibbs free energy and required voltage for Eqs. 1-5 (case 1) and 1-8 (case 2). Ammonia formation from N_2 and H_2O is a nonspontaneous reaction ($\Delta G > 0$), whereas that from N_2 and H_2 is a spontaneous reaction below 450K. Electrochemical ammonia formation requires an applied voltage of 1.12 V at ambient temperature in case 1, and the required voltage increases with increasing the operating temperature. In case 2, the required voltage is around 0.1 V at 450°C, which is much lower than that in case 1 because the reaction in case 1 requires extra energy for water electrolysis.

However, to date, the low ammonia formation rate and low current efficiency are still issues. Whether in case 1 or 2, by-product H_2 via the hydrogen evolution reaction (Eq. 1-10) occurs in the cathode, and it causes a low current efficiency of ammonia formation because the required potential for H_2 evolution reaction is lower than that for electrochemical ammonia formation.[15]

$$2H^+ + 2e^- \rightarrow H_2\,(g) \qquad 1\text{-}10$$

In the next section, the performance of ammonia formation in previous studies will be introduced.

1.4. State-of-arts for electrochemical reaction of ammonia synthesis

1.4.1. Electrochemical of ammonia synthesis with pure N_2 in cathode

Although it is difficult for direct N_2 cleavage to occur on the catalyst surface at ambient temperature because of insufficient kinetics, previous studies pointed out based on density

functional theory (DFT) calculations that N_2 bonding can be broken at ambient temperature via an associative mechanism with cathodic polarization, which is represented by Eqs. 1-11−1-12 .[15, 16] In the associative mechanism, ammonia is formed via the charge-transfer reaction at the TPB. The electrochemical ammonia reaction can be divided according to three different operating temperatures based on the electrolysis system and selected electrolyte.

Low temperature (*T* < 100°C)

$$N_2\,(g) + 3H^+ + 3e^- + * \rightarrow N* + NH_3\,(g) \qquad 1\text{-}11$$

$$N* + 3H^+ + 3e^- \rightarrow NH_3\,(g) \qquad 1\text{-}12$$

Table 1-2 reports the previous studies about the electrochemical reaction of ammonia synthesis at low temperature (*T* < 100°C). The used electrolyte can be divided into the aqueous electrolyte, non-aqueous, and polymer electrolyte membrane. Aqueous electrolytes, including HCl, phosphate buffer solution (PBS), NaOH, KOH, $LiClO_4$, $NaClO_4$, $KClO_4$, Na_2SO_4, and Li_2SO_4, were used for the N_2 reduction reaction.[17-40] The pH of electrolyte solution plays an important role in the N_2 reduction reaction. Wang et.al reported the effect of pH on ammonia formation by comparing the performance in acidic (0.05 M H_2SO_4), neutral (0.1 M PBS), and alkaline (0.1 M NaOH) electrolytes.[18] They found that neutral electrolytes had the highest ammonia formation rate and current efficiency but with relatively lower current densities than acidic and alkaline electrolytes because of the high resistance to mass transfer and charge-transfer reaction, i.e., hydrogen evolution reaction, in the neutral electrolyte. However, low current efficiencies in the acidic and alkaline aqueous electrolyte are caused by the active hydrogen evolution reaction. In addition, low N_2 solubility is another issue in the aqueous system.

Non-aqueous electrolytes show a better performance of the electrochemical reaction of ammonia synthesis than aqueous because they have advantages like high nitrogen solubility and low activity for the hydrogen evolution reaction. Most non-aqueous electrolytes, 2-propanol, [P6,6,6,14][eFAP], [C4mpyr][eFAP], $FPEE^+$[C4mpyr][eFAP], and EDA, show a high current efficiency (>10%).[41-44] On the other hand, previous studies also reported proton or anion exchange membrane used for ammonia formation.[45-50] A high ammonia formation rate (10^{-9} mol cm^{-2} s^{-1}) is achieved. However, a disadvantage of possible by-production of hydrazine by the nitrogen reduction reaction occurs at low temperature.[51].

Intermediate temperature (100°C < *T* < 400°C)

Table 1-3 contains the previous studies about the electrochemical reaction of ammonia synthesis at intermediate temperature (100°C < *T* < 400°C). At this temperature, molten salt electrolytes (KOH-NaOH and KCl-NaCl-CsCl) are usually used for the electrochemical reaction of ammonia synthesis.[52-59] The reaction mechanism using molten salt electrolytes is that nitride ions (N^{3-}) are formed by reduction reaction in molten salts, and they subsequently react with hydrogen or water to form ammonia. On the other hand, phosphate-based proton-conducting electrolytes, such as CsH_2PO_4 and SiP_2O_7, are also applied for the electrochemical reaction of ammonia synthesis.[57, 60, 61] Kishira et al. reported an ammonia formation rate of 10^{-10} mol s^{-1} cm^{-2} using Ru-based catalysts on carbon and noble metals (Ag-Pd and Pt) as cathodes with N_2 in the cathode and H_2 in the anode. However, when H_2 is replaced by steam in the anode, the ammonia formation rate drops by one order of magnitude to 10^{-11} mol s^{-1} cm^{-2}.

High temperature (*T* > 400°C)

Table 1-4 shows the results from previous studies about the electrochemical reaction of ammonia synthesis at high temperature (*T* > 400°C). The electrochemical reduction of N_2 to NH_3 at high temperatures was investigated using a variety of catalysts including metals and cermet electrodes.[13, 62-83] Notably, noble metals and ceramic catalysts exhibit a similar ammonia formation rate of approximately 10^{-9} mol s^{-1} cm^{-2}. On the other hand, the proton conductivity of the electrolytes also plays an important role in the electrochemical reaction of ammonia synthesis. Ma et al. reported the relationship between ammonia formation rate and the proton conductivity by using various electrolytes such as $BaCe_{1-x}Dy_xO_3$, $BaCe_{1-x}Ca_xO_3$, and $BaCe_{1-x}Gd_xO_3$.[82-84] High proton conductivities show better performance of ammonia formation than that using low proton conductivities. In addition to H^+ supply from the anode, Kosaka et al. also reported that the rate-determining step of N_2 dissociation can be accelerated by cathodic polarization using a Ru-based catalyst.[75, 77] However, a previous study reported that the hydrogen coverage surface at high applied voltage hinders N_2 molecule adsorption and NH_3 formation using Ru catalyst due to the hydrogen poisoning.[75]

1.4.2. Electrochemical synthesis of ammonia in gaseous mixture H_2 and N_2 in cathode

The composition of flow gas in the cathode also plays an important role in the electrochemical reaction. The performance of electrochemical ammonia synthesis has also been investigated by introducing a gaseous mixture of H_2–N_2 into the cathode.[62, 70, 72, 74, 76] Generally, the ammonia formation rate in a gaseous mixture of H_2–N_2 is higher than in pure N_2 because the H_2 in the cathode acts as an additional source of ammonia formation. For example, Ouzounidou et al. reported that a low ammonia formation rate using Fe catalyst (6×10^{-12} mol s^{-1} cm^{-2}) in pure N_2, whereas the rate increased to approximately 1.1×10^{-11} mol s^{-1} cm^{-2} in 4% H_2−62% N_2.[62] Notably, they also reported that the current efficiency of the electrochemical reaction of ammonia synthesis is over 100%, suggesting that the mechanism of electrochemical ammonia formation is probably followed by the electrochemical promotion of catalyst (EPOC) effect (i.e. non-Faradaic process). J. Díez-Ramírez et al. also reported another result to support that the electrochemical promotion was dominated by EPOC using K^+−Al_2O_3 as electrolyte and Co_3Mo_3N as cathode.[85] Here, when the supply of H^+ from the anode was replaced by K^+, the ammonia formation rate increased from 10.2 to 13.6 μg h^{-1} mg^{-1} with cathodic polarization in H_2−N_2 atmosphere in the cathode, which also agrees with the result. Vayenas et al. proposed that the effect of EPOC on reaction rate is caused by a change of the work function of metal catalyst with cathodic or anodic polarization by an effective double layer, in which a gas–solid system could be formed via spillover of mobile ions originating from charge carriers in the electrolyte.[86-88] The increase or decrease in metal work function by the effective double layer could promote the electron donation/backdonation reaction and improve the reaction rate.

In our previous study, Kosaka et al. reported a similar result using the electrolyte-supported cell of Pt |$BaCe_{0.9}Y_{0.1}O_3$ (BCY)| Al–K–Fe–BCY. A low ammonia formation rate (5.5×10^{-12} to 2.4×10^{-11} mol s^{-1} cm^{-2}) was observed in pure N_2, whereas when a gaseous mixture of 15% H_2–85 %N_2 was supplied to the cathode side, a significant increase in the ammonia formation rate from 2.8×10^{-11} to 6.7×10^{-10} mol s^{-1} cm^{-2} was obtained with cathodic polarization at 650°C.[74] However, for a gaseous mixture of H_2–N_2 in the cathode, it is unclear whether the electrochemical promotion is caused by a dissociative mechanism (Eqs. 1-1−1-5) (i.e., non-Faradic process without charge-transfer reaction), which accelerates N_2 dissociation on the Fe surface (Eq. 1-2), or by a proton-assisted associative mechanism (i.e., Faradic process with charge-transfer reaction), which promotes the charge-transfer reaction of N_2* at the TPB (Eqs. 1-11−1-12).

1.5. **Research objectives**

With the demands of ammonia for agriculture and energy carriers increasing every year, to reduce the CO_2 emissions during ammonia synthesis, the electrochemical reaction of ammonia synthesis in decentralized and small-scale plants can replace the conventional Haber−Bosch process. In this thesis, the mechanism of electrochemical ammonia formation is discussed using proton-conductive fuel cells by using different cathode structures, i.e., cermet structures with long TPB length and metal structures with short TPB length, kinetic analysis, and deuterium isotope analysis using FTIR. Then, to achieve highly efficient electrochemical process of ammonia formation, the energy efficiency for the electrochemical process is discussed. The single compartment reactor, operating with a gaseous mixture of N_2 and H_2, was considered to achieve a higher ammonia formation rate as compared to the dual compartment reactor. The discussions on reaction mechanism and energy consumption presented in this thesis can help improve the design of cathode structures and reactors for ammonia formation processes.

The structure of this thesis is described as below:

Chapter 2 reports the experimental methods used for powder synthesis, cell preparation, characterization, and device for ammonia formation.

In chapter 3, the mechanism of electrochemical ammonia formation was investigated by comparing the performances using different cathode structures. The cathodes include Fe−BCY, W−Fe−BCY, and porous pure Fe cathodes. Also, the influence of the amount of Fe on the performance is investigated.

In chapter 4, based on the result in chapter 3, the detailed performance for porous pure Fe cathode was discussed. The effects of the composition and flow rate of the cathode gas on the performance of ammonia formation were examined. Furthermore, the reaction orders of hydrogen and nitrogen were investigated in the electrochemical reaction by kinetic analysis.

In chapter 5, the mechanism of electrochemical ammonia formation was examined via the deuterium isotope analysis with FTIR in different atmospheres. In this chapter, the contributions of surface reaction and charge-transfer reaction to ammonia formation are shown with the deuterium isotope analysis. Through the observation of ammonia compositions ($NH_{3-x}D_x$), the dominating reaction mechanism in the electrochemical ammonia formation was investigated.

In chapter 6, based on the results in chapters 3-5, a possible mechanism of EPOC was proposed to explain the behavior of electrochemical ammonia formation. Furthermore, comparing the

performance for porous pure Fe and 10Fe−BCY cathodes, two possible reaction mechanisms were proposed.

Chapter 7 shows a process diagram for case 1 and case 2 with an ammonia production of 100 tons/ day using continuous stirred-tank reactor. The energy consumptions for case 1, case 2, and the Haber-Bosch process were compared. This result can significantly help the reactor designing and has the potential to be implemented.

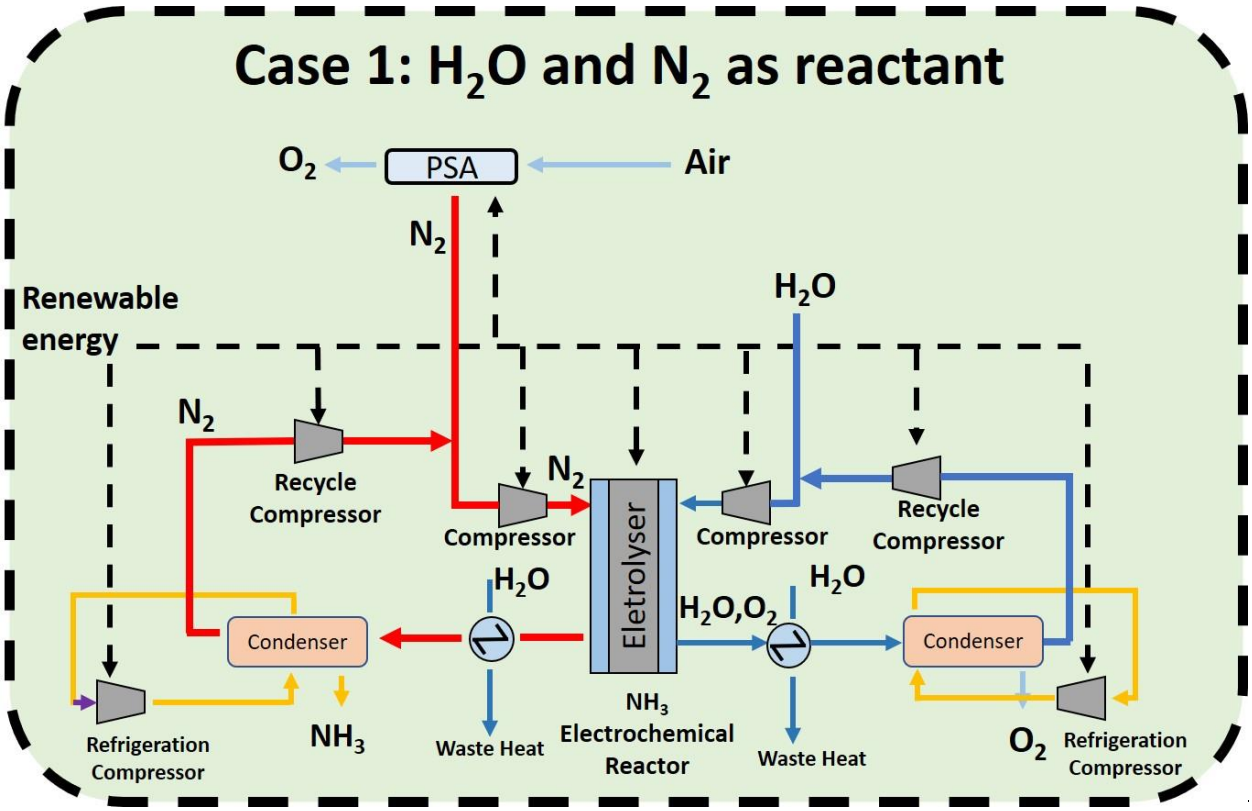

Fig. 1-1 A schematic diagram for case 1. Yellow lines are process gas, dark blue lines are water/steam, light blue lines are air, purple lines are ammonia, and dash gray lines are electricity.

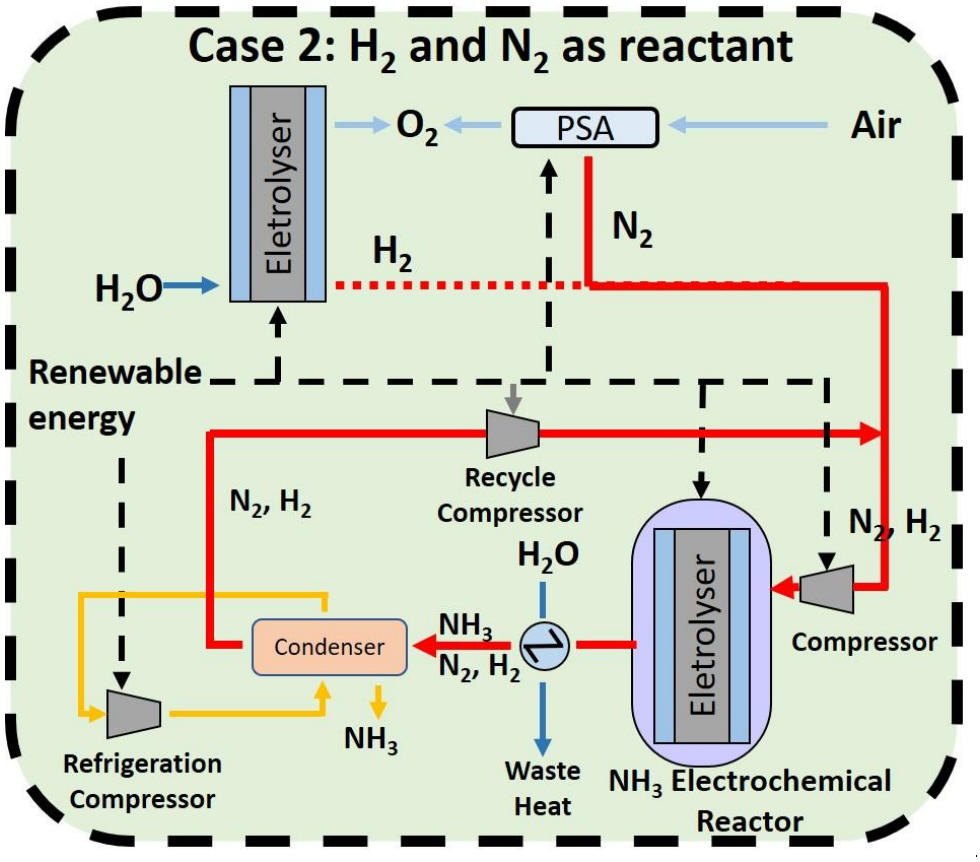

Fig. 1-2 A schematic diagram for case 2. Yellow lines are process gas, dark blue lines are water/steam, light blue lines are air, purple lines are ammonia, and dash gray lines are electricity.

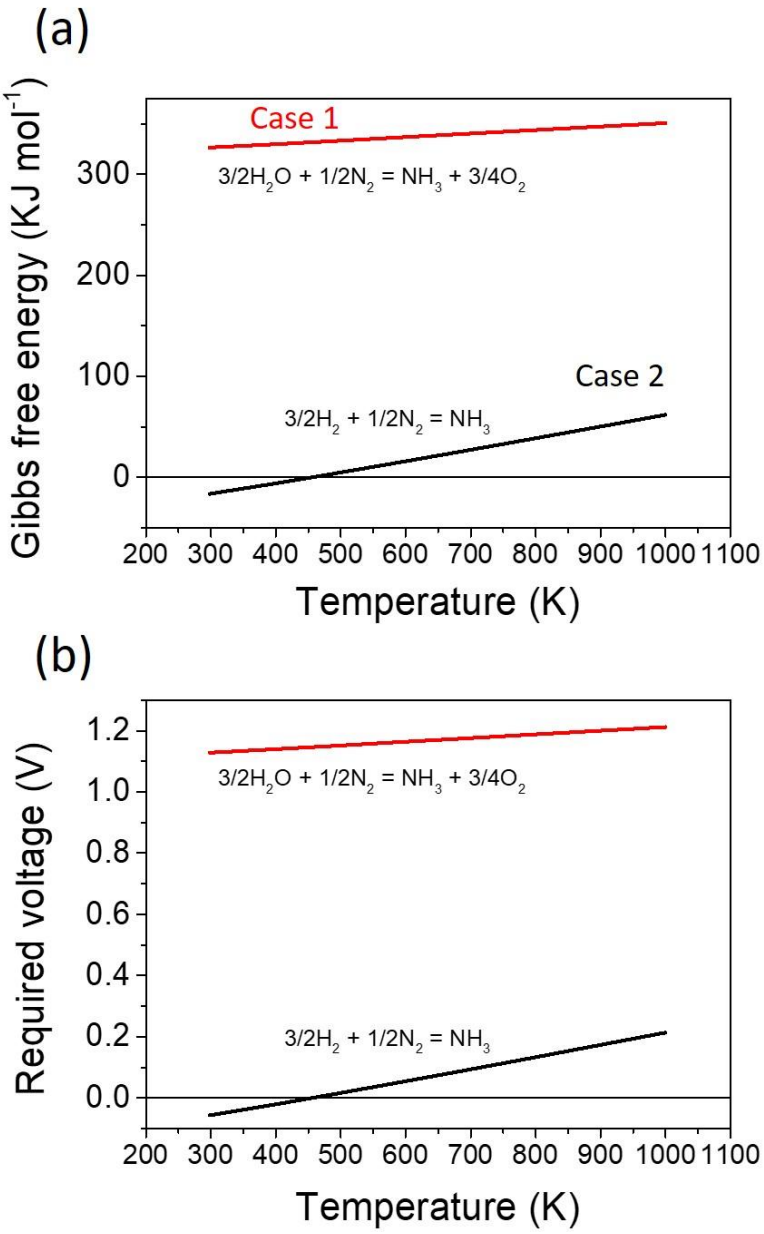

Fig. 1-3 (a) Gibbs free energy and (b) required voltage for ammonia formation reactions in case 1 and case 2. In case 1, ammonia was formed using H_2O and N_2 as reactants. In case 2, H_2, which was from water electrolysis, and N_2 were used to form ammonia.

Table 1-1 Energy densities for different energy carriers.

	Gravimetric energy density (MJ/kg)	Volumetric energy density (MJ/L)
Hydrogen (liquid)	141.9	10
Hydrogen (700 bar)	141.9	5.3
Hydrogen (at STP)	141.9	0.01
Methane (200 bar)	55.6	10
Diesel	45.6	38.6
Methanol	19.7	15.6
Ammonia (liquid)	18.6	11.5

Table 1-2 The performance and condition of ammonia formation at low temperature. The number after the cathode refers to the reference.

Cathode	Electrolyte	T (°C)	r_{NH3} (mol s^{-1} cm^{-2})	r_{NH3} (μg h^{-1} mg^{-1})	Flow rate (sccm)	Atmo-sphere (cathode/ anode)	Current effi-ciency (%)	Year
$SmBaCuFeO_5$ (SBCF)[49]	Nafion	80	6.9×10^{-9}	-	30	N_2/H_2	-	2010
$SmBaCuCoO_5$ (SBCC)[49]	Nafion	80	7.2×10^{-9}	-	30	N_2/H_2	-	2010
Fe[89]	AEM	50	3.8×10^{-12}	-	-	N_2/-	41	2015
Porous Ni[42]	2-propanol	25	1.5×10^{-11}	-	1000	N_2/-	0.9	2016
Ni[43]	0.1 M LiCl/EDA	25	3.6×10^{-11}	-	-	N_2/-	17.2	2016
Au nanorods[17]	0.1 M KOH	25	4.6×10^{-10}	-	-	N_2/-	4.1	2017
a-Au/CeOx-RGO[23]	0.1 M HCl	25	-	8.3	-	N_2/-	10.1	2017
c-Au/CeO_x-RGO[23]	0.1 M HCl	25	-	3.5	-	N_2/-	3.7	2017
poly(N-ethyl-benzene-1,2,4,5-tetracar-boxylic diimide) (PEBCD)[27]	0.5 M Li_2SO_4	25	3.3×10^{-11}	-	-	N_2/-	2.9	2017
FTO[41]	[P6,6,6,14][eFAP]	25	8.2×10^{-12}	-	-	N_2/-	60	2017

SS[41]	[C4mpyr][eFAP]	25	2.3×10^{-11}	-	-	N_2/-	30	2017
MOF(Fe)[45]	Nafion-117	90	2.1×10^{-9}	-	15	N_2/-	1.4	2017
Fe/CNT[46]	Nafion	25	3.6×10^{-12}	-	10	N_2/-	<0.1	2017
γ-Fe_2O_3[47]	Anion exchange membrane	65	4.5×10^{-14}	1.0	200	N_2/-	<0.1	2017
Au/TiO_2[33]	0.1M HCl	25	–	21.4	-	N_2/-	8.1	2017
Au/TiO_2[33]	0.1M HCl	60	–	31	-	N_2/-	13.5	2017
Mo[31]	0.5 M H_2SO_4	80	3.1×10^{-11}	–	10	N_2/-	0.7	2017
Fe_2O_3-CNT N doped [50]	Nafion	25	1.9×10^{-11}	–	20	N_2/-	0.3	2017
Pd/C[18]	0.1 M PBS	25	-	4.5	10	N_2/-	8.2	2018
Au/C[18]	0.1 M PBS	25	-	0.3	10	N_2/-	1.2	2018
Pt/C[18]	0.1 M PBS	25	-	0.3	10	N_2/-	0.2	2018
Pd/C[18]	0.1 M NaOH	25	-	2.1	10	N_2/-	<0.1	2018
Pd/C[18]	0.05 M H_2SO_4	25	-	2.5	10	N_2/-	<0.1	2018
Rh nanosheet[19]	0.1 M KOH	25	6.2×10^{-11}	23.9	200-1000	N_2/-	0.2	2018
Zn[20]	0.1 M KOH	25	9.4×10^{-10}	-	20	N_2/-	10.2	2018

Zn[20]	0.1 M KOH	60	2×10^{-9}	-	20	N_2/-	-	2018
CNS (nitrogen-doped carbon nanospikes)[21]	0.25 M $LiClO_4$	25	1.6×10^{-9}	-	20	N_2/-	11.5	2018
CNS (nitrogen-doped carbon nanospikes)[21]	0.25M $NaClO_4$	25	7.5×10^{-10}	-	20	N_2/-	6	2018
CNS (nitrogen-doped carbon nanospikes)[21]	0.25M $KClO_4$	25	3.3×10^{-10}	-	20	N_2/-	2.5	2018
$Bi_4V_2O_{11}$ / CeO_2[22]	0.1M HCl	25	-	23.2	-	N_2/-	10.2	2018
VN/CC[24]	0.1M HCl	25	2.4×10^{-10}		-	N_2/-	3.6	2018
Ru[26]	0.01M HCl	25	9.0×10^{-12}	-	-	N_2/-	5.4	2018
Ru[26]	0.01M HCl	60	3.5×10^{-11}	-	-	N_2/-	-	2018
MoS_2/CC[25]	0.1M Na_2SO_4	25	8.1×10^{-11}	-	20-60	N_2/-	1.17	2018
Mo_2C/C[28]	0.5 M Li_2SO_4	25	-	11.3	10	N_2/-	7.8	2018
Fe[44]	FPEE+[C4mpyr][eFAP]	25	2.4×10^{-11}	-	-	N_2/-	32	2018

VN[48]	Nafion	80	3.3×10^{-10}	-	100	N_2/-	6	2018
Fe_2O_3 nanorods[29]	0.1M Na_2SO_4	25	-	15.9	20-50	N_2/-	0.94	2018
Mo_2C/C[28]	0.5M Li_2SO_4	25	-	11.3	10	N_2/-	7.8	2018
porous carbon[30]	0.05M H_2SO_4	25	-	23.8	-	N_2/-	1.4	2018
Au/C_3N_4/CP[32]	0.005M H_2SO_4	25	-	1305	-	N_2/-	11.1	2018
VN/Ti mesh[34]	0.1M HCl	25	8.4×10^{-11}	–	–	N_2/-	2.25	2018
B_4C/CP[35]	0.1M HCl	25		26.6	-	N_2/-	16.0	2018
Nb_2O_5/CP[37]	0.1M HCl	25	43.6	-	-	N_2/-	9.26	2018
nitrogen-doped nanoporous graphitic carbon (NCM)[36]	0.1M HCl	25	1.3×10^{-10}	-	-	N_2/-	5.2	2018
NCM-AuNPs[36]	0.1M HCl	25	5.9×10^{-10}	-	-	N_2/-	22	2018
Cobalt phosphide hollow nanocages (CoP HNC)[38]	1M KOH	25	-	10.8	–	N_2/-	7.4	2018
α-Fe_2O_3-CNT/CP[39]	0.1M KOH	25	-	1.5	30	N_2/-	8.3	2018

Pt/C[40]	0.1M KOH	25	2.0×10^{-11}	-	100	N_2/-	0.2	2018

Table 1-3 Performance and condition of ammonia formation at intermediate temperature. The number after the cathode refers to the reference.

Cathode	Electrolyte	T (°C)	r_{NH3} (mol s^{-1} cm^{-2})	r_{NH3} (μg h^{-1} mg^{-1})	Flow rate (sccm)	Atmo-Sphere (cathode/ anode)	Current effi-ciency (%)	Year
Porous Ni[90]	LiCl-KCl-CsCl	400	6.7×10^{-9}	–	–	N_2/H_2	60	2005
$La_{0.6}Sr_{0.4}Fe_{0.8}Cu_{0.2}O_3$ - $Ce_{0.8}Sm_{0.2}O_2$ (LSFCu-SDC)[91]	SDC-carbonate	450	5.4×10^{-9}	–	–	N_2/H_2	–	2011
$CoFe_2O_4$ /Ag[92]	carbonate-$LiAlO_2$	400	2.3×10^{-10}	–	–	N_2/H_2	–	2011
$La_{0.8}Cs_{0.2}Fe_{0.8}Ni_{0.2}O_3$ [93]	$Ce_{0.8}Gd_{0.2}O_2$-$(Li,Na,K)_2CO_3$	400	9.2×10^{-11}	–	50	Air-H_2O/ Air-H_2O	<0.1	2014
$La_{0.8}Cs_{0.2}Fe_{0.8}Ni_{0.2}O_3$ [93]	$Ce_{0.8}Gd_{0.2}O_2$-$(Li,Na,K)_2CO_3$	400	1.2×10^{-10}	–	50	N_2-H_2O/ N_2-H_2O	0.5	2014
$CoFe_2O_4$-$Ce_{0.8}Gd_{0.18}Ca_{0.02}O_2$ (CFO-CGDC)[94]	CGDC ternary carbonate	400	6.5×10^{-11}	–	50	N_2-H_2O/ N_2-H_2O	–	2014

$La_{0.6}Sr_{0.4}Fe_{0.8}Cu_{0.2}O_3$ - $Ce_{0.8}Gd_{0.18}Ca_{0.02}O_2$[95]	$Ce_{0.8}Gd_{0.2}O_2$-$(Li,Na,K)_2CO_3$	400	5.0×10^{-11}	–	50	N_2-H_2O/ N_2-H_2O	0.1	2014
$La_{0.6}Sr_{0.4}FeO_3$- $Ce_{0.8}Gd_{0.18}Ca_{0.02}O_2$[96]	$Ce_{0.8}Gd_{0.2}O_2$-$(Li,Na,K)_2CO_3$	400	7.0×10^{-11}	–	50	N_2-H_2O/ N_2-H_2O	0.1	2014
$Pr_{0.6}Ba_{0.4}Fe_{0.8}Cu_{0.2}O_3$ [97]	$Ce_{0.8}Gd_{0.2}O_2$-$(Li,Na,K)_2CO_3$	400	1.1×10^{-10}	–	50	N_2-H_2O/ N_2-H_2O	5	2014
$Sm_{0.6}Ba_{0.4}Fe_{0.8}Cu_{0.2}O_3$[98]	$Ce_{0.8}Gd_{0.2}O_2$-$(Li,Na,K)_2CO_3$	400	9.2×10^{-11}	–	50	Air-H_2O/Air-H_2O	0.7	2014
$Sm_{0.6}Ba_{0.4}Fe_{0.8}Cu_{0.2}O_3$[98]	$Ce_{0.8}Gd_{0.2}O_2$-$(Li,Na,K)_2CO_3$	400	1.5×10^{-10}	–	50	N_2-H_2O/ N_2-H_2O	1.2	2014
Co_3Mo_3N –Ag[99]	carbonate-$LiAlO_2$	450	3.3×10^{-10}	–	–	N_2/H_2	–	2014
Nano Fe_2O_3[100]	0.5 M NaOH/ 0.5 M KOH	200	2.4×10^{-9}	–	–	N_2-H_2O/ N_2-H_2O	35	2014
Fe_2O_3[56]	$Na_{0.5}K_{0.5}OH$	105	1.6×10^{-8}	–	–	N_2-H_2O/ N_2-H_2O	~2	2014
Fe_2O_3[56]	$Na_{0.5}K_{0.5}OH$	200	$\sim 10^{-10}$	–	–	N_2-H_2O/ N_2-H_2O	71	2014
Fe_3Mo_3N[101]	carbonate-$LiAlO_2$	425	1.9×10^{-10}	–		N_2/H_2		2015
$CoFe_2O_4$[52]	LiCl-KCl-CsCl	327	1.8×10^{-10}	–	200	N_2/H_2O		2016

Fe_2O_3[52]	LiCl-KCl-CsCl	327	3.0×10^{-10}	–	200	N_2/H_2O		2016
$Pt/TiO_2|C$[57]	$CsH_5(PO_4)_2/SiO_2$	220	2.0×10^{-10}	–	50	N_2/H_2O	2.1	2016
Fe_2O_3/activated carbon powders (AC)[54]	NaOH-KOH	250	8.3×10^{-9}	–	250	N_2/H_2O	13.7	2016
nano-Fe_3O_4[55]	NaOH-KOH	210	6.5×10^{-10}	–	80	N_2/H_2	9.3	2017
Ni[53]	NaOH/KOH+ Nano Fe_3O_4	200	4.4×10^{-9}	–	80	N_2/H_2	14.2	2017
Ru/C[61]	CsH_2PO_4/SiP_2O_7 composite	220	8.5×10^{-11}	–	50	N_2/H_2	<0.1	2017
Pt/C[61]	CsH_2PO_4/SiP_2O_7 composite	220	2.3×10^{-10}	–	50	N_2/H_2	<0.1	2017
Ru[61]	CsH_2PO_4/SiP_2O_7 composite	220	1.7×10^{-10}	–	50	N_2/H_2	0.1	2017
Ag-Pd[61]	CsH_2PO_4/SiP_2O_7 composite	220	8.5×10^{-10}	–	50	N_2/H_2	0.1	2017
Ru/C[61]	CsH_2PO_4/SiP_2O_7 composite	220	1.9×10^{-11}	–	50	N_2/H_2O	0.1	2017
Pt/C[61]	CsH_2PO_4/SiP_2O_7 composite	220	6.5×10^{-12}	–	50	N_2/H_2O	<0.1	2017
Ru[61]	CsH_2PO_4/SiP_2O_7 composite	220	1.3×10^{-11}	–	50	N_2/H_2O	<0.1	2017
Ag-Pd[61]	CsH_2PO_4/SiP_2O_7 composite	220	9.0×10^{-12}	–	50	N_2/H_2O	<0.1	2017

Pt-Ru/C[61]	CsH_2PO_4/SiP_2O_7 composite	220	1.3×10^{-11}	–	50	N_2/H_2O	<0.1	2017
$Ru/Cs^+/MgO$[59]	CsH_2PO_4/SiP_2O_7	250	7.7×10^{-10}	–	1	N_2/H_2O	3.5	2017
$Ru/Cs^+/MgO$ |Pd-Ag[60]	CsH_2PO_4/SiP_2O_7	250	9.0×10^{-10}	–	3	N_2/H_2O	2.6	2018
$Ru/Cs^+/MgO$*[158]	CsH_2PO_4/SiP_2O_7	250	1.2×10^{-8}	–	1	N_2/H_2O	12	2019

Table 1-4 Performance and condition of ammonia formation at high temperature. The number after the cathode refers to the reference.

Cathode	Electrolyte	T (°C)	r_{NH3} (mol s^{-1} cm^{-2})	r_{NH3} (μg h^{-1} mg^{-1})	Flow rate (sccm)	Atmo-Sphere (cathode/ anode)	Current effi-ciency (%)	Year
Pd[13]	$SrCe_{0.95}Yb_{0.05}O_3$	570	4.5×10^{-9}	-	5	N_2/H_2	78	1998
AgPd[64]	$La_{1.9}Ca_{0.1}Zr_2O_{6.95}$	460-560	1.7×10^{-9}	-	18000	N_2/H_2	68	2004
AgPd[67]	$La_{1.95}Ca_{0.05}Zr_2O_{6.95}$	460-560	2.0×10^{-9}	-	0.018	N_2/H_2	–	2005
AgPd[102]	$BaCe_{0.8}Gd_{0.2}O_3$	480	3.1×10^{-9}	-	18000	N_2/H_2	–	2005
AgPd[63]	$Ba_3Ca_{0.9}Nd_{0.2}{}_8Nb_{1.82}O_9$	620	2.2×10^{-9}	-	-	N_2/H_2	–	2005
Ad-Pd[103]	yttrium doped ceria YDC–$Ca_3(PO_4)_2$–K_3PO_4	650	7.0×10^{-9}	–	-	N_2/CH_4	-	2006
Ad-Pd[81]	$Ce_{0.8}La_{0.2}O_2$	650	7.2×10^{-9}	–	18000	N_2/H_2	-	2006
Ad-Pd[81]	$Ce_{0.8}Y_{0.2}O_2$	650	7.5×10^{-9}	–	18000	N_2/H_2	-	2006
Ad-Pd[81]	$Ce_{0.8}Gd_{0.2}O_2$	650	7.7×10^{-9}	–	18000	N_2/H_2	–	2006
Ad-Pd[81]	$Ce_{0.8}Sm_{0.2}O_2$	650	8.2×10^{-9}	–	18000	N_2/H_2	–	2006
Ad-Pd[79]	$BaCe_{0.8}Gd_{0.1}Sm_{0.1}O_3$	620	5.8×10^{-9}	–	18000	N_2/H_2	-	2007

AgPd[66]	$La_{0.9}Sr_{0.1}Ga_{0.8}Mg_{0.2}O_3$	550	2.4×10^{-9}	-	30	N_2/H_2	70	2007
Fe[62]	$SrZr_{0.9}Y_{0.1}O_3$	450	1.1×10^{-9}	2.2	50	25% N_2-75% H_2	200	2007
Fe[62]	$SrZr_{0.9}Y_{0.1}O_3$	450	1.1×10^{-10}	0.22	50	N_2-H_2-Ar/H_2	<1	2007
Ad-Pd[104]	$La_{0.9}Ba_{0.1}Ga_{0.8}Mg_{0.2}O_3$	520	1.9×10^{-9}	–	30	N_2/H_2	–	2008
Ad-Pd[80]	$BaCe_{0.85}Y_{0.15}O_3$	500	2.1×10^{-9}	–	–	N_2/H_2	-	2009
Ad-Pd[84]	$BaCe_{0.8}Gd_{0.2}O_3$	480	4.6×10^{-9}	–	30	N_2/H_2	70	2009
Ru/MgO[68]	$SrCe_{0.95}Yb_{0.05}O_3$	550	–	6×10^{-5}	50	N_2/H_2O	–	2009
$Ba_{0.5}Sr_{0.5}Co_{0.8}Fe_{0.2}O_3$[69]	$BaCe_{0.85}Y_{0.15}O_3$	530	4.1×10^{-9}	-	30	N_2/H_2	60	2010
Ad-Pd[82]	$BaCe_{0.9}Ca_{0.1}O_3$	480	2.7×10^{-9}	–	30	N_2/H_2	50	2010
Ad-Pd[83]	$BaCe_{0.85}Dy_{0.15}O_3$	530	3.5×10^{-9}	–	–	N_2/H_2	–	2010
Ad-Pd[65]	$Ba_{0.98}Ce_{0.8}Y_{0.2}O_3$+ 0.04ZnO	500	2.4×10^{-9}	–	30	N_2/H_2	–	2011
Pt[71]	$BaZr_{0.8}Y_{0.2}O_3$	-	$< 10^{-12}$	-	30	N_2/H_2O	≦1	2015
$La_{0.6}Sr_{0.4}Co_{0.2}Fe_{0.8}O_3$[71]	$BaZr_{0.8}Y_{0.2}O_3$	550	8.5×10^{-11}	-	30	N_2/H_2O	≦1	2015
Ag[71]	$BaZr_{0.8}Y_{0.2}O_3$	550	4.9×10^{-11}	-	30	N_2/H_2O	≦1	2015

Ni-$BaZr_{0.7}Ce_{0.2}Y_{0.1}O_3$[70]	$BaZr_{0.7}Ce_{0.2}Y_{0.1}O_3$	600	2.9×10^{-9}	1.18	150	N_2-H_2/ N_2-H_2	6.2	2015
Ni-$BaZr_{0.7}Ce_{0.2}Y_{0.1}O_3$[72]	$BaZr_{0.7}Ce_{0.2}Y_{0.1}O_3$	620	4×10^{-9} (mol s^{-1})	-	150	N_2-H_2/ N_2-H_2	-	2015
Ru-doped $La_{0.5}Sr_{0.5}Ti_{0.6}Ru_{0.4}O_3$[73]	$BaCe_{0.9}Y_{0.1}O_3$	500	5.0×10^{-12}	-	20	N_2/H_2	2.3	2015
AgPd[73]	$BaCe_{0.9}Y_{0.1}O_3$	500	3.0×10^{-11}	-	20	N_2/H_2	0.9	2015
Ni-$BaCe_{0.2}Zr_{0.7}Y_{0.1}O_3$[76]	$BaCe_{0.2}Zr_{0.7}Y_{0.1}O_3$	620	4.1×10^{-9}	-	150	N_2-H_2/ N_2-H_2	9.2	2016
Ru-doped $La_{0.3}Sr_{0.6}TiO_3$[77]	$BaCe_{0.9}Y_{0.1}O_3$	500	3.8×10^{-12}	-	20	N_2/H_2	–	2016
K-Al-Fe-$BaCe_{0.9}Y_{0.1}O_3$[74]	$BaCe_{0.9}Y_{0.1}O_3$	650	6.7×10^{-10}	4	20	15% H_2-85% N_2/Ar-H_2	0.3	2017
Ni-Ru-doped $BaCe_{0.9}Y_{0.1}O_3$[75]	$BaCe_{0.9}Y_{0.1}O_3$	500	1.1×10^{-11}	-	20	N_2/H_2	0.3	2017
Ni-BCY[78]	$BaCe_{0.9}Y_{0.1}O_3$	500	3.4×10^{-10}	-	60	N_2/H_2	0.63	2017
Ni-BCY[78]	$BaCe_{0.9}Y_{0.1}O_3$	500	2.8×10^{-10}	-	60	N_2/H_2O	0.15	2017

Ag-Co_3Mo_3N[85]	K-β"-Al_2O_3	500	-	15.3	75	N_2-H_2/ N_2-H_2	>300	2017

2. Methods

2.1. **Powder preparation**

In this study, $BaCe_{0.9}Y_{0.1}O_3$ (BCY), Fe_2O_3, and yttria–stabilized zirconia (YSZ) powders were prepared for cell preparation. Fine Fe_2O_3 powder (99.9% purity; Fujifilm Wako Pure Chemical, Co., Inc., Japan) and fine YSZ powder (10%Y_2O_3, Tosoh, Co., Inc., Japan) were obtained after the ball milling using ZrO_2 balls. BCY powder was synthesized by the coprecipitation method. The steps were described as following:

1. The precursors of $Ba(NO_3)_2$ (99.99% purity; Kanto Chemical Co., Inc., Japan), $Ce(NO_3)_3{\cdot}6H_2O$ (99.99% purity; Kanto Chemical Co., Inc., Japan), and $Y(NO_3)_3{\cdot}6H_2O$ (99.99% purity; Kanto Chemical Co., Inc., Japan), were dissolved stoichiometrically in 300 ml water.
2. The concentration of $(NH_4)_2(COO)_2$ (99.5% purity; Kanto Chemical Co. Inc., Japan), which was 1.5 times higher than the total cation concentration, was dissolved in 600 ml water.
3. The solution in step 1 was slowly added into $(NH_4)_2(COO)_2$ solution to form a white gel.
4. The white precipitate was obtained by filtering the gel with the suction filtration, and then dried at 80°C for one night. The dried precipitate was precalcined at 800°C and then calcined at 1200°C in air to obtain BCY powder.
5. Finally, fine BCY powder was obtained by the ball milling.

2.2. **Cell preparation**

2.2.1. Electrolyte preparation

BCY (YSZ) pellets were prepared by a uniaxial press and subsequent cold isostatic press. 1.5 g BCY (YSZ) powder was uniaxially pressed under 1 t cm^{-2}, and then isostatically pressed under 180 MPa. Next, the BCY (YSZ) pellets were calcined at 1600°C in air in a crucible with sacrificial powder of BCY (YSZ) to prevent intermixing and Ba atoms escaping.

2.2.2. Slurry preparation

The slurry was prepared by mixing the following chemicals:

1. α-terpineol (solvent) (98% purity; Fujifilm Wako Pure Chemical, Co., Inc., Japan): 3.7 g

2. Ethyl cellulose (binder) (48.0%–49.5% ethoxy content; Kanto Chemical, Co., Inc., Japan): 0.5 g
3. Nonion OP-83 RAT sorbitan sesquioleate (dispersant) (NOF, Co., Japan): 0.3 g
4. dibutyl phthalate (plasticizer) (99.5% purity; Kanto Chemical, Co., Inc., Japan): 0.3 g
5. poly(methyl methacrylate) resin (pore formation) (99.9% purity;: Tokyo Chemical Industry, Co., Ltd., Japan): 0.35 g

2.2.3. Fe–BCY cermet working electrode (cathode) preparation

Porous pure BCY electrode on BCY electrolyte was fabricated by the doctor-blade method. Then, iron nitride solution was poured onto the porous pure BCY by the impregnation method. Next, the samples were annealed to obtain Fe−BCY. The steps were described below:

1. BCY powder was mixed with the slurry (weight ratio 1:1) in section 2.2.2.
2. The mixed slurry was pasted onto the BCY electrolyte and calcined at 1300°C in air to obtain a porous pure BCY cathode.
3. $Fe(NO_3)_3{\cdot}9H_2O$ was stoichiometrically dissolved in water to prepare 0.5M iron nitrate solution.
4. The iron nitrate solution was poured onto the BCY porous cathode under vacuum, and then dried at 80°C for 5 mins.
5. The sample was annealed at 500°C in air.
6. Repeat steps 4-5 to obtain an appropriate amount of Fe.
7. The sample was annealed at 900°C in 3% H_2−97% Ar to obtain a 10 wt.%Fe–BCY (10Fe–BCY) cathode.

2.2.4. W–Fe–BCY cermet working electrode (cathode) preparation

W–Fe–BCY electrode on BCY electrolyte was fabricated by the same method as that for Fe−BCY electrode. The steps were described below:

1. BCY powder was mixed with the slurry in section 2.2.2.
2. The mixed slurry was pasted onto the BCY electrolyte and calcined at 1300°C in air to obtain a porous pure BCY cathode.
3. Ammonium metatungstate (99.99% purity; Sigma-Aldrich, USA) and $Fe(NO_3)_3{\cdot}9H_2O$ (99.99% purity; Wako Chemical Co., Inc., Japan) were stoichiometrically dissolved in water to prepare 0.5M iron nitrate solution.

4. The mixture solution was poured onto the BCY porous cathode and dried at 80°C for 5 mins.
5. The sample was annealed at 700°C in air.
6. Repeat steps 4-5 to obtain 10 wt.% Fe and 0.5 wt.% W (or 1 wt.%W)
7. The sample was annealed at 900°C in pure hydrogen to obtain 0.5 wt.%W–10 wt.%Fe–BCY (0.5W–10Fe–BCY) or 1 wt.%W–10 wt.%Fe–BCY (1W–10Fe–BCY) cathode.

2.2.5. Porous pure Fe working electrode (cathode) preparation

Porous pure Fe electrode on BCY electrolyte was fabricated by the doctor-blade method. The steps were described below:

1. Fe_2O_3 powder was mixed with the slurry in section 2.2.2.
2. The mixed slurry was pasted onto the BCY electrolyte and calcined at 900°C in air to obtain a porous pure BCY cathode.
3. The sample was annealed at 900°C in 3% H_2−97% Ar to obtain porous pure Fe cathode on BCY electrolyte.

2.2.6. Pt counter electrode (anode) and reference electrode preparation

Pt counter electrode and reference electrode on another side of BCY (YSZ) electrolyte were prepared by the doctor-blade method. Pt slurry was pasted onto the BCY (YSZ) electrolyte and then calcined at 900°C in air to obtain Pt counter electrode and reference electrode. The cell is shown in Fig. 2-1.

2.3. Characterization

2.3.1. X–Ray diffraction

X–Ray diffraction (XRD) is a tool for detecting the crystal structure of material. When X-ray whose wavelength is around 0.01-100 Å incidents into a crystalline material, the interaction of the incident with the sample produces a constructive interference if the condition satisfied the Bragg's Law ($n \times \lambda = 2 \times d \times \sin\theta$), where n, λ, d, θ, is a positive integer, wavelength of the incident wave, distance between discrete parallel plane, and glancing angle.

In this study, XRD was conducted to identify the phases of cathode and electrolyte. XRD (SmartLab, Rigaku, Japan) was operated at 40 kV and 30 mA with Cu Kα source. Scans were from 20-80° 2θ with a step size of 0.02°.

2.3.2. Scanning electron microscopy

Scanning electron microscopy (SEM) is used to scan the morphology of sample with a focused electron beam. When an electron beam incidents into the sample, exciting electrons including secondary electrons and backscattered electrons (BSE) are emitted by atoms. Secondary electrons are used to analyze the morphology of sample. BSE is used to detect the contrast between areas to confirm different chemical composition.

In this study, SEM was conducted to observe the cross-sectional images of interface between cathode and electrolyte. SEM images were obtained using JEOL JSM-5600, Japan, JEOL IT100, Japan, and S4700 unit Hitachi, Japan.

2.3.3. Transmission electron microscopy

Transmission electron microscopy (TEM) images were obtained using JEOL JEM-1200EX, Japan and JEOL JEM-2010F, Japan.

2.4. Equipment for electrochemical ammonia synthesis

The device for electrochemical ammonia formation is shown in Fig. 2-2. A single cell is set between two quartz tubes in a furnace. Pyrex glass rings are used to seal the quartz tubes at 900°C. After sealing, Fe and Fe−W are reduced in 3% H_2/Ar and pure H_2 atmosphere, respectively. Then, the temperature is lowered to the operating temperature (500−700°C) for ammonia electrosynthesis. The produced ammonia is either flowed into a capture solution of 0.01 mM H_2SO_4 for HPLC measurement or an optical cell for FTIR measurement.

2.4.1. Electrochemical impedance analysis

AC impedance spectroscopic measurement from 1 to 10^6 Hz is performed using Autolab PGSTAT128N (Metrohm Autolab B.V., Netherlands). Electrode potential is defined by Eq. 2-1 in the electrochemical measurements using the three-electrode method.

$$\text{Electrode potential} = V_{\text{app}} - (IR_{\text{ohm}} + \frac{RT}{nF}\ln(p_{H2,\,\text{anode}}/p_{\text{H2},\,\text{1bar}}) \quad \text{2-1}$$

(a) (b)

where V_{app}, I, R_{ohm}, R, T, n, F, and p_{H2} are the applied voltage, current, ohmic resistance, gas constant, temperature, electron transfer number, Faraday constant, and H_2 partial pressure in the anode, respectively. The term (a) corresponds to *IR* loss correction. The term (b) corresponds to a correction of the potential difference between H_2 partial pressure in the reference electrode and 1 bar H_2 pressure, i.e., the standard pressure.

2.4.2. High performance liquid chromatography

High performance liquid chromatography (HPLC) (EXTREMA, Jasco, Japan) is used to identify the component in a mixture. The sampler, which is composed of sample mixture and pressurized liquid, mobile phase, is carried into a column which is filled with a solid adsorbent material. Each component in the sample can be separated by different interactions between each component with the solid adsorbent material, which results in different flow rates.

In this study, IC Y-521 column with the mobile phase of 4 mM HNO_3 is used to analyze the concentration of ammonia in the capture solution of 0.01 mM H_2SO_4 using HPLC, which is used to capture ammonia in the gas flow from the cathode.

The calibration curve of ammonia concentration for HPLC is shown in Fig. 2-3. The ammonia solution is prepared by 1000 ppm standard ammonia solution (Wako Co., Japan) and 0.01mM sulfide acid solution.

2.4.3. Fourier-transform infrared spectroscopy

Fourier-transform infrared spectroscopy (FTIR) (FT/IR 670 Plus, JASCO, Japan) is used to obtain an infrared spectrum of adsorption/ transmission of sample. The infrared beam which passes through a Michelson interferometer is recombined to produce interference light. Then, the computer processes the data of the intensity of interference light to obtain the desired spectrum by the Fourier transform.

In this study, FTIR with a long optical path cell (8 m) (LPC-8M-S, JASCO, Japan) is used to investigate the concentration of $NH_{3-x}D_x$ (x = 0, 1, 2, 3) in the gas flow from the cathode. The FTIR spectral resolution was 4 cm^{-1}. The gas tubing and long optical path cell were kept at 80°C

and 70°C, respectively. To examine the adsorption of ammonia on the tube, the area of NH_3 spectra was investigated at different gas tubing temperatures, which was shown in Appendix A.

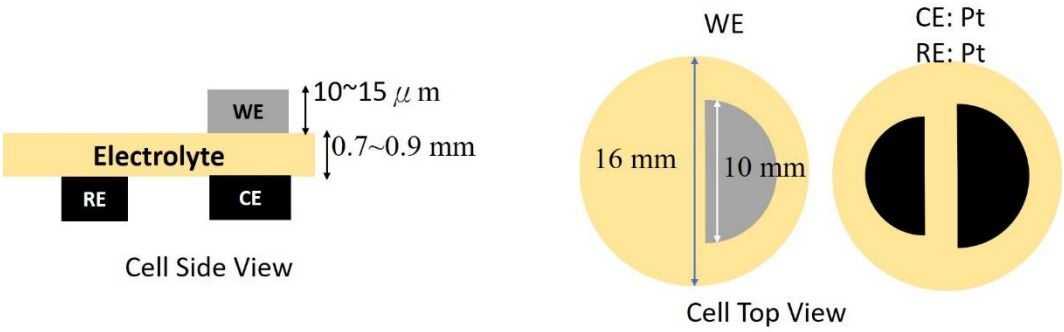

Fig. 2-1 A schematic image of cell.

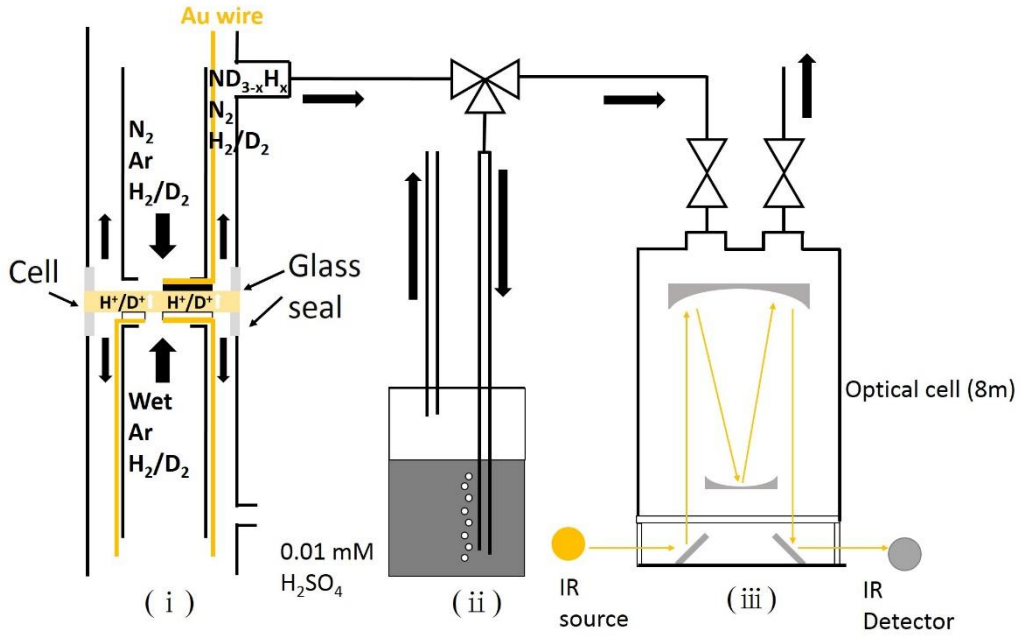

Fig. 2-2 A schematic of the device for electrochemical reaction of ammonia. (i) is the device for electrochemical reaction of ammonia synthesis. (ii) is a schematic of gas flow into capture solution. (iii) is a schematic of FTIR with an optical cell.

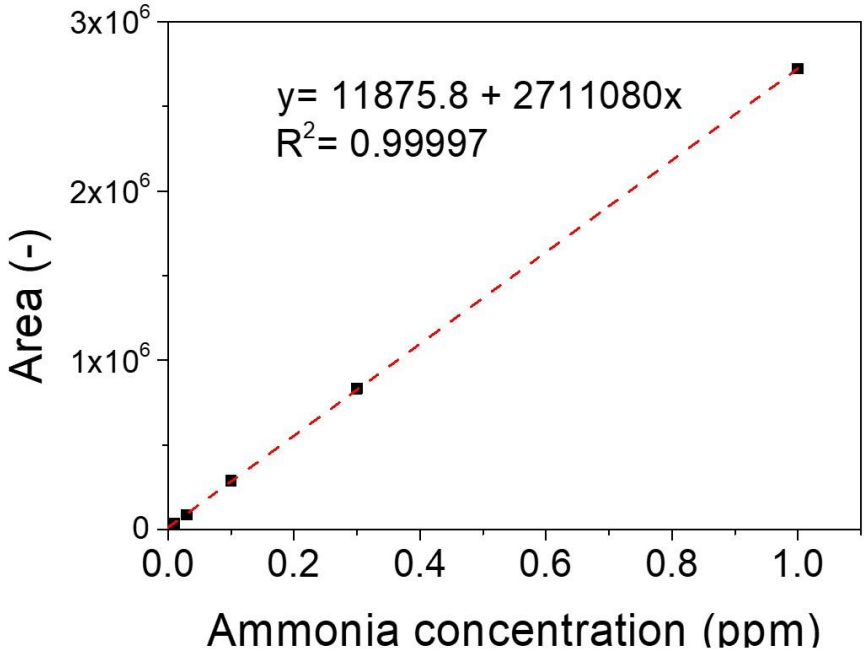

Fig. 2-3 Calibration curve of ammonia concentration by HPLC.

3. Effect of cathode structures on electrochemical ammonia synthesis

3.1. Introduction

In this chapter, the influence of the cathode structures on the performances of electrochemical ammonia formation is investigated. (W–)Fe–BCY cermet, which has relatively long TPB length, and porous pure Fe, which has relatively short TPB length (the relevant reactions are dominated by a two-phase boundary, i.e., the Fe surface), are used, as shown in Fig. 3-1−Fig. 3-3. Although Fe–BCY and W–Fe–BCY have a similar cathode structure (long TPB length), W addition can suppress the hydrogen evolution reaction and reduce the current density because of the higher adsorption energy of W–H formation than that of Fe–H.[105]

Ammonia formation rate r_{NH3}, the fraction of obtained NH_3 concentration to the NH_3 concentration at equilibrium X_{equ}, and current efficiency Λ, are defined by the following equations:

$$r_{\mathrm{NH_3}} = \frac{[\mathrm{NH_4^+}]\,V}{tA} \quad (3\text{-}1)$$

$$\Lambda_{CE} = \frac{r_{\mathrm{NH3}} nF}{i} \quad (3\text{-}2)$$

$$X_{\mathrm{equ}} = \frac{\frac{r_{\mathrm{NH3}} ARTf}{}}{K p_{\mathrm{H2}}{}^{\frac{3}{2}} p_{\mathrm{N2}}} \quad (3\text{-}3)$$

where $[\mathrm{NH_4^+}]$, V, t, A, i, K, p_{H2}, p_{N2}, and f are the NH_4 ion concentrations measured by HPLC, the volume of solution trapping NH_3, the capture time, the electrode area, current density, the equilibrium constant for Eq. 1-5, hydrogen partial pressure, nitrogen partial pressure, and flow rate, respectively.

3.2. Crystal structure of cathode by XRD

XRD was used to investigate the structures of the as-prepared samples of (W–)Fe–BCY and porous pure Fe cathodes on BCY electrolytes, as shown in Fig. 3-4. The single phase of Fe (cubic, $Im\bar{3}m$, PDF#00-006-0696) and that of BCY originating from the BCY electrolytes in W–Fe–BCY, Fe–BCY, and porous pure Fe samples were observed. Fe peaks for porous pure were stronger than those for W–Fe–BCY and Fe–BCY due to the high amount of Fe. However, relevant peaks of W

or W compounds were not detected because of the low amount of W in 0.5W−10Fe−BCY 1W−10Fe−BCY cathodes.

3.3. Cathode morphology

Fig. 3-5 shows cross-sectional scanning electron microscopy (SEM) images of the three cathode catalysts. The thicknesses of the BCY and Fe porous cathodes were approximately 10–15 μm. The size of BCY particles was about 300 nm in pure BCY, 10Fe–BCY, and 0.5W–10Fe–BCY electrodes. Although it is difficult to distinguish the position of Fe particles in the 10Fe–BCY cathode, the deposition of Fe particles on BCY particles can be observed by TEM images. In 0.5W–10Fe–BCY cathode, Fe particles tend to aggregate on the BCY surface. In the porous pure Fe cathode, the size of Fe particles was around 200–400 nm. Fig. 3-5m-o correspond to the SEM cross-sectional images of the cathodes after the electrochemical measurements, which show the particle aggregation of around 50, 130, and 150 nm in 10Fe–BCY, 0.5W–10Fe–BCY, and porous pure Fe cathodes, respectively.

For further observation of Fe and W positions in the cathode structures of 0.5W–10Fe–BCY, TEM was used to examine the micro-structures, as shown in Fig. 3-6. The TEM image of the pure porous BCY cathode shows that BCY particle size was around 300 nm, which agrees with the SEM result. After Fe or W–Fe infiltrated into BCY, small particles located on the BCY surface were observed in 10Fe–BCY and 0.5W–10Fe–BCY cathodes. Therefore, the small particles on the BCY surface should be Fe particles in 10Fe–BCY. The energy-dispersive X-ray spectroscopy (EDX) mapping of 0.5W–10Fe–BCY shows that Fe signal around the BCY surface and Ce signal locating on the BCY particle (Fig. 3-7). Judging from the TEM-EDX images, the small particles located on the BCY surface are Fe particles. However, the exact W position cannot be confirmed because the amount of W is too low to detect and the EDX peaks of W (M_α and M_β edges) and Y (L_α edge) are overlapping.

3.4. Comparison of electrochemical ammonia synthesis using (W-)Fe-BCY and porous pure Fe cathodes

3.4.1. Performance of electrochemical ammonia synthesis using (W–)Fe–BCY cathode

Experimental condition

Cathodes: 10Fe–BCY, 0.5W–10Fe–BCY and 1W–10Fe–BCY cathodes (15 μm)

Gas in the cathode: 10% H_2−90% N_2 with 20 sccm

Gas in the anode: wet 20% H_2–80% Ar with 30 sccm

Temperature: 550-700°C

Fig. 3-8 shows the performances using 10Fe–BCY, 0.5W–10Fe–BCY, and 1W–10Fe–BCY cathodes in 10% H_2–90% N_2, which have a similar structure with long TPB length (Fig. 3-1−Fig. 3-2). The three cathodes exhibited that the ammonia formation rate increased with decreasing the operating temperature between 600 and 700°C, which was probably caused by the active reverse reaction of NH_3 to N_2 and H_2 and the low value of X_{equ} at high temperature. Then, the ammonia formation rate decreased with decreasing the operating temperature between 500 and 600°C due to the low activity to ammonia formation. 10Fe–BCY cermet cathode exhibited the highest ammonia formation rate of 4.2×10^{-10} mol s^{-1} cm^{-2} (101 μg h^{-1} mg^{-1} Fe) at 600°C and electrode potential of –0.7 V. With a low amount of W addition to 10Fe–BCY, 0.5W–10Fe–BCY cathode exhibited a higher ammonia formation rate of 5.7×10^{-10} mol s^{-1} cm^{-2} at –1.2 V (137 μg h^{-1} mg^{-1} Fe) at a low operating temperature (550°C). However, 1W–10Fe–BCY showed a worse performance below 600°C because of too much W amount.

Fig. 3-9 shows the current densities using 10Fe–BCY, 0.5W–10Fe–BCY, and 1W–10Fe–BCY cathodes in 10% H_2–90% N_2. A corresponding current density, i.e., proton flux from the counter electrode (anode) to the working electrode (cathode), for 0.5W−10Fe−BCY and 1W−10Fe−BCY cathodes were reduced by approximately 40% and 80% compared with that of 10Fe−BCY cathode, respectively. In a comparison with the performance for 10Fe–BCY and 0.5W–10Fe–BCY, although the highest applied voltage was −1.5 V (corresponding electrode potentials were around –0.6 and –1.2 V for 10Fe–BCY and 0.5W–10Fe–BCY, respectively) at 600°C, the ammonia formation rates were mostly the same, whereas 0.5W−10Fe−BCY cathode had a lower current density than that of 10Fe−BCY. The result suggests that the influence of electrode potential on ammonia formation is more significant than that of current density.

Fig. 3-10 exhibits the current efficiencies for 10Fe–BCY, 0.5W–10Fe–BCY, and 1W–10Fe–BCY cathodes in 10%H_2–90%N_2. The electrochemical ammonia formation involved two charge-transfer reactions: 1) the electrochemical synthesis of ammonia and 2) the hydrogen evolution

reaction (Eq. 1-10). The low current efficiencies for ammonia formation below 2% represent that the electrochemical reaction is dominated by the hydrogen evolution reaction rather than the electrochemical ammonia formation. Therefore, the low current densities for 0.5W–10Fe–BCY and 1W–10Fe–BCY cathodes are caused by the suppression of the dominating hydrogen evolution reaction.

Fig. 3-11 shows the impedance analysis for 10Fe–BCY, 0.5W–10Fe–BCY, and 1W–10Fe–BCY at 600°C. The ohmic resistance, which is an intersection with X–axis, increased with W addition into 10Fe–BCY. In addition, the R_{LF}, which represents the resistance of charge-transfer reaction, also increased with W addition into 10Fe–BCY. This result also agrees with the low current densities for 0.5W–10Fe–BCY and 1W–10Fe–BCY cathodes because the dominating hydrogen evolution reaction is suppressed.

3.4.2. Performance of electrochemical ammonia synthesis using porous pure Fe cathode.

Experimental condition

Gas in the cathode: 10% H_2–90% N_2 with 20 sccm

Gas in the anode: wet 20% H_2–80% Ar with 30 sccm

Temperature: 550−600°C

Cathode: porous pure Fe (15 μm)

Compared to Fe−W cermet electrode, porous pure Fe cathode has a relatively low TPB length and high amount of Fe. Before the electrochemical ammonia formation, the properties of porous pure Fe including NH_3 decomposition behavior, the blank test, reversible test, and Fe cathode stability were examined, as shown in Appendix B−G. Fig. 3-12 shows the performance of ammonia formation rate and current density in 10% H_2–90% N_2 for porous pure Fe cathode. The highest ammonia formation rate was 1.3×10^{-9} mol s^{-1} cm^{-2} (44.33 μg h^{-1} mg^{-1} Fe) with a corresponding current density of about 27 mA cm^{-2} at 550°C. The ammonia formation rate for porous pure Fe was higher than that for 0.5W−10Fe−BCY, but the current density for porous pure Fe is similar to that for 0.5W−10Fe−BCY.

Due to the high ammonia formation rate, the current efficiency and X_{Equ} using porous pure Fe cathode achieved 1.6% and 47%, respectively, which were higher than those using

0.5W−10Fe−BCY, as shown in Fig. 3-13. Notably, a high ammonia formation rate using porous pure Fe cathode, which has short TPB length, is higher than that using (W−)10Fe−BCY cathodes, which has long TPB length. Here, two possible reasons are considered: 1) the large amount of Fe in porous pure Fe cathode makes the high ammonia formation rate; 2) ammonia is not formed via the charge-transfer reaction at the TPB but the surface reaction on the Fe surface. Therefore, in the next section, the effect of the amount of Fe on ammonia formation rate will be discussed.

3.4.3. Effect of Fe amount on electrochemical ammonia synthesis

Experimental condition

Gas in the cathode: 10% H_2–90% N_2 with 20 sccm

Gas in the anode: wet 20% H_2–80% Ar with 30 sccm

Temperature: 550-700°C

Cathode: 10Fe−BCY and 20Fe−BCY

As for the cathodes with long TPB length, Fig. 3-14 shows the performance of ammonia formation using 20Fe–BCY cathode between 550–700°C. The ammonia formation rates at rest potential using 20Fe–BCY were higher than 10Fe–BCY because of the high amount of Fe. However, the ammonia formation rates for 10Fe–BCY were closed to that for 20Fe–BCY cathodes with cathodic polarization. The highest ammonia formation rates were 5×10^{-10} at 650°C and 4.2×10^{-10} mol s^{-1} cm^{-2} at 600°C for 20Fe–BCY and 10Fe–BCY, respectively. Fig. 3-14b shows the current densities for 10Fe–BCY and 20Fe–BCY cathodes between 550–700°C. Except of 700°C, the current densities for 10Fe–BCY were similar to those for 20Fe–BCY between 550–650°C. This result indicates that increasing the amount of Fe in Fe–BCY cermet can improve the ammonia formation rate at rest potential but had no obvious effect on ammonia formation rate with cathodic polarization.

Experimental condition

Gas in the cathode: 10% H_2–90% N_2 with 40 sccm

Gas in the anode: wet 20% H_2–80% Ar with 30 sccm

Temperature: 550°C

Cathode: porous pure Fe (15 and 30 μm)

On the other hand, as for the cathode with short TPB length, the performances were investigated using porous pure Fe cathodes with 15 μm and 30 μm electrode thicknesses. The ammonia formation rate using 30 μm cathode was higher than that using 15 μm cathode at rest potential due to the large amount of Fe, as shown in Fig. 3-15. However, the ammonia formation rates increased to 2×10^{-9} mol s^{-1} cm^{-2} with cathodic polarization at 550°C for both the cathodes. Also, a high current density was observed using 30 μm cathode. This result indicated that increasing electrode thickness could not effectively improve ammonia formation rate with cathodic polarization. Based on the result in this section, the effect of increasing the amount of Fe in both 10Fe–BCY and porous pure Fe cathodes cannot improve the ammonia formation rate with cathodic polarization.

3.4.4. A comparison between Fe–BCY cermet and porous pure Fe cathodes

In section 3.4.2, the highest ammonia formation rate in (W)–Fe–BCY cermet catalyst, which had relatively long TPB length, was 5.7×10^{-10} mol s^{-1} cm^{-2} at 550°C using 0.5W–Fe–BCY cathode. On the other hand, the highest ammonia formation rate was 1.3×10^{-9} mol s^{-1} cm^{-2} for porous pure Fe cathode with 15 μm electrode thickness, which had short TPB length. It was observed that the performance of ammonia formation for porous pure Fe catalyst was a better catalyst than W–Fe–BCY cermet. Also, the effect of the amount of Fe was investigated in section 3.4.3. An increase in the amount of Fe cannot improve the ammonia formation rate for both 10Fe–BCY and porous pure Fe cathodes. Therefore, the high ammonia formation rate in porous pure Fe is probably caused by that the ammonia is formed via the surface reaction rather than the charge-transfer reaction at the TPB.

3.5. Conclusion

1. The performance of ammonia formation rate using porous pure Fe cathode, which has short TPB length, is better than that using 0.5W–Fe–BCY cathode, which has long TPB length.
2. W addition into Fe−BCY cermet cathode can improve ammonia formation rate and decrease current density, whereas excessive W addition into Fe−BCY will decrease ammonia formation rate.

3. The influence of electrode potential on the ammonia formation rate is more significant than that of current density.
4. For Fe−BCY cermet cathode, enhancement of the Fe amount cannot improve ammonia formation rate in the electrochemical reaction. Also, for porous pure Fe cathode, an increase in electrode thickness cannot improve the ammonia formation rate in the electrochemical reaction.
5. Ammonia is probably formed via the surface reaction rather than the charge-transfer reaction at the TPB in the electrochemical reaction.

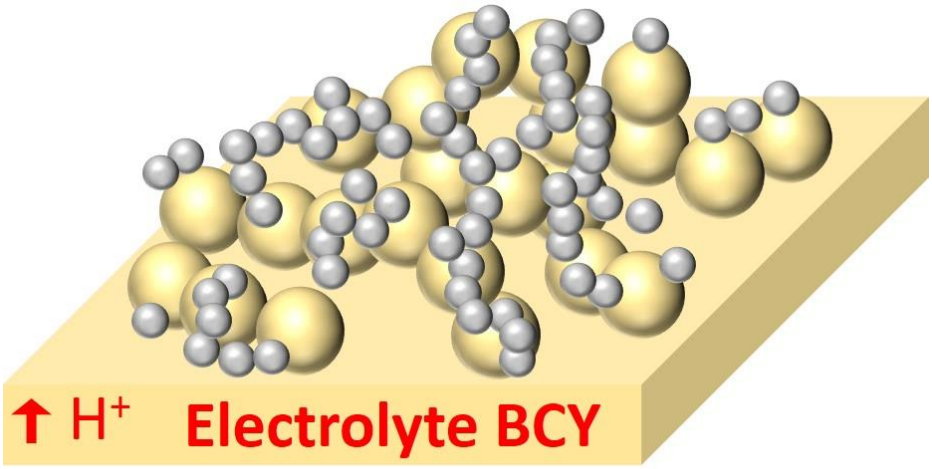

Fig. 3-1 A schematic image of Fe−BCY structure.

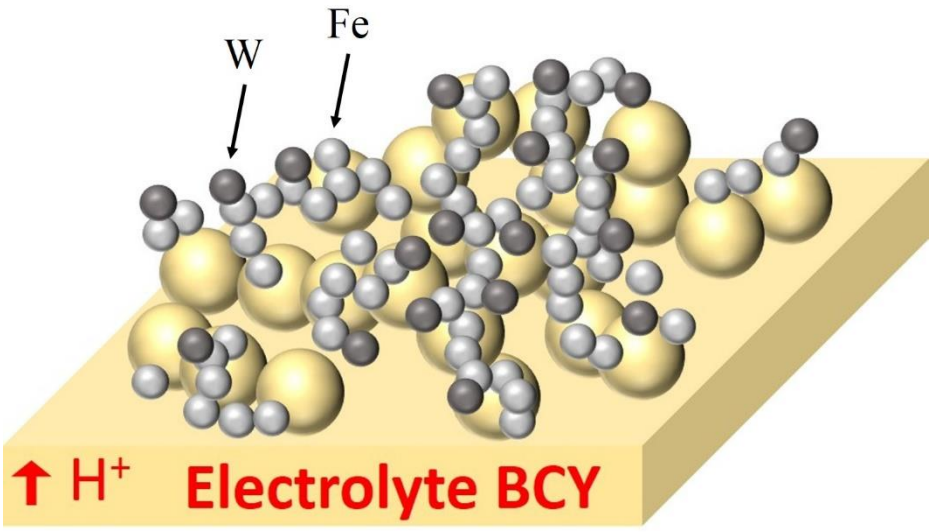

Fig. 3-2 A schematic image of W−Fe−BCY structure.

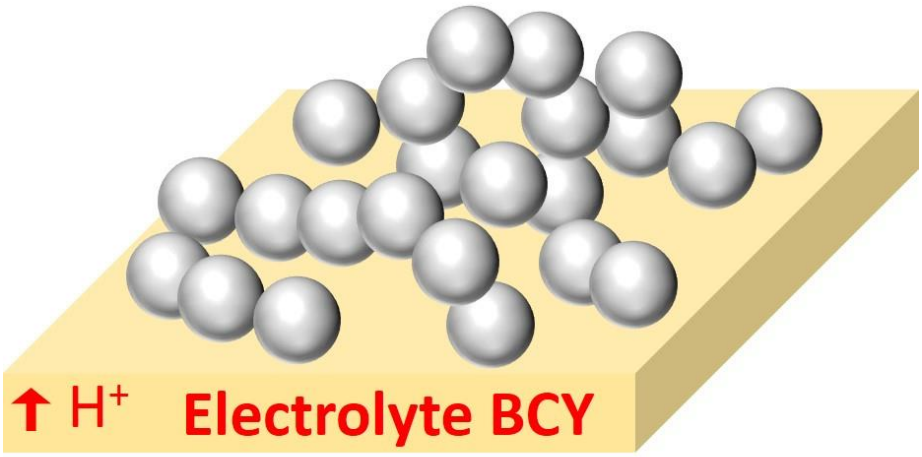

Fig. 3-3 A schematic image of porous pure Fe structure.

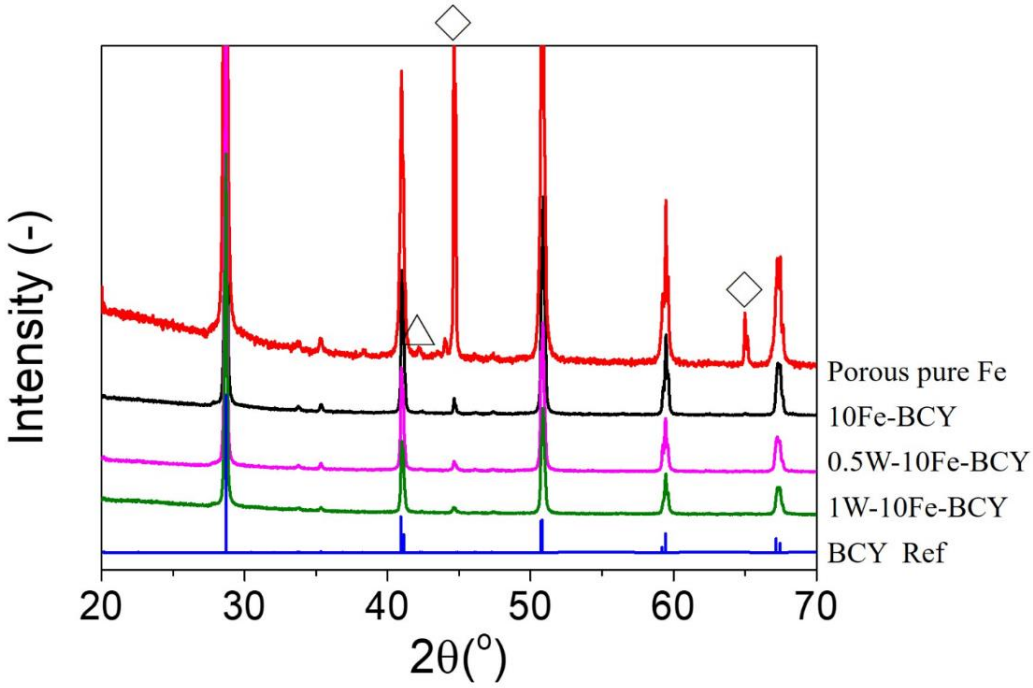

Fig. 3-4 XRD spectra of porous pure Fe, 10Fe–BCY, 0.5W–10Fe–BCY, and 1W–10Fe–BCY cathodes on BCY electrolytes.

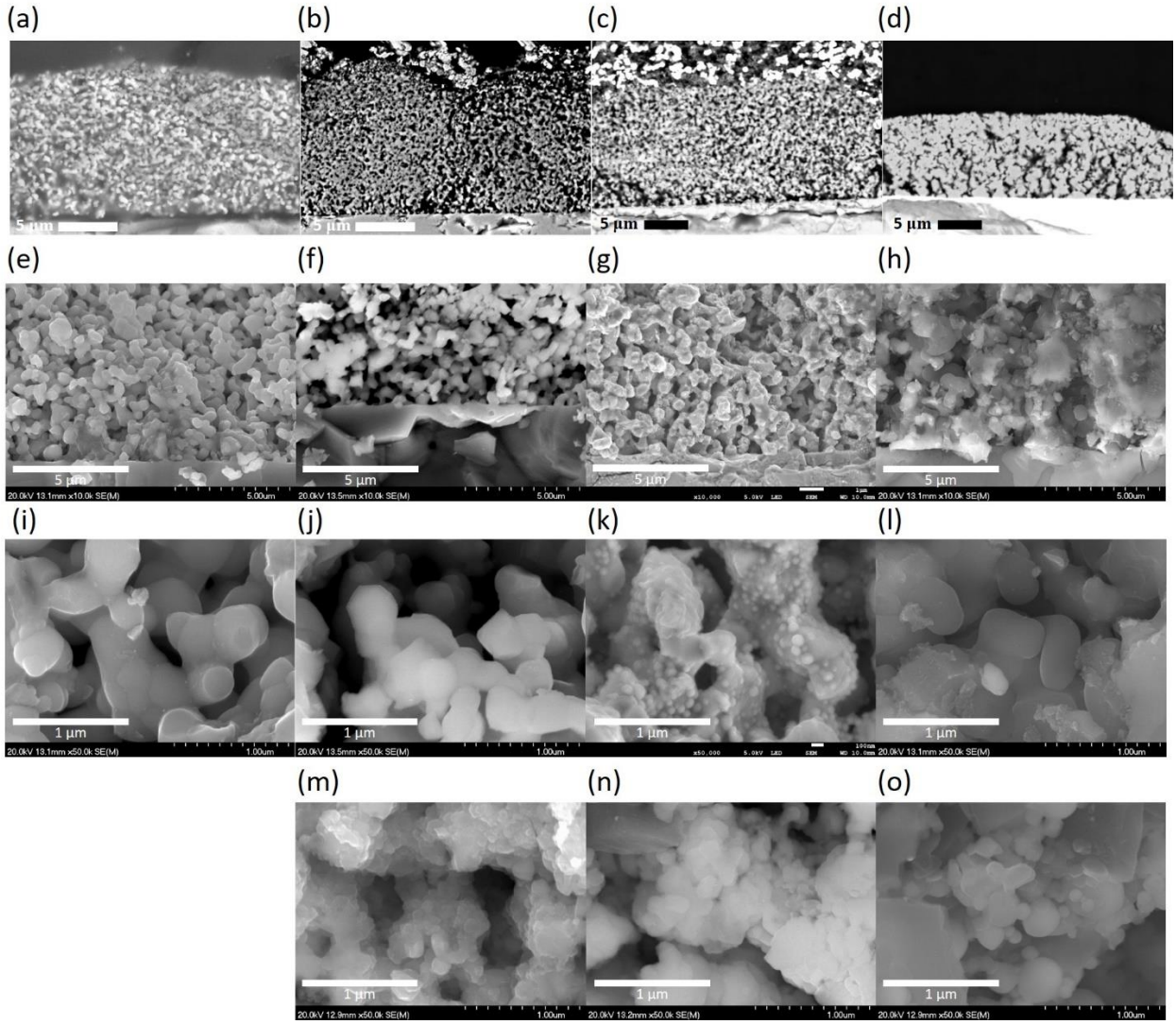

Fig. 3-5 Cross-sectional images of (a), (e), (i) porous pure BCY, (b), (f), (j) as-prepared 10Fe–BCY, (c), (g), (k) as-prepared 0.5W–10Fe–BCY, and (d), (h), (l) as-prepared porous pure Fe cathodes. (m) 10Fe–BCY after electrochemical measurement, (n) 0.5W–10Fe–BCY after electrochemical measurement, and (o) porous pure Fe after electrochemical measurement.

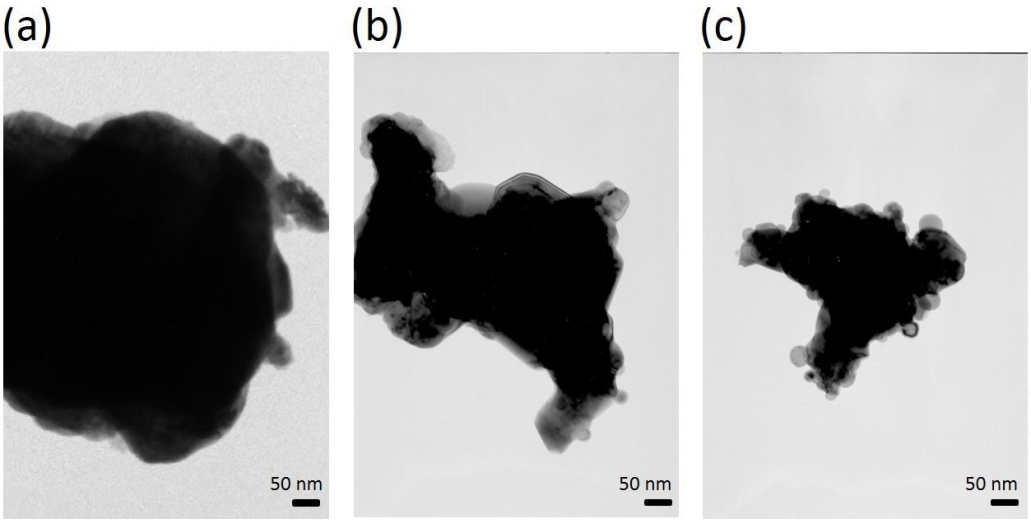

Fig. 3-6 TEM images of (a) pure BCY, (b) 10Fe–BCY, and (c) 0.5W–10Fe–BCY.

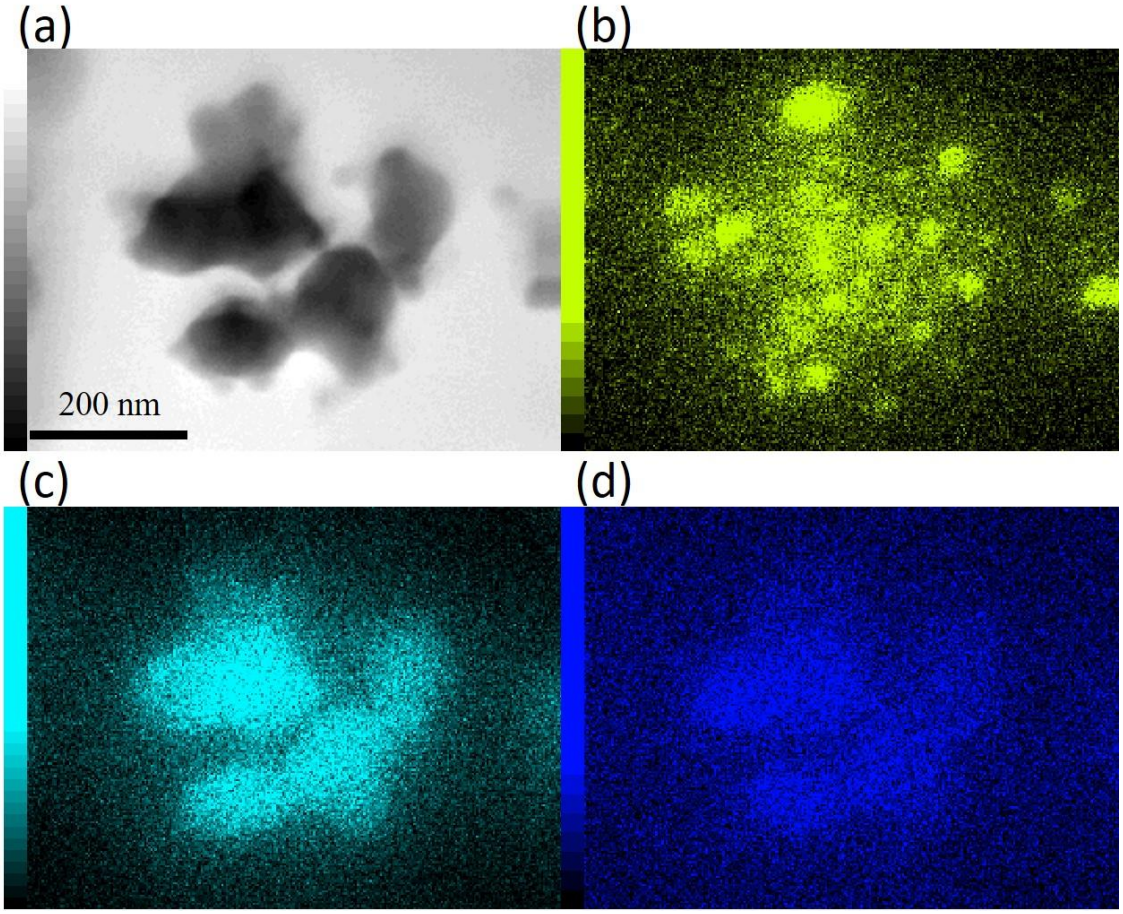

Fig. 3-7 (a) TEM image of 0.5W–10Fe–BCY, and TEM-EDX images of (b) Fe, (c) Ce, and (d) W elements.

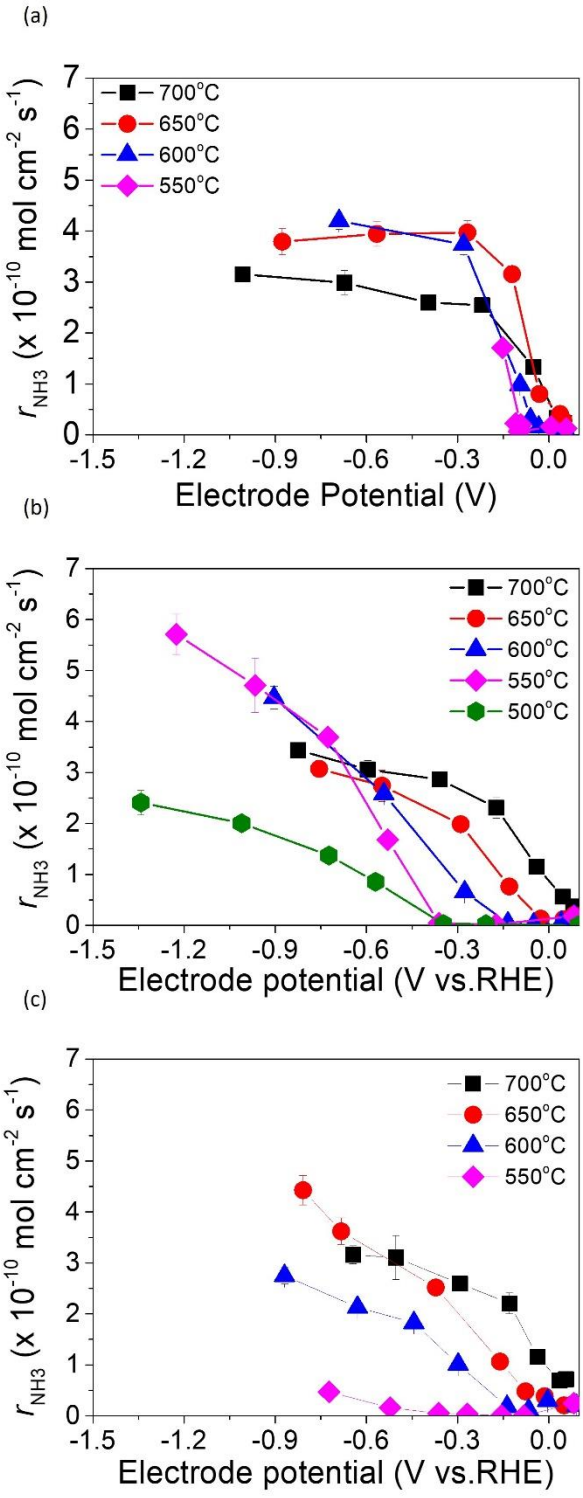

Fig. 3-8 Ammonia formation rate at different temperatures for (a) 10Fe−BCY, (b) 0.5W−10Fe−BCY, and (c) 1W−10Fe−BCY.

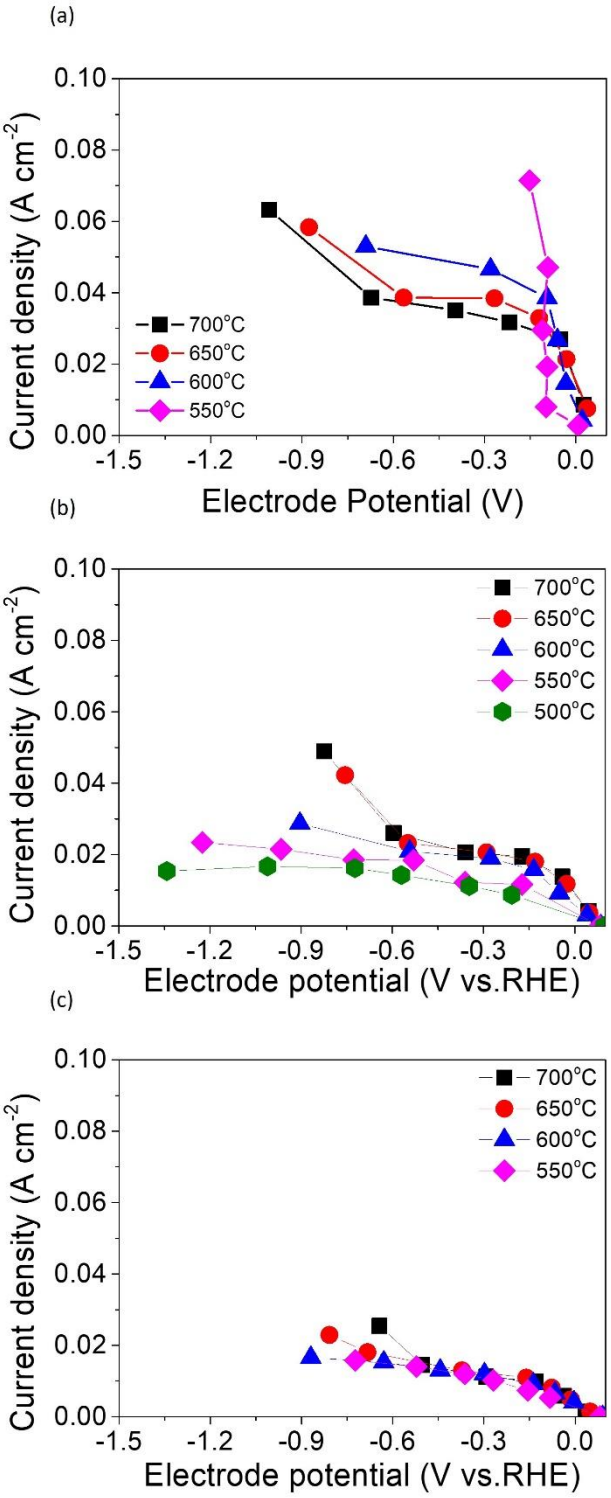

Fig. 3-9 Current densities at different temperatures for (a) 10Fe−BCY, (b) 0.5W−10Fe−BCY, and (c) 1W−10Fe−BCY.

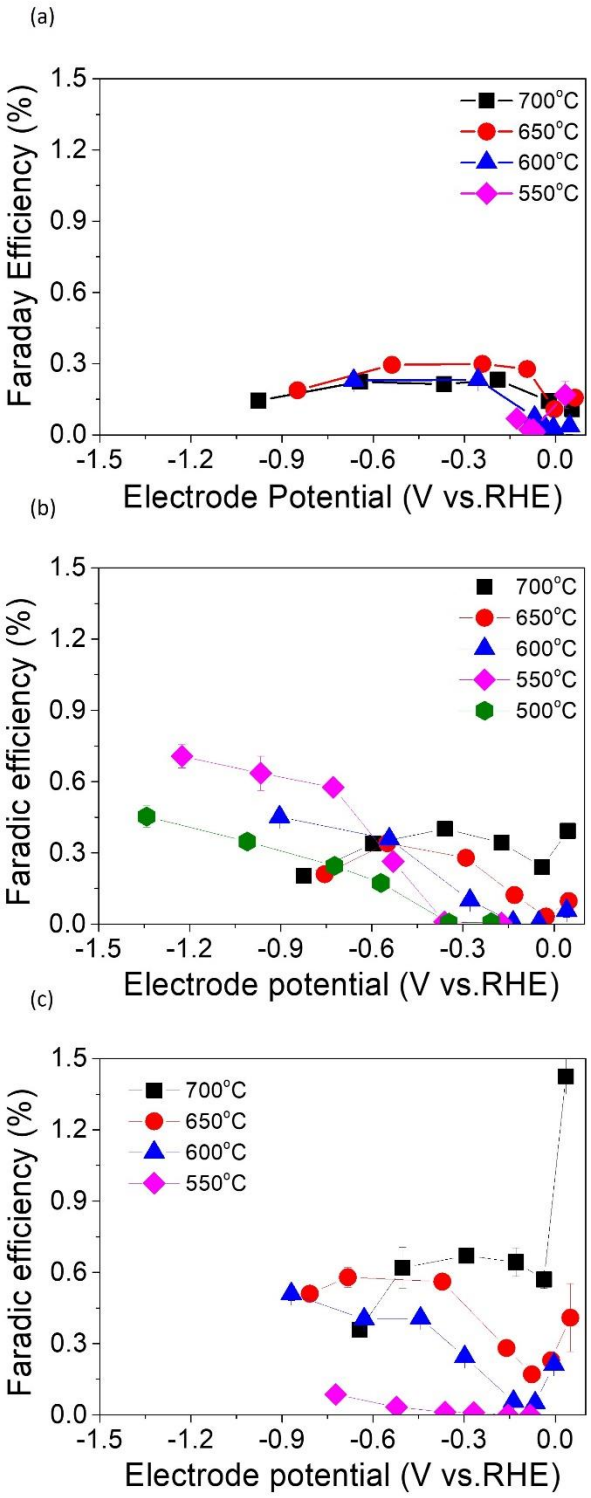

Fig. 3-10 Current efficiencies at different temperatures for (a) 10Fe−BCY, (b) 0.5W−10Fe−BCY, and (c) 1W−10Fe−BCY.

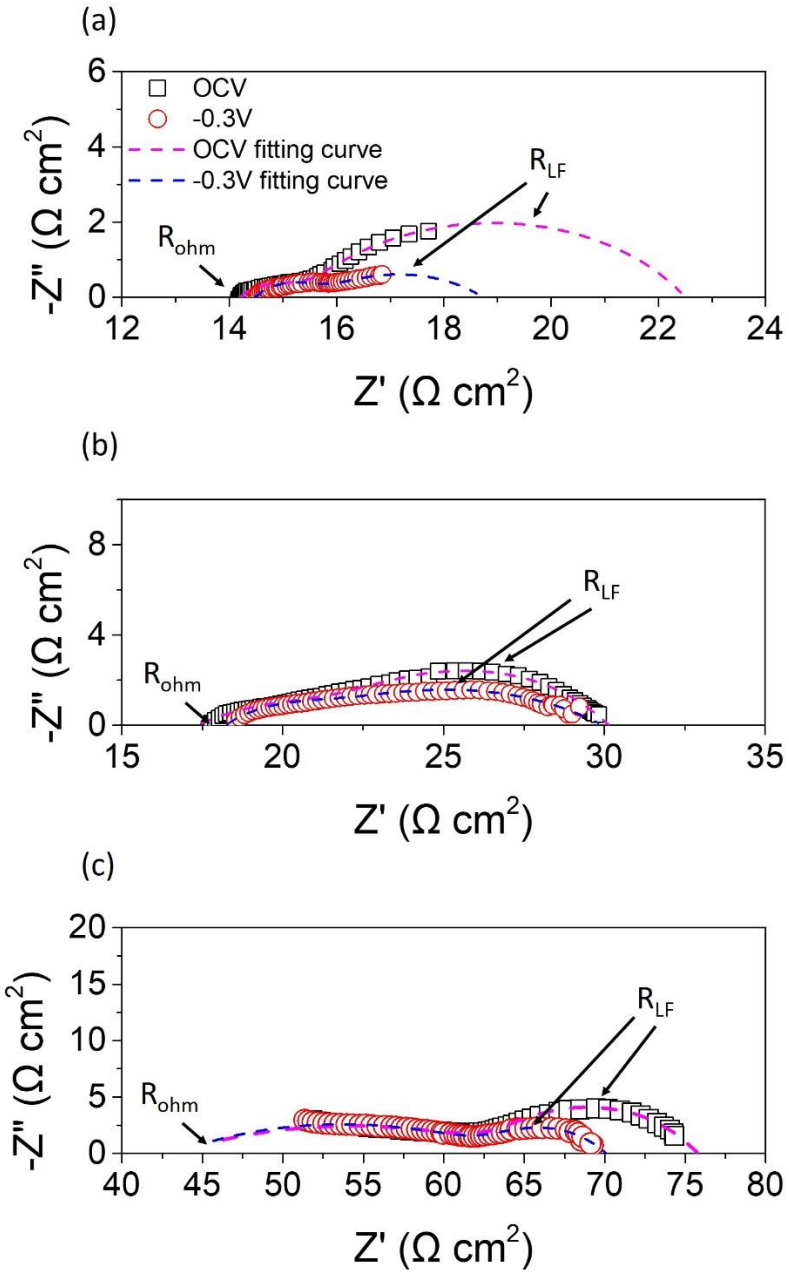

Fig. 3-11 EIS analysis at 600°C for (a) 10Fe−BCY, (b) 0.5W−10Fe−BCY, and (c) 1W−10Fe−BCY.

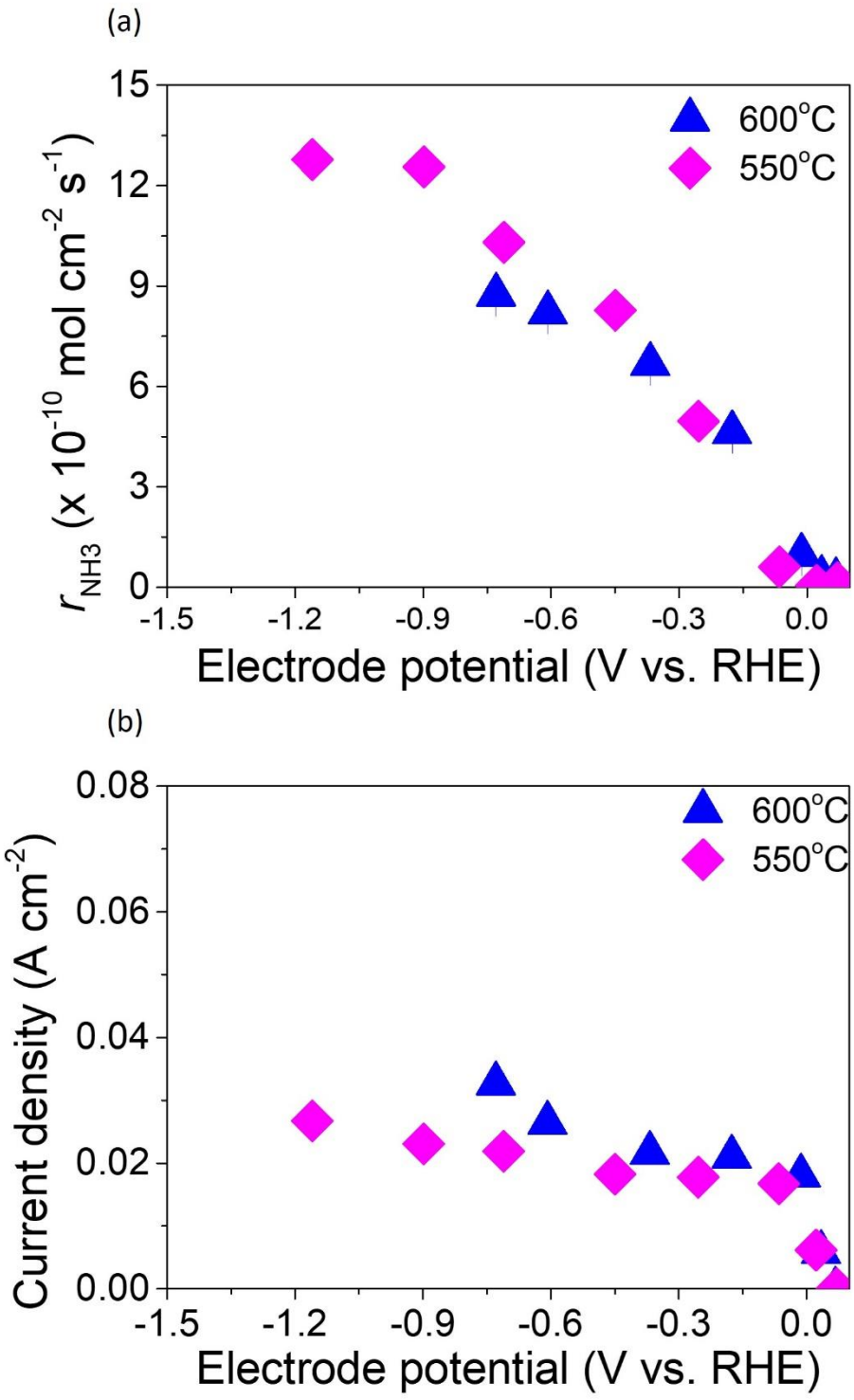

Fig. 3-12 (a) Ammonia formation rate and (b) current density at different temperatures for porous pure Fe cathode.

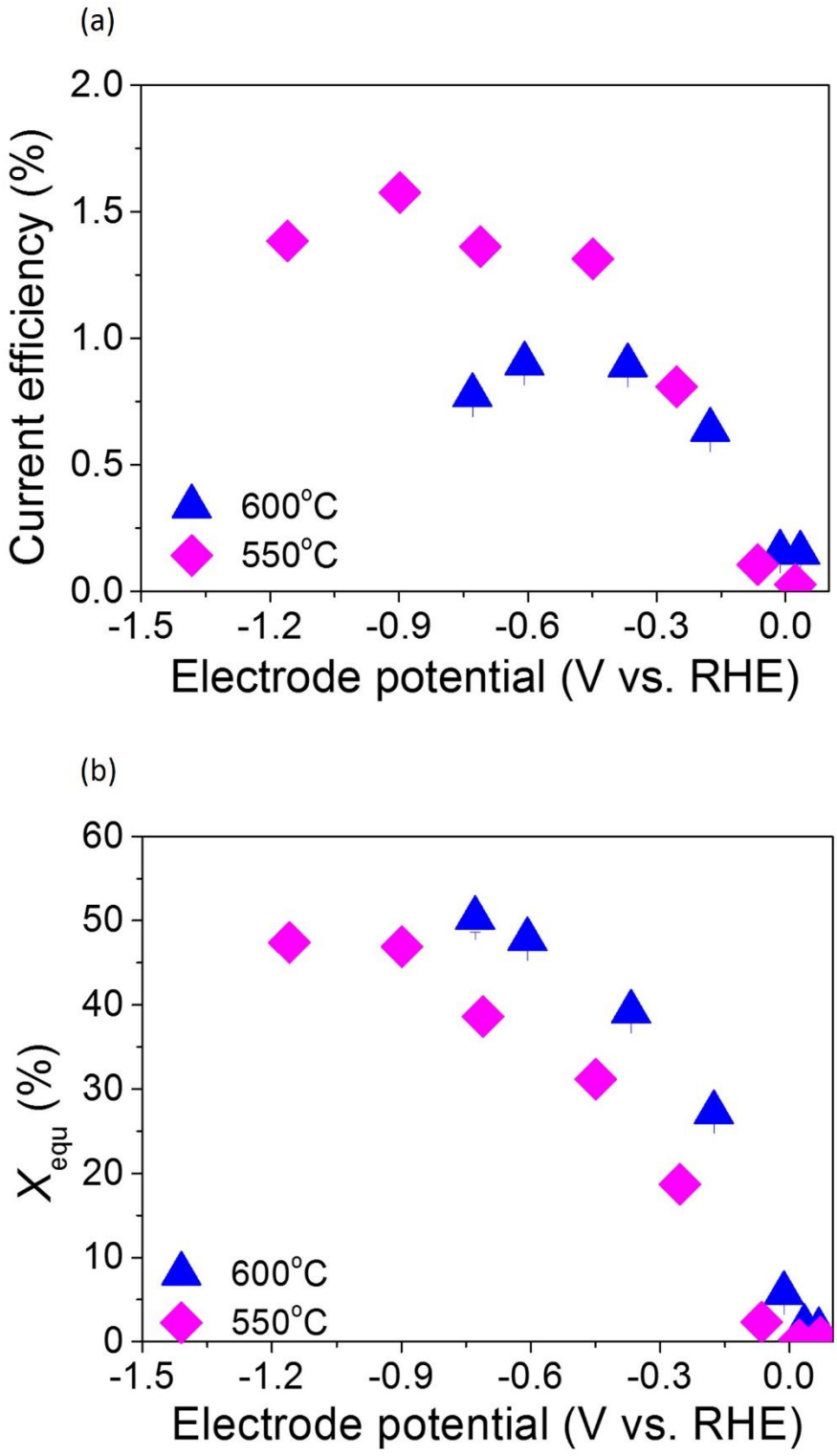

Fig. 3-13 (a) Current efficiency and (b) X_{Equ} at different temperatures for porous pure Fe cathode.

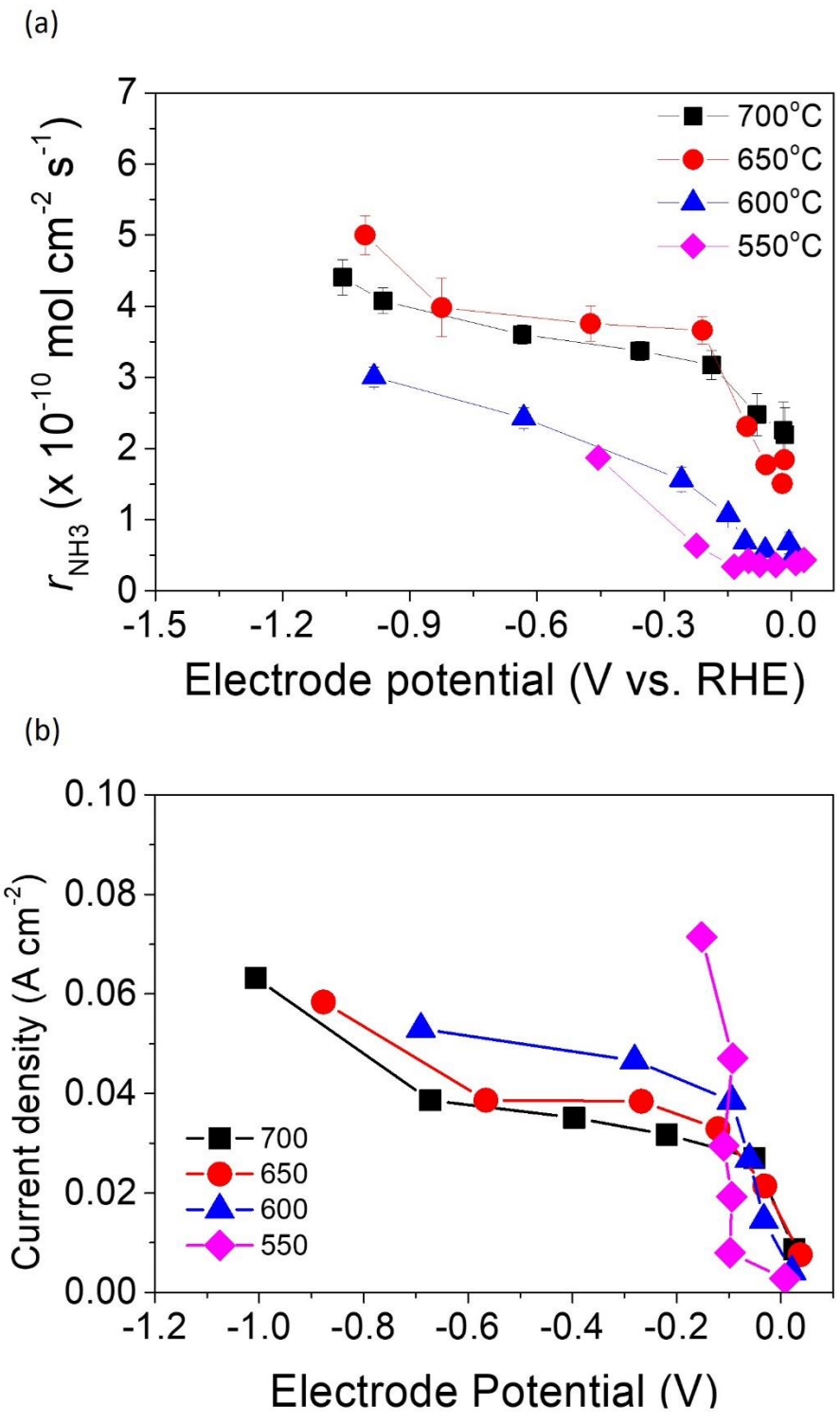

Fig. 3-14 (a) Ammonia formation rate and (b) current density at different temperatures for 20Fe-BCY.

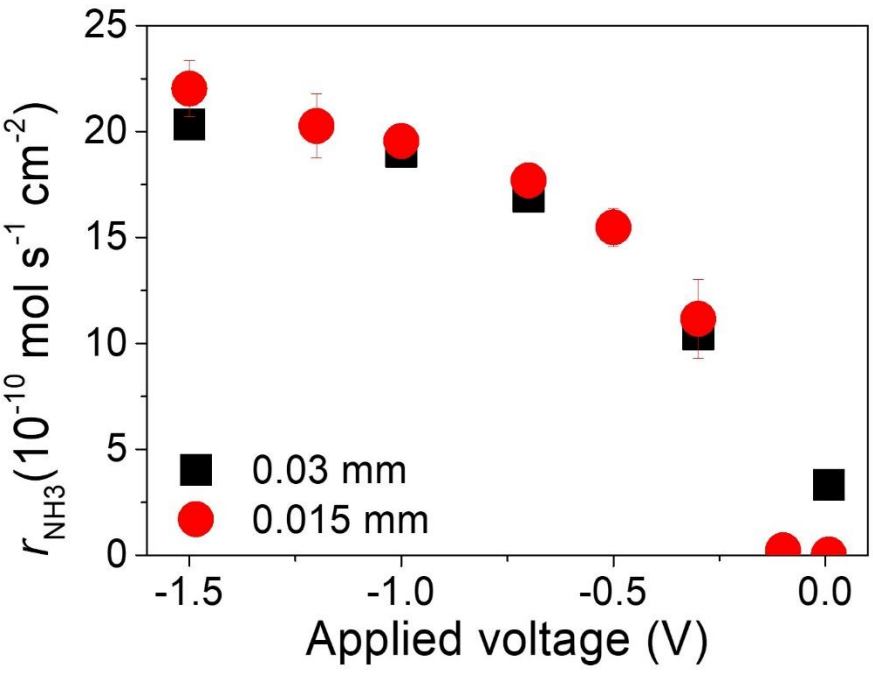

Fig. 3-15 Ammonia formation rates at 550°C for porous pure Fe with 15 and 30 μm.

4. Performance of ammonia synthesis using porous pure Fe cathode

4.1. Introduction

In chapter 3, the best performance in Fe pure porous cathode among all the cathodes was found. However, this is in contradiction with the conventional theory which ammonia electrosynthesis is formed via charge-transfer reaction at TPB because Fe pure porous cathode had relatively low TPB length. Thus, to investigate the detailed reaction mechanism, the kinetics analysis will be discussed in this chapter.

4.2. Reaction orders of hydrogen and nitrogen using porous pure Fe cathodes

Experimental condition

Gas flow in the cathode: H_2–N_2–Ar with 40 sccm

Gas flow in the anode: wet 20%H_2–80%Ar with 30 sccm

Temperature: 550°C

Cathode: Porous pure Fe with 30 μm electrode thickness

To investigate the kinetics of ammonia formation, the reaction orders of hydrogen and nitrogen were examined using porous pure Fe cathode (30 μm electrode thickness). The performance of ammonia formation was conducted in a gaseous mixture of X% H_2–50% N_2–(50-X)% Ar (X=5, 10, 15, 20, and 25) for the reaction order of hydrogen and in a gaseous mixture of 10% H_2–Y %N_2–(90-Y)% Ar (Y=30, 40, 50, and 60) for the reaction order of nitrogen, as shown in Fig. 4-1–Fig. 4-2. Fig. 4-1a shows that the ammonia formation rate increases with an increase in H_2 partial pressure in the cathode. The ratios of ammonia formation rates at -1.3V to that at rest potential are around 3.5–6 at different H_2 partial pressure. Fig. 4-1b shows that the current densities decreased with increasing H_2 partial pressure in the cathode, which is probably caused by the degradations of the cathode and the low overpotential at high H_2 partial pressure because rest potential is more negative at high H_2 partial pressure than that at low H_2 partial pressure in the cathode.

Fig. 4-2 shows the ammonia formation rate at a fixed H_2 partial pressure of 0.1 atm and different N_2 partial pressures. Fig. 4-2a shows a slight increase in the ammonia formation rate when N_2 partial pressure is increased. The current densities were almost the same at different N_2 partial

pressures. Notably, the effect of increasing N_2 partial pressure on ammonia formation rate was weaker than that of increasing H_2 partial pressure.

Fig. 4-3 shows ln(p_{H2}) and ln(p_{N2}) dependence of ln(r_{NH3}). The hydrogen partial pressure used for the horizontal axis in Fig. 4-3a is defined as the sum of hydrogen partial pressure in feed gas and Δp_{H2} from the H_2 evolution reaction. The current efficiency of H_2 evolution reaction is assumed to be 100% (Eq. 1-10), which suggests that H_2 partial pressure in the cathode increases by Δp_{H2} with cathodic polarization (Eq. 4-1).

$$\Delta p_{H2} = \frac{iART}{nFf} \quad 4\text{-}1$$

The slopes in Fig. 4-3a and Fig. 4-3b represent the reaction order for hydrogen, α, and that for nitrogen, β, at different applied voltages, which is calculated by Eq. 4-2.

$$r_{NH3} = k p_{H2}^{\alpha} p_{N2}^{\beta} \quad 4\text{-}2$$

α was around 1.3 at rest potential, which was different with that of 0.72 using K-promoted Fe catalysts, 0.69 using K–Al–Fe–BCY catalysts, and 2.2 using a commercial catalyst (94% Fe–2.8% CaO–2.5% Al_2O_3–0.6% K_2O).[74, 106-108] The high positive value of α indicates that there is no hydrogen poisoning over the Fe catalyst surface, and active interaction with hydrogen and nitrogen adatoms occurs in the surface reaction. Notably, α at applied voltages of –0.3, –0.7, –1 and –1.3 V were around 1.2–1.4, which were most similar to that at rest potential. Also, β was around 0.3 at rest potential, which was smaller than that of 0.52 using K-promoted Fe catalysts or that of 0.8-1.0 using Fe catalysts.[107, 108] The value of β = 1 means that the rate-limiting step is N_2 dissociation over the catalyst surface in the ammonia synthesis. The low value of β in this study indicates the promotion of N_2 dissociation at 550°C. The rate-limiting step probably changes to the combination of nitrogen and hydrogen adatoms over the Fe surface, which is also considered as an alternative reaction mechanism proposed by the model of Stoltze and Nørskov.[9] β was around 0.3−0.4 at different applied voltages, which is closed to that at rest potential. The values of α and β were summarized in Table 4-1. This result shows that both α and β do not change after applying a negative voltage, which suggests that the reaction mechanism with cathodic polarization is the same as that at rest potential.

4.3. Effect of atmosphere in cathode on electrochemical ammonia synthesis

Experimental condition

Gas in the cathode: H_2–N_2 with 40 sccm

Gas in the anode: wet 20% H_2–80% Ar with 30 sccm

Temperature: 550°C

Cathode: porous pure Fe cathode with 15 μm

In the last section, an increase in the ammonia formation rate with increasing H_2 partial pressure was observed. This result is not corresponding to the charge-transfer reaction because ammonia formation from the charge-transfer reaction should not be affected by H_2 partial pressure in the cathode. Therefore, in this section, the performance at different hydrogen partial pressures in the cathode (10–75% H_2–90–25% N_2) was examined using the porous pure Fe cathode (15 μm electrode thickness), as shown in Fig. 4-4. With increasing H_2 partial pressure in the cathode, the ammonia formation rate also increased by 6 times from 2.2×10^{-9} mol s^{-1} cm^{-2} in a gaseous mixture of 10% H_2–90% N_2 to 1.4×10^{-8} mol s^{-1} cm^{-2} in that of 50% H_2–50% N_2 at −1.2 V. In a gaseous mixture of 50% H_2–50% N_2, the ammonia formation rate increased by about 220 times to 1.4×10^{-8} mol s^{-1} cm^{-2} (450 μg h^{-1} mg^{-1}) at around −1.2 V compared with that at rest potential, which is the highest ammonia formation. Notably, the highest ammonia formation rate was obtained in 50% H_2–50% N_2 rather than at the nominal composition of 75% H_2–25% N_2 because ammonia formation depends on temperature, pressure, and hydrogen coverage on the catalyst surface rather than the nominal stoichiometric ratio of H_2/N_2 in the cathode.

Fig. 4-5 shows the current efficiency and X_{Equ} at different H_2 and N_2 partial pressures. Although the current densities were similar at different H_2 and N_2 partial pressures, the current efficiency increased by 4.4 times from 2.7% in a gaseous mixture of 10% H_2–90% N_2 to 14.5% in that of 50% H_2–50% N_2. X_{Equ}, however, decreased from 42% to 32% because of the high NH_3 partial pressure at equilibrium in a gaseous mixture of 10% H_2–90% N_2. This result shows that a positive effect of increasing H_2 partial pressure in the cathode on the ammonia formation rate was observed in the electrochemical reaction. However, based on the charge-transfer reaction at the TPB for ammonia formation (Eqs. 1-11−1-12), the ammonia formation rate should be independent of H_2 partial pressure in the cathode, which contradicts the result of the relationship between ammonia formation rate and H_2 partial pressure in the cathode. Therefore, this result also implies that the mechanism of electrochemical ammonia formation is followed via the surface reaction.

4.4. Influence of flow rate on electrochemical ammonia synthesis

Experimental condition

Gas flow in the cathode: 50% H_2–50% N_2

Gas flow in the anode: wet 20% H_2–80% Ar with 30 sccm

Temperature: 550°C

Cathode: porous pure Fe cathode with 15 μm

In this section, the ammonia formation rate was investigated using porous pure Fe (15 μm electrode thickness) between the flow rate of 40 and 700 sccm in the cathode at −1.2 V, as shown in Fig. 4-6. The gaseous mixture of flow gas is 50% H_2–50% N_2. Fig. 4-6a shows that the ammonia formation rate increased from 1.2×10^{-8} mol s^{-1} cm^{-2} with 40 sccm to 5.5×10^{-8} mol s^{-1} cm^{-2} (1800 μg mg^{-1} h^{-1}) with 700 sccm, whereas the current density decreased with increasing the flow rate, which is probably caused by that the inlet gas at ambient temperature decreased the surface temperature of cathode in a high flow rate. Fig. 4-6b shows that the current efficiency increased from 8% with 40 sccm to 60% with 700 sccm, while X_{Equ} decreased with increasing the flow rate, which represents that the obtained NH_3 partial pressure in the cathode decreased with increasing the flow rate.

4.5. Conclusion

1. The reaction orders of hydrogen and nitrogen at rest potential are mostly similar to those with cathodic polarization, which indicates that the reaction mechanism with cathodic polarization is the same as that at rest potential.
2. The ammonia formation rate can be controlled by changing H_2 partial pressure in the cathode. This result agrees with that ammonia is formed via the surface reaction rather than the charge-transfer reaction at the TPB.
3. With increasing the flow rate in the cathode, the ammonia formation rate and current efficiency increase as well, whereas the current density and X_{Equ} decrease. In our study, the highest ammonia formation rate of 5.5×10^{-8} mol cm^{-2} s^{-1} (1800 μg mg^{-1} h^{-1}) occurs in a gaseous mixture of 50% H_2–50% N_2 with 700 sccm at 550°C in the electrochemical reaction.

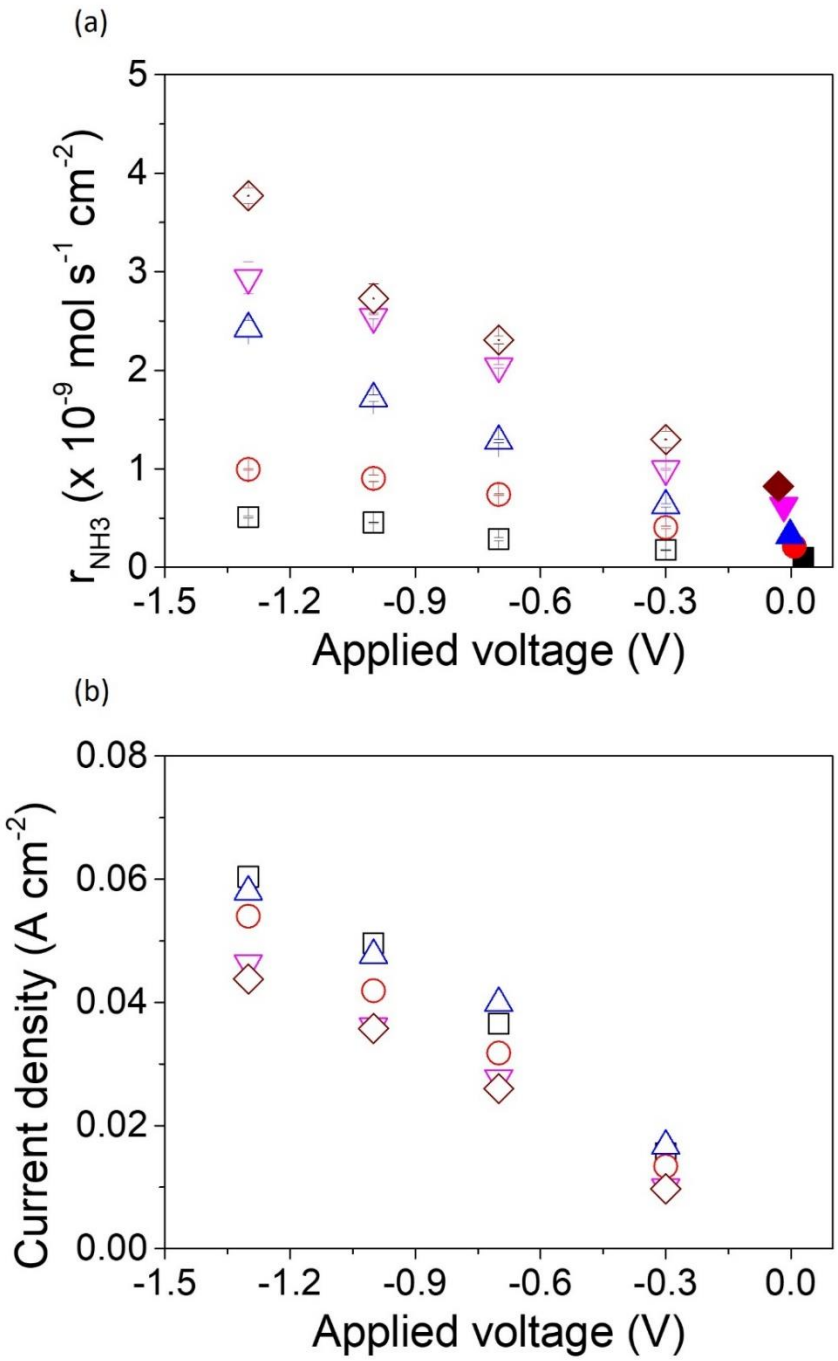

Fig. 4-1 (a) ammonia formation rate and (b) current density using porous pure Fe cathode (30 μm) at 550°C and different H_2 partial pressures. ■ 5% H_2−50% N_2 at rest potential. □ 5% H_2−50% N_2 with cathodic polarization. ● 10% H_2−50% N_2 at rest potential. ○ 10% H_2−50% N_2 with cathodic polarization. ▲ 15% H_2−50% N_2 at rest potential. △ 15% H_2−50% N_2 with cathodic polarization. ▼ 20% H_2−50% N_2 at rest potential. ▽ 20% H_2−50% N_2 with cathodic polarization. ◆ 25% H_2−50% N_2 at rest potential. ◇ 25% H_2−50% N_2 with cathodic polarization.

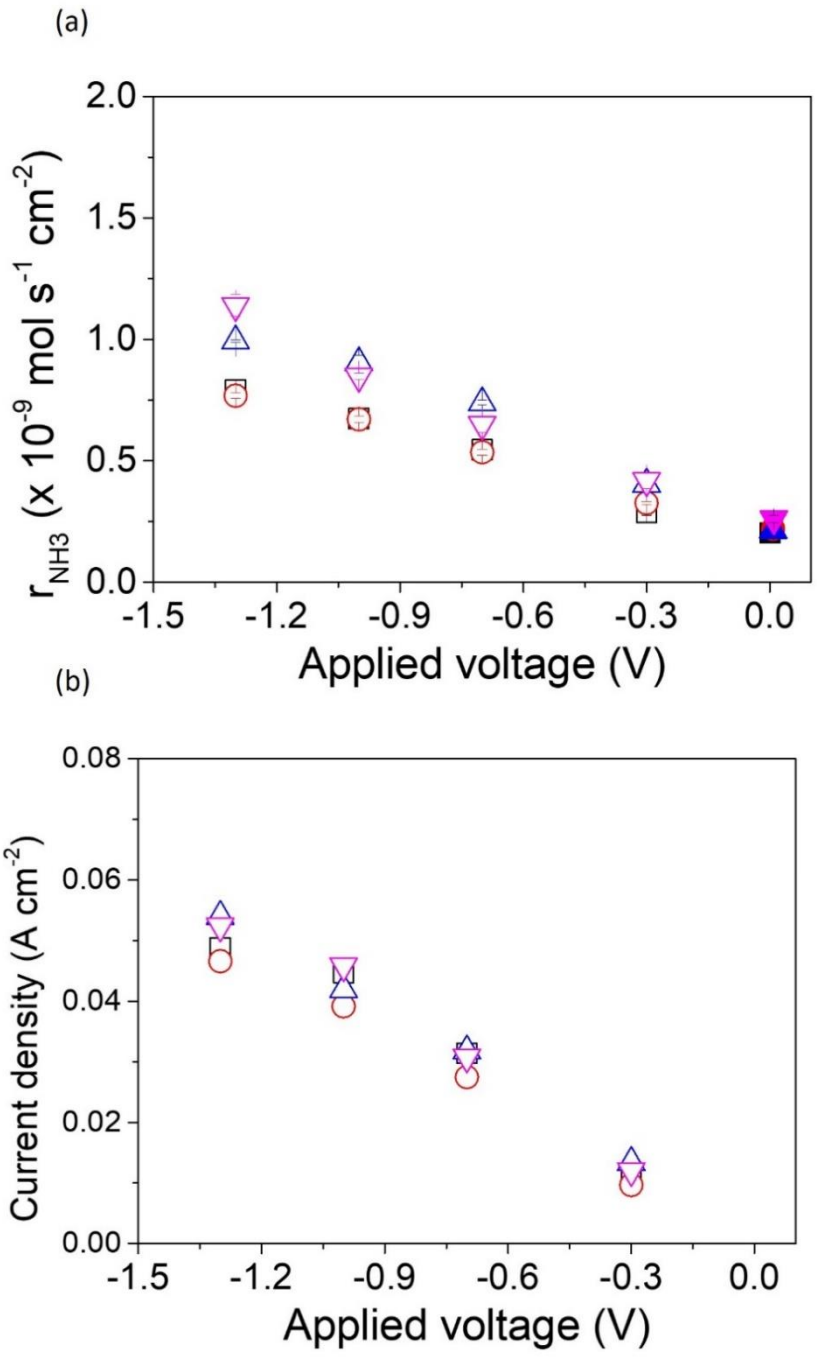

Fig. 4-2 (a) ammonia formation rate and (b) current density using porous pure Fe cathode (30 μm) at 550°C and different N_2 partial pressures. ■ 10% H_2−30% N_2 at rest potential. □ 10% H_2−30% N_2 with cathodic polarization. ● 10% H_2−40% N_2 at rest potential. ○ 10% H_2−40% N_2 with cathodic polarization. ▲ 10% H_2−50% N_2 at rest potential. △ 10% H_2−50% N_2 with cathodic polarization. ▼ 10% H_2−60% N_2 at rest potential. ▽ 10% H_2−60% N_2 with cathodic polarization.

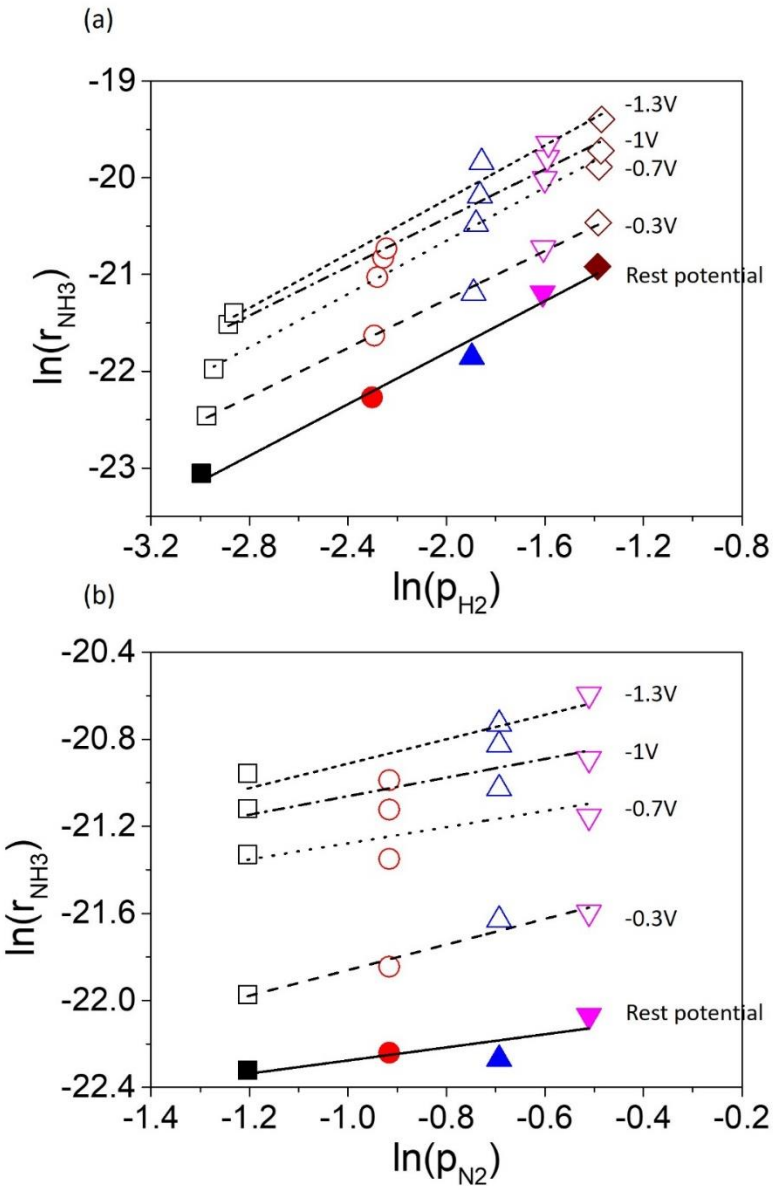

Fig. 4-3 (a) ln(r_{NH3}) vs. ln(p_{H2}) at 550°C ■ 5% H_2−50% N_2 at rest potential. □ 5% H_2−50% N_2 with cathodic polarization. ● 10% H_2−50% N_2 at rest potential. ○ 10% H_2−50% N_2 with cathodic polarization. ▲ 15% H_2−50% N_2 at rest potential. △ 15% H_2−50% N_2 with cathodic polarization. ▼ 20% H_2−50% N_2 at rest potential. ▽ 20% H_2−50% N_2 with cathodic polarization. ◆ 25% H_2−50% N_2 with cathodic polarization. ◇ 25% H_2−50% N_2 with cathodic polarization. (b) ln(r_{NH3}) vs. ln(p_{N2}) at 550°C ■ 10% H_2−30% N_2 at rest potential. □ 10% H_2−30% N_2 with cathodic polarization. ● 10% H_2−40% N_2 at rest potential. ○ 10% H_2−40% N_2 with cathodic polarization. ▲ 10% H_2−50% N_2 at rest potential. △ 10% H_2−50% N_2 with cathodic polarization. ▼ 10% H_2−60% N_2 at rest potential. ▽ 10% H_2−60% N_2 with cathodic polarization.

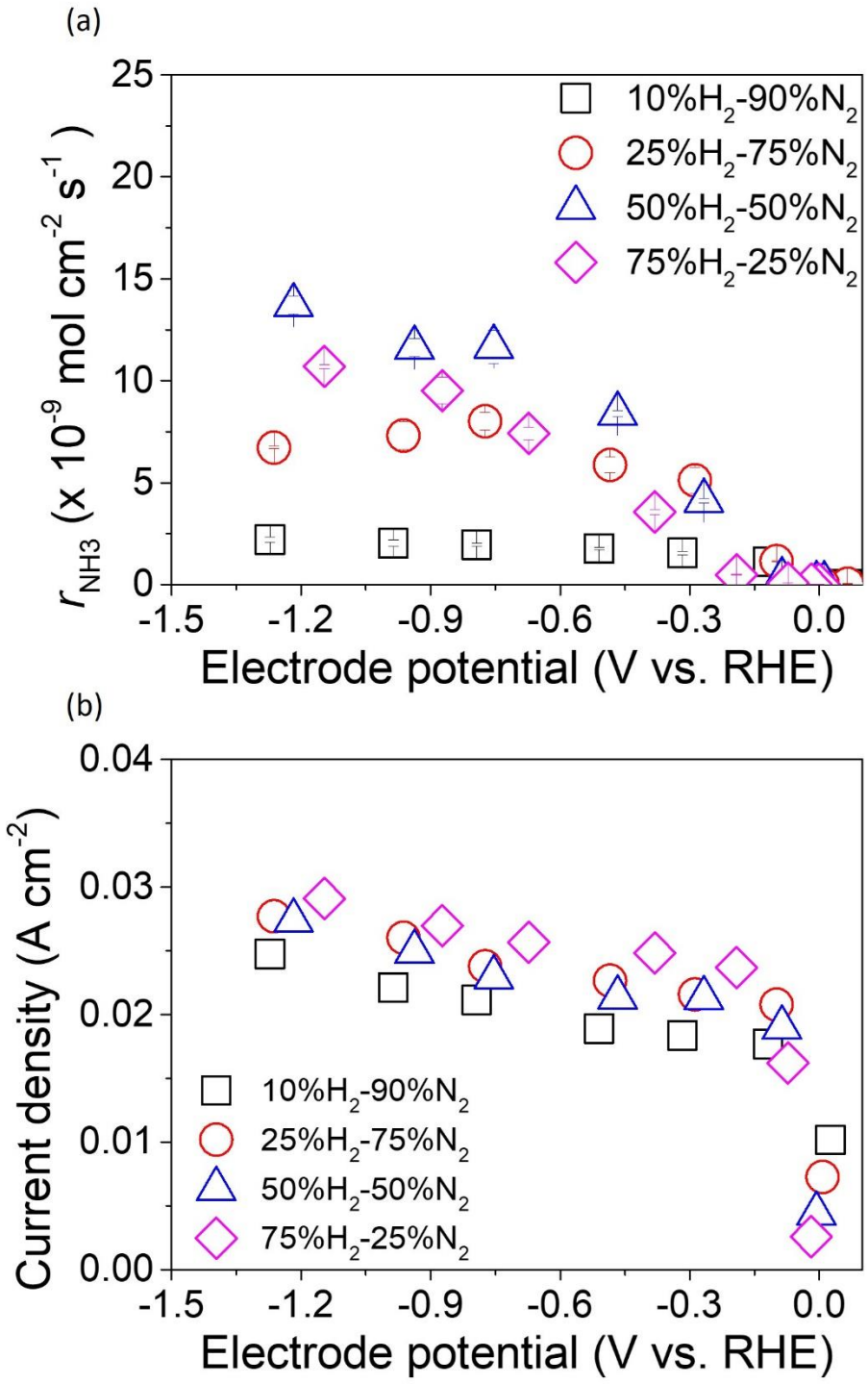

Fig. 4-4 (a) Ammonia formation rate and (b) current density at 550°C with different H_2/N_2 ratios for porous pure Fe cathode.

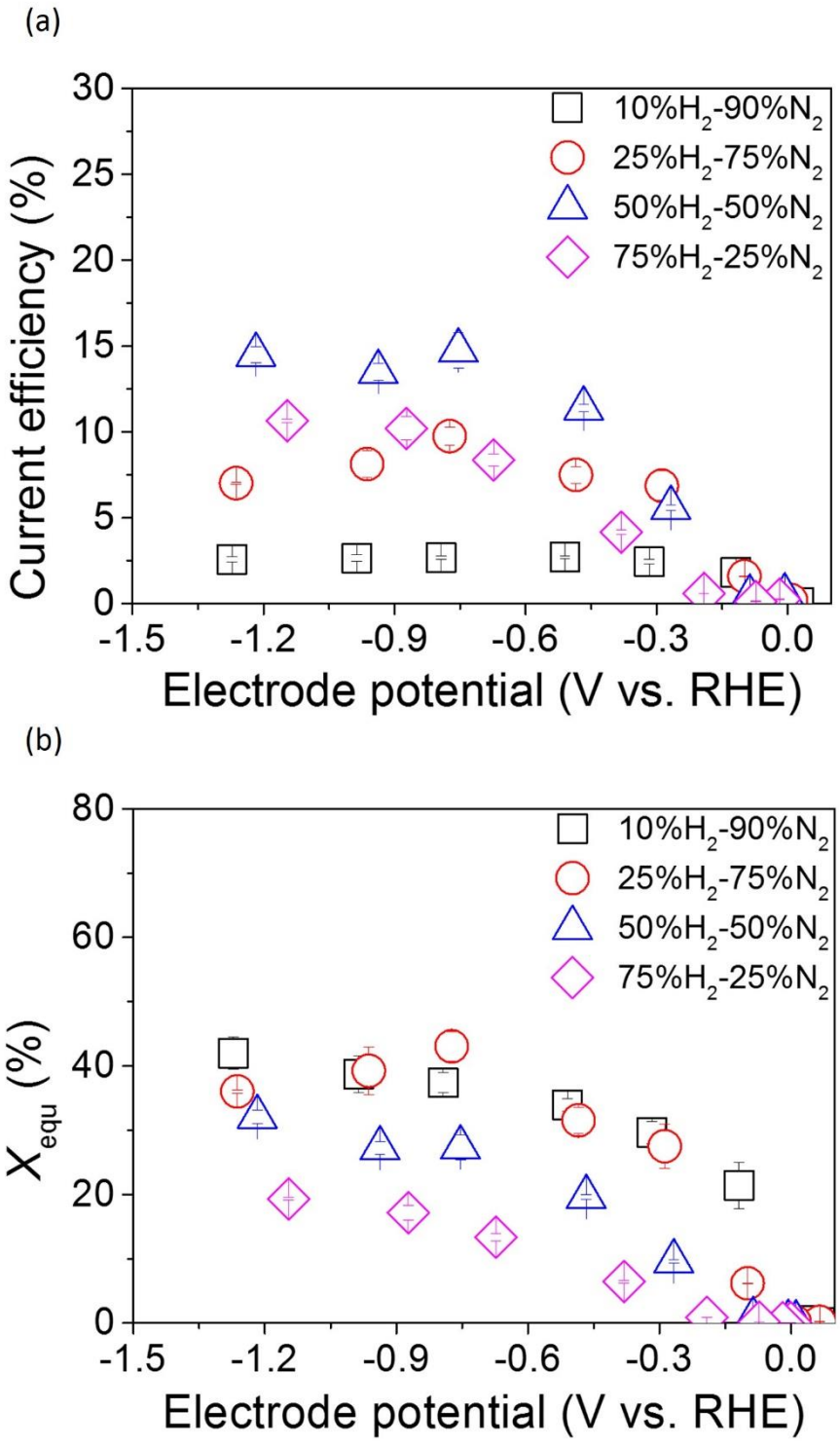

Fig. 4-5 (a) Current efficiency and (b) X_{equ} at 550°C with different H_2/N_2 ratios for porous pure Fe cathode.

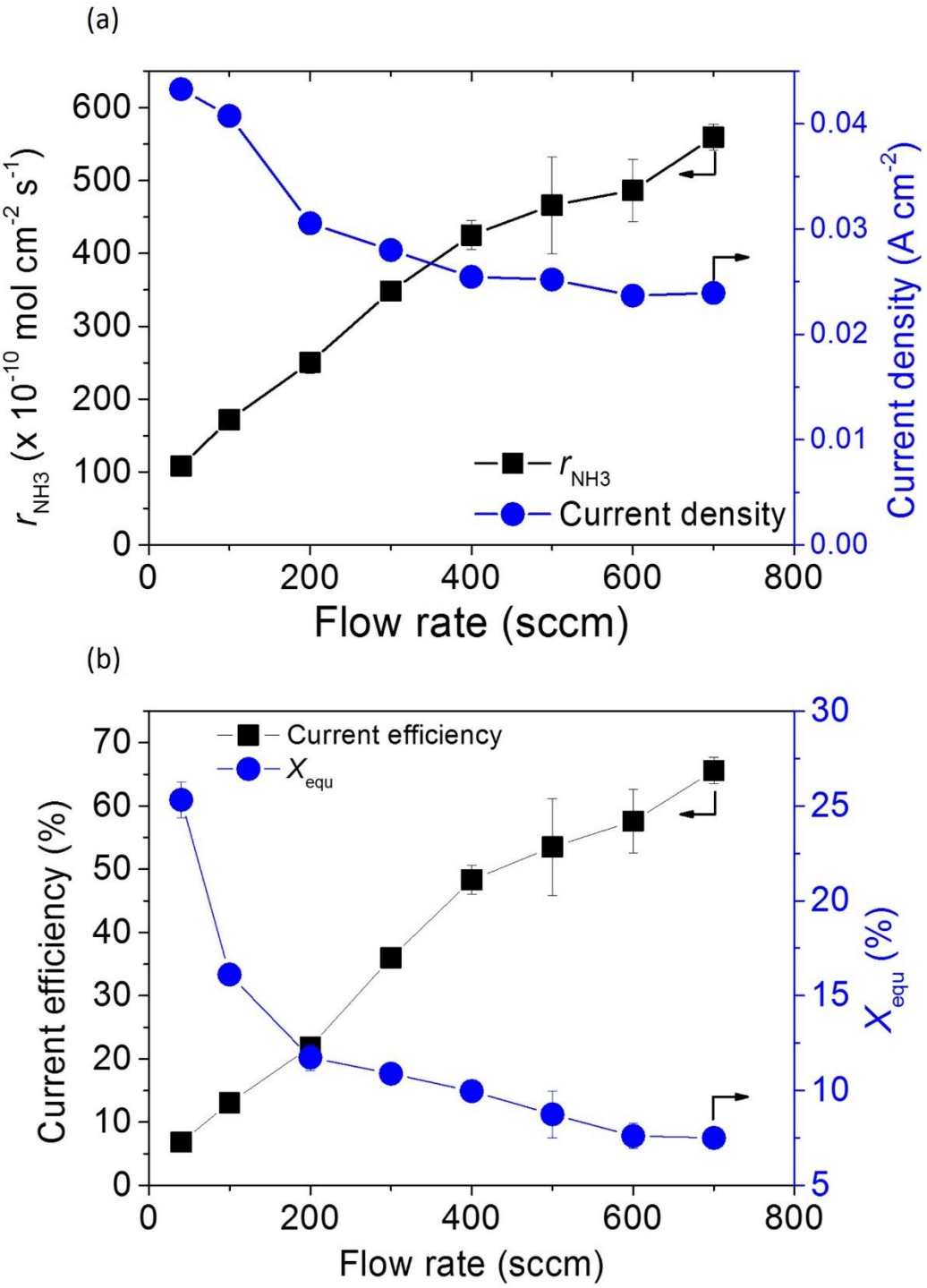

Fig. 4-6 (a) ammonia formation rate and current density, and (b) current efficiency and X_{Equ} with different flow rates at 550°C for porous pure Fe cathode.

Table 4-1 α and β at different applied voltage.

	Rest potential	−0.3V	−0.7V	−1V	−1.3V
α	1.33 ± 0.11	1.26 ± 0.04	1.38 ± 0.06	1.26 ± 0.09	1.40 ± 0.13
β	0.30 ± 0.15	0.59 ± 0.09	0.37 ± 0.25	0.43 ± 0.21	0.56 ± 0.20

5. Deuterium isotopic analysis with FTIR for electrochemical promotion of ammonia synthesis

5.1. **Introduction**

In chapters 3 and 4, the performance of ammonia formation was investigated by controlling different parameters, including the cathode structure, the amount of Fe, H_2 partial pressure in the cathode, and flow rate in the cathode. Based on the results, the reaction mechanism of ammonia formation is dominated by the surface reaction in the electrochemical reaction. In this chapter, through the observation of ammonia composition ($NH_{3-x}D_x$) formed in the cathode, the dominant mechanism for the ammonia formation, the charge-transfer reaction or surface reaction, was discussed in the electrochemical reaction. For example, when gaseous mixtures of D_2−N_2 and H_2−Ar are introduced into the cathode and anode, respectively, if ammonia is formed via the surface reaction (Eqs. 5-1−5-7), the product should be ND_3. If the charge-transfer reaction is dominating in the reaction (Eqs. 5-8−5-15), the product should be NH_3. According to the ammonia composition, the details of ammonia formation mechanism can be revealed.

Surface reaction

$N_2 + * \rightarrow N_2*$ 5-1

$N_2* + * \rightarrow 2N*$ 5-2

$D_2 + 2* \rightarrow 2D*$ 5-3

$N* + D* \rightarrow ND* + *$ 5-4

$ND* + D* \rightarrow ND_2* + *$ 5-5

$ND_2* + D* \rightarrow ND_3* + *$ 5-6

$ND_3* \rightarrow ND_3 + *$ 5-7

Charge-transfer reaction

$N_2* + H^+ + e^- \rightarrow N_2H*$ 5-8

$N_2H* + H^+ + e^- \rightarrow N_2H_2*$ 5-9

$N_2H_2* + H^+ + e^- \rightarrow N_2H_3*$ 5-10

$N_2H_3* \rightarrow N* + NH_3$ 5-11

$$N^* + H^+ + e^- \rightarrow NH^* \quad 5\text{-}12$$

$$NH^* + H^+ + e^- \rightarrow NH_2^* \quad 5\text{-}13$$

$$NH_2^* + H^+ + e^- \rightarrow NH_3^* \quad 5\text{-}14$$

$$NH_3^* \rightarrow NH_3 + * \quad 5\text{-}15$$

5.2. Deuterium isotope analysis

In this section, the ammonia compositions ($NH_{3-x}D_x$) were investigated by FTIR. The v_2 band (umbrella mode) of $NH_{3-x}D_x$ was chosen because of the high intensity. In the v_2 band, a degenerated energy level, which is caused by that the barrier of umbrella inversion for nitrogen atom pass through the three hydrogen atoms plane, produces two energy levels, symmetric state and asymmetric state, as shown in Fig. 5-1. The doublet causes two Q branches in IR spectrum of NH_3.[109]

According to the selection rule, the rotational-vibrational transitions need to be satisfied with two conditions: 1) the symmetric state to the asymmetric state or the asymmetric state to the symmetric state; 2) the vibrational quantum number, v, the quantum number for total angular momentum, J, and the quantum number for the projection of J onto the principal axis of the molecule, K, need to be satisfied with $\Delta v = 1$, $\Delta J = \pm 1, 0$, and $\Delta K = 0$. The rotational-vibrational transitions in the ν_2 band are shown in Fig. 5-2. The transitions with ΔJ equal to 0, 1, and −1 are corresponding to Q, P, and R branches, respectively. The wavenumbers of Q, P, and R branches for $NH_{3-x}D_x$ are summarized in Appendix H. In this study, only Q branches, which represent the transition from the symmetric to the asymmetric states ($0_s \rightarrow 1_a$), and Q' branches, which represent the transition from the asymmetric to the symmetric states ($1_s \rightarrow 0_a$), of $NH_{3-x}D_x$ are marked because of their high intensities.

5.2.1. Absorption coefficient of $NH_{3-x}D$

To calculate the ammonia concentration, the absorption coefficient, α_i, is an essential parameter, which is determined by Eq. 5-16:

$$\alpha_i = \frac{A}{C_i L} \quad 5\text{-}16$$

where A, C_i, and L are the area of the peak in FTIR spectrum, ammonia concentration (i = $NH_{3-x}D_x$), and optical length of 8 m.

NH_3 absorption coefficient, α_{NH3}, was determined by flowing 10 ppm NH_3-N_2 into the cathode with 100 sccm. The ammonia concentration of 5.07 ppm in the cathode was obtained by the HPLC, and the corresponding area of NH_3 peak at 965 cm^{-1} was 0.13 in the IR spectrum. Therefore, α_{NH3} was 0.0032 ppm^{-1} m^{-1}, which is smaller than that of 0.0039 ppm^{-1} m^{-1} in the previous study.[110] α_{NH2D} was determined by the IR spectra at rest potential (90 mins) and at −1 V (90 mins), as shown in Fig. 5-3. α_{NHD2} and α_{ND3} were obtained by Eq. 5-17:

$$\frac{A_{ND3}}{\alpha_{ND3}L} + \frac{A_{NHD2}}{\alpha_{NHD2}L} = C_{total} - C_{NH3} - C_{NH2D} \quad 5\text{-}17$$

where C_{total} was the total concentration of ammonia, which was determined by the HPLC.
Eq. 5-17 could be written by Eq. 5-18:

$$A_{ND3} = -\frac{\alpha_{ND3}}{\alpha_{NHD2}} A_{NHD2} + (C_{total} - C_{NH3} - C_{NH2D}) L \alpha_{ND3} \quad 5\text{-}18$$

α_{NHD2} and α_{ND3} were determined by the IR spectra at −1 V (50, 60, 70, 80, and 90 mins), as shown in Fig. 5-4.

5.2.2. D_2–N_2–Ar in the cathode and H_2–Ar in the anode

Experimental condition

Gas flow in the cathode: 5% D_2–45% Ar–50% N_2 with 100 sccm

Gas flow in the anode: wet 10% H_2–90% Ar with 30 sccm

Temperature: 550°C

Cathode: porous pure Fe cathode with 30 μm

To investigate the origin of the hydrogen (deuterium) atoms in the ammonia, deuterium isotope analysis was conducted to analyze the ammonia compositions with FTIR. The cell operation condition was 10% H_2−90% Ar, Pt |BCY| Fe, 5% D_2−45% Ar−50% N_2 at 550°C. Fig. 5-5 shows the IR spectra and ammonia concentrations at rest potential. The NH_2D, NHD_2, and ND_3 concentrations were stable after 50 mins in the optical cell. At rest potential, the ammonia product was supposed to be only ND_3 because H^+ could not be supplied, whereas ND_3, NHD_2, and NH_2D were detected at rest potential. Here are two possible reasons for NHD_2 and NH_2D formation. The first reason is the exchange reactions with ND_3 and H_2O to form NH_2D and NHD_2 (Eqs. 5-19 and 5-20). The second reason is hydrogen atoms, which diffuse from the anode to the cathode due to the gradient of H_2 concentration, reacting with nitrogen and deuterium to form NH_2D and NHD_2.

$ND_3 + H_2O = NHD_2 + HDO$ 5-19

$NHD_2 + H_2O = NH_2 + HDO$ 5-20

Subsequently, the ammonia compositions were investigated at a voltage of −1 V, as shown in Fig. 5-6. The intensities of ND_3, NHD_2, NH_2D, and NH_3 peaks increased before 20 mins, and then became stable after 20 mins. The details of electrochemical promotion of ammonia formation will be discussed in section 5.2.3.

Finally, the concentrations of ammonia compositions were examined in the closed optical cell, i.e. the valves for gas outlet and gas inlet were closed. The intensities of ND_3 peaks exhibited a decrease with elapsed time, whereas the intensities of NH_3 and NH_2D peaks slightly increased with elapsed time, and the intensities of NHD_2 peaks became stable, as shown in Fig. 5-7. The result indicated that ND_3 decomposed in the closed optical cell.

5.2.3. Mechanism of electrochemical promotion of ammonia formation

In the electrochemical reaction, if the electrochemical ammonia formation is followed by the charge-transfer reaction, the main product should be NH_3 at −1 V (Eqs. 5-8−5-15). Fig. 5-6 shows that the concentration of ND_3 increased by approximately 3.5 ppm(4 ppm → 7.5 ppm), whereas the concentrations of NHD_2, NH_2D, and NH_3 increased by approximately 0.8, 0.4, and 0.16 ppm, respectively, at −1 V. Therefore, this assumption contradicts the fact that the main product of ND_3 at −1 V, which suggests that the electrochemical ammonia formation is dominated by the surface reaction (Eqs. 5-1−5-7).

For the products of NHD_2, NH_2D, and NH_3, the H atoms in these three products probably originated from three pathways: 1) the surface reaction with adsorbed N and H atoms, which diffused from the anode; 2) the exchange reaction with H_2O; 3) the charge-transfer reaction. To investigate the contribution of the charge-transfer reaction to ammonia formation, that all H atoms originated from the charge-transfer reaction was assumed. The current efficiency for H^+ as mobile cation, Λ_H, can be obtained by Eq. 5-21:

$$\Lambda_H = \frac{i_{NH_{3-x}D_x} Fn}{i} = \frac{\left(c_{NH_{3-x}D_x,-1V} - c_{NH_{3-x}D_x,0}\right) f}{RTAi} \quad 5\text{-}21$$

where $i_{NH_{3-x}D_x}$, $c_{NH_{3-x}D_x,-1V}$, and $c_{NH_{3-x}D_x,0}$ are the current density for ammonia formation, concentration of $NH_{3-x}D_x$ at −1 V, and concentration of $NH_{3-x}D_x$ at rest potential, respectively. Notably, the electron transfer number are 3, 2, and 1 for NH_3, NH_2D, and NHD_2, respectively,

because only H atoms form via the charge-transfer reaction. The obtained current efficiency is about 0.12%, which is very low in an electrochemical reaction. Thus, the charge-transfer reaction is not dominant in this system.

5.2.4. H_2–N_2–Ar in the cathode and D_2–Ar in the anode

Experimental condition

Gas flow in the cathode: 5% H_2–95% N_2 with 100 sccm

Gas flow in the anode: wet 10% D_2–90% Ar with 30 sccm

Temperature: 550°C

Cathode: porous pure Fe cathode with 30 μm

The deuterium isotope analysis was also conducted under the condition of 5% H_2−95% N_2 in the cathode and 10% D_2−90% Ar in the anode. Fig. 5-8 shows the ammonia compositions at rest potential. The main product of NH_3 is formed by the surface reaction without cathodic polarization, and NH_2D should be formed via the surface reaction with N, H, and D diffused from the anode.

Then, the ammonia compositions were detected at an applied voltage of −1 V, as shown in Fig. 5-9. The concentrations of the product NH_3 and NH_2D increased by approximately 0.9 and 0.5 ppm, respectively, which indicates that the main product is NH_3 formed via the surface reaction in the electrochemical reaction. This result is supported by the result in section 5.2.3.

Finally, the concentrations of ammonia compositions were examined in the closed optical cell. The intensities of NH_3 and NH_2D peaks are stable with elapsed time, as shown in Fig. 5-10.

5.2.5. The effect of applied voltages on surface reaction and charge-transfer reaction

Experimental condition

Gas flow in the cathode: 5% H_2–95% N_2 with 100 sccm and 3% H_2–95% N_2 with 100 sccm

Gas flow in the anode: wet 10% D_2–90% Ar with 30 sccm

Temperature: 550°C

Cathode: porous pure Fe cathode with 30 μm

To investigate the contribution of the charge-transfer reaction under the condition of 5% H_2–95% N_2 in the cathode and 10% D_2–90% Ar in the anode, the ammonia compositions were examined at

–0.3, –0.7, and –1 V, as shown in Fig. 5-11. Fig. 5-11 shows that the concentrations of NH_3 and NH_2D were corresponding to H_2 and D_2 partial pressure in the cathode, respectively. The H_2 and D_2 partial pressure can be represented by H_2 flux and D^+ flux (upper X-axis).

In Fig. 5-11a, 2.2 ppm NH_3 was detected in 5% H_2 at rest potential. The enhancement of NH_3 concentration increased with increasing the applied voltage although H_2 partial pressure is the same with cathodic polarization. This result indicated that the contribution of surface reaction on ammonia formation rate is influenced by the applied voltage. When 5% H_2 was decreased to the 3% H_2, the ammonia concentration at rest potential decreased to 1.3 ppm, and the enhancement of NH_3 concentration decreased at the same applied voltage, which suggests that the promotion of ammonia formation via the surface reaction is also affected by H_2 partial pressure in the cathode.

In Fig. 5-11b, a small amount of D_2 diffused from anode to the cathode to react with N and H adatoms to form 0.5 ppm NH_2D at the rest potential. Based on the calculation, D_2 partial pressure was 7.6×10^{-7} atm at rest potential (see Appendix I). When a voltage of −0.3 V was applied, the D_2 partial pressure and D^+ flux increased by several hundred times, while the NH_2D concentration increased by around 29%. Even though the applied voltage was increased to −1 V, the D_2 partial pressure and D^+ flux increased by around one thousand times, but the NH_2D concentration increased by around 68%. This result shows that an increase in current density, i.e. D^+ flux, cannot promote the charge-transfer reaction.

NH_2D was formed via the surface reaction with H_2, D_2, and N_2 at rest potential. When a voltage was applied (–0.3 − –1.0 V), the D_2 partial pressure increased with increasing the current density because of pumped D^+ cation (i.e. current density) and NH_2D concentration increased with increasing the applied voltage as well. However, the D^+ flux at an applied voltage was larger by hundreds of times than that at rest potential, whereas NH_2D concentration only increased by around 29%−68%, which suggests that an increase in the D^+ flux (i.e. current density) cannot promote the charge-transfer reaction. Here, supposing that all D atoms originated from the charge-transfer reaction, the current efficiency of around 0.01 – 0.06% for D^+ as mobile cation, Λ_D, can be obtained by Eq. 5-21. To calculate the contribution of ammonia formation rate from the charge-transfer reaction, that the current efficiency is approximately 0.1% and that the current efficiency does not change with H_2 partial pressure in the cathode are assumed. In Fig. 4-1(a) (the sample in Fig. 4-1 and Fig. 5-11 was the same), the ammonia formation rate, $r_{NH3,total}$, at −1.3 V could be divided into three contributions: ammonia formation rate from (a) catalytic reaction, $r_{NH3,0}$, (b) charge-transfer

reaction, $r_{NH3,CT}$, and (c) surface reaction, $r_{NH3,sur}$, as shown in Fig. 5-12. $r_{NH3,0}$ was corresponding to the ammonia formation rate at the rest potential. $r_{NH3,CT}$ was around 3×10^{-10} mol s^{-1} cm^{-2} because the current efficiency was assumed as 0.1% and was independent of H_2 partial pressure. $r_{NH3,sur}$ could be obtained by Eq. 5-22. In Fig. 5-12, $r_{NH3,sur}$ increased from 2.7×10^{-10} mol s^{-1} cm^{-2} in 5%H_2 partial pressure to 2.7×10^{-9} mol s^{-1} cm^{-2} in 25%H_2 partial pressure, which indicates that the $r_{NH3,sur}$ can be significantly improved by H_2 supply in the cathode. Also, although $r_{NH3,sur}$ was much higher than $r_{NH3,CT}$ in 25%H_2 partial pressure, $r_{NH3,sur}$ and $r_{NH3,CT}$ showed a similar rate in 5%H_2 partial pressure. This result indicates that $r_{NH3,sur}$ is dominant at high H_2 partial pressure, whereas $r_{NH3,sur}$ is dominant at low H_2 partial pressure (lower than 5%H_2 partial pressure).

$$r_{NH3,sur} = r_{NH3,total} - r_{NH3,0} - r_{NH3,CT} \quad 5\text{-}22$$

Therefore, through the observation of ammonia compositions, the main electrochemical promotion of ammonia formation is caused by the surface reaction rather than the charge-transfer reaction at the TPB. Furthermore, the electrochemical promotion of ammonia formation via the surface reaction is affected by the applied voltage and the hydrogen partial pressure in the cathode, whereas the contribution of the charge-transfer reaction to ammonia cannot improve by increasing current density or applied voltage.

5.3. Conclusion

1. Based on the deuterium isotope analysis, through the observation of ammonia composition ($NH_{3-x}D_x$) formed in the cathode, the main reaction mechanism is followed by the surface reaction rather than the charge-transfer reaction at TPB.
2. The electrochemical promotion of ammonia formation rate depends on the applied voltage and the hydrogen partial pressure in the cathode, whereas the contribution of charge-transfer reaction to ammonia cannot be improved by increasing current density or applied voltage.
3. The contribution of charge-transfer reaction to ammonia formation is very low (around 3×10^{-10} mol s^{-1} cm^{-2}).
4. The ammonia formation rate via the surface reaction with cathodic polarization can be improved significantly by increasing H_2 partial pressure in the cathode.
5. At high H_2 partial pressure, the ammonia formation rate is dominant by the surface reaction, whereas the main ammonia formation rate will change to the charge-transfer reaction at low H_2 partial pressure.

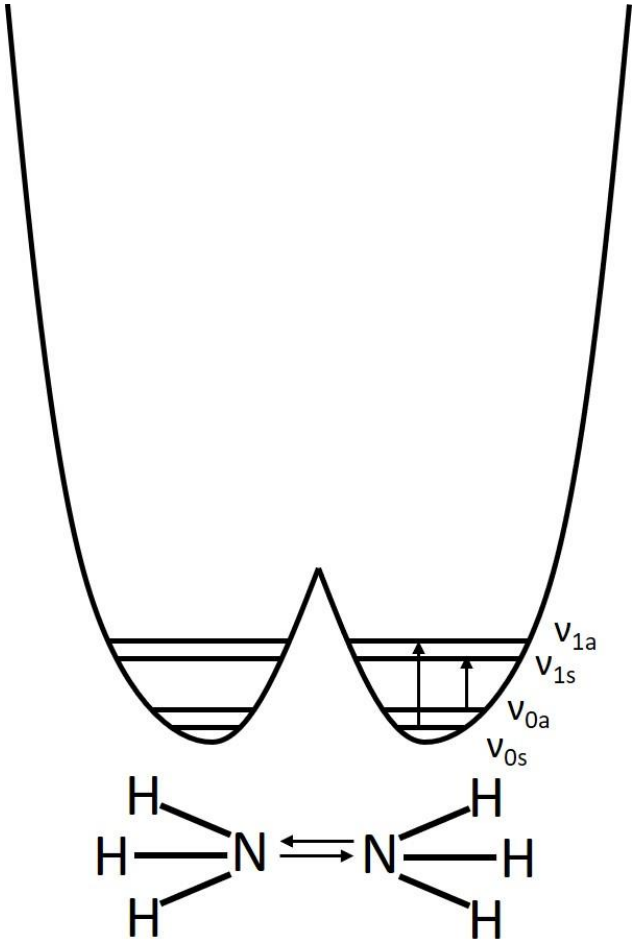

Fig. 5-1 Splitting of a degenerated energy for the ground state and the first excited state of rotational-vibrational energy level.

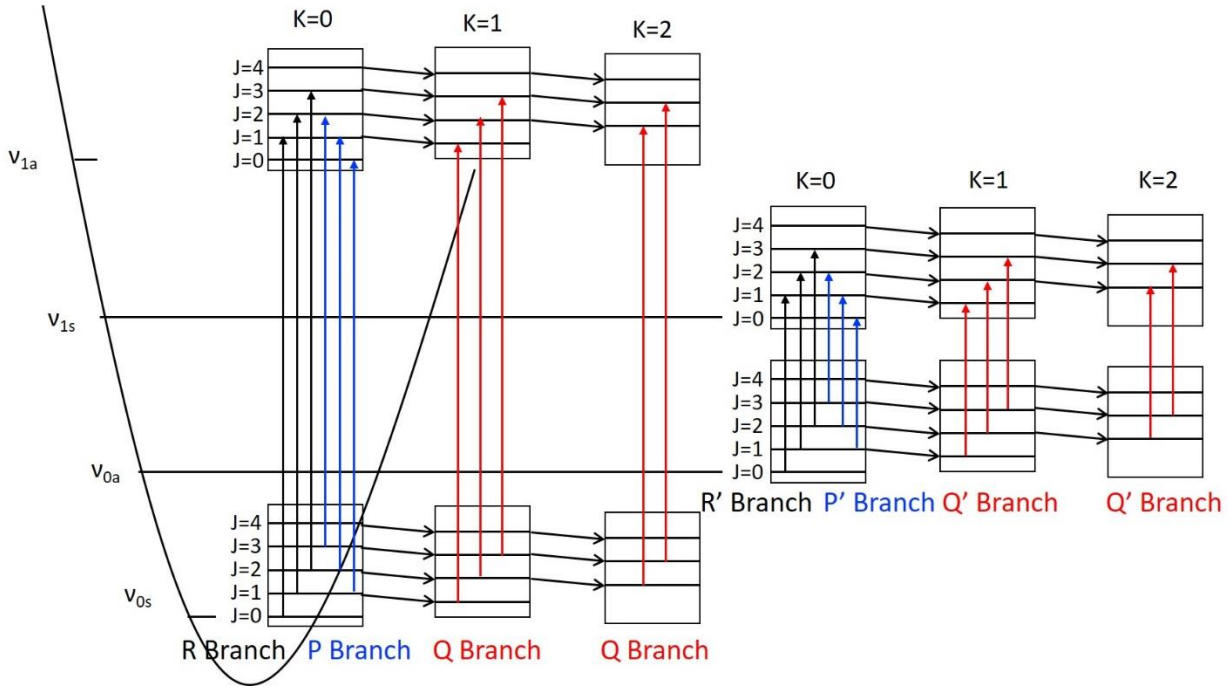

Fig. 5-2 Transition of P, Q, and R branches for the ν_2 vibration. Q and Q' represented the transition from symmetric state to asymmetric state and asymmetric state to symmetric state, respectively, as J = 0. P and P' represented the transition from symmetric state to asymmetric state and asymmetric state to symmetric state, respectively, as J = -1. R and R' represented the transition from symmetric state to asymmetric state and asymmetric state to symmetric state, respectively, as J = 1.

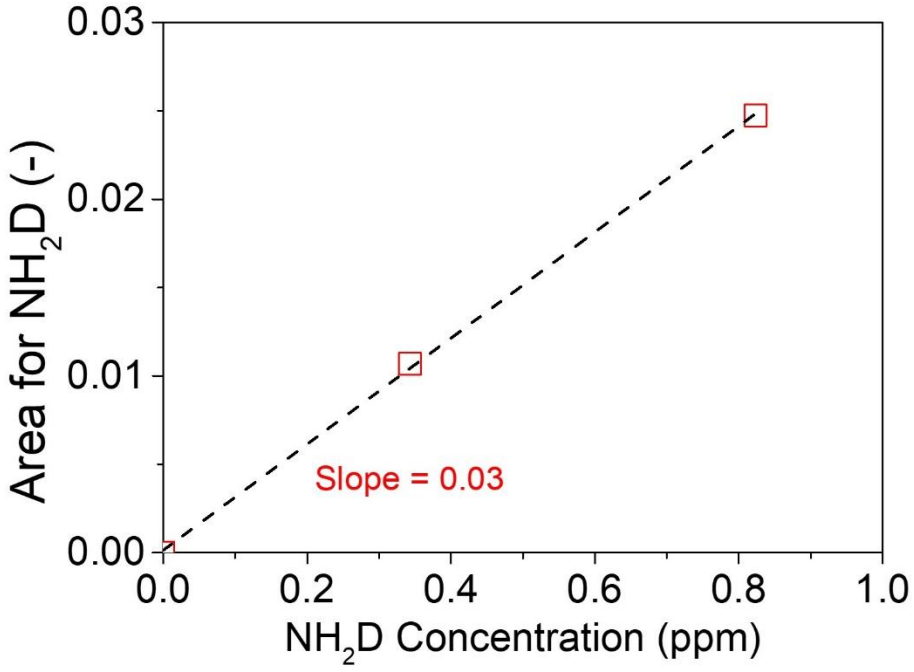

Fig. 5-3 The area of NHD_2 corresponds to the concentration of NHD_2. The slope is $\alpha_{NH2D} \times L$.

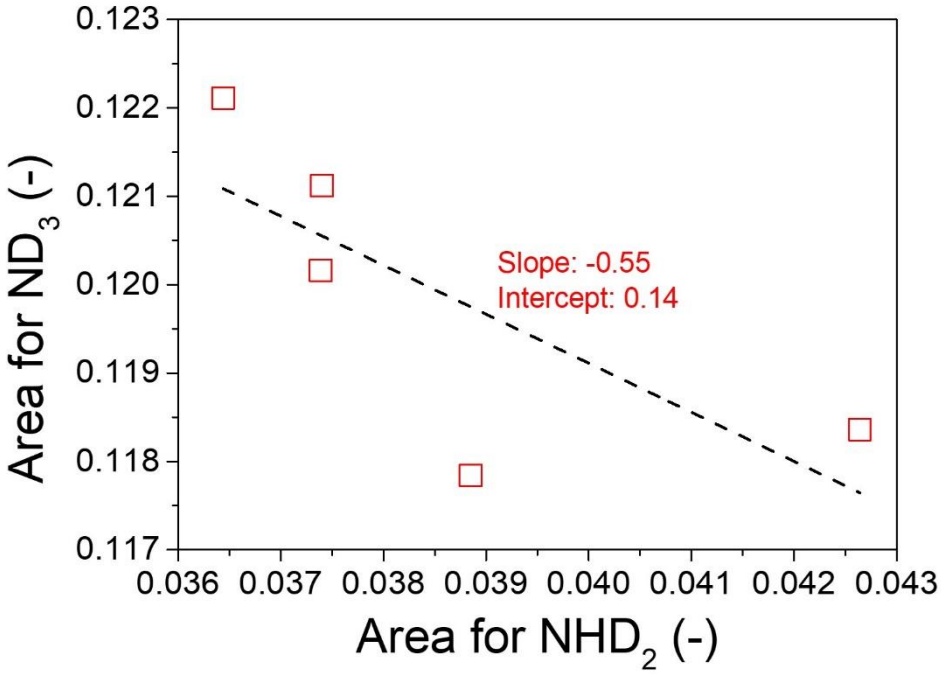

Fig. 5-4 The area of NHD_2 vs. the area of ND_3 at steady state. The intercept is $(C_{total}\text{-}C_{NH3}\text{-}C_{NH2D}) \times L \times \alpha_{ND3}$, and the slope is $-\alpha_{ND3}/\alpha_{NHD2}$.

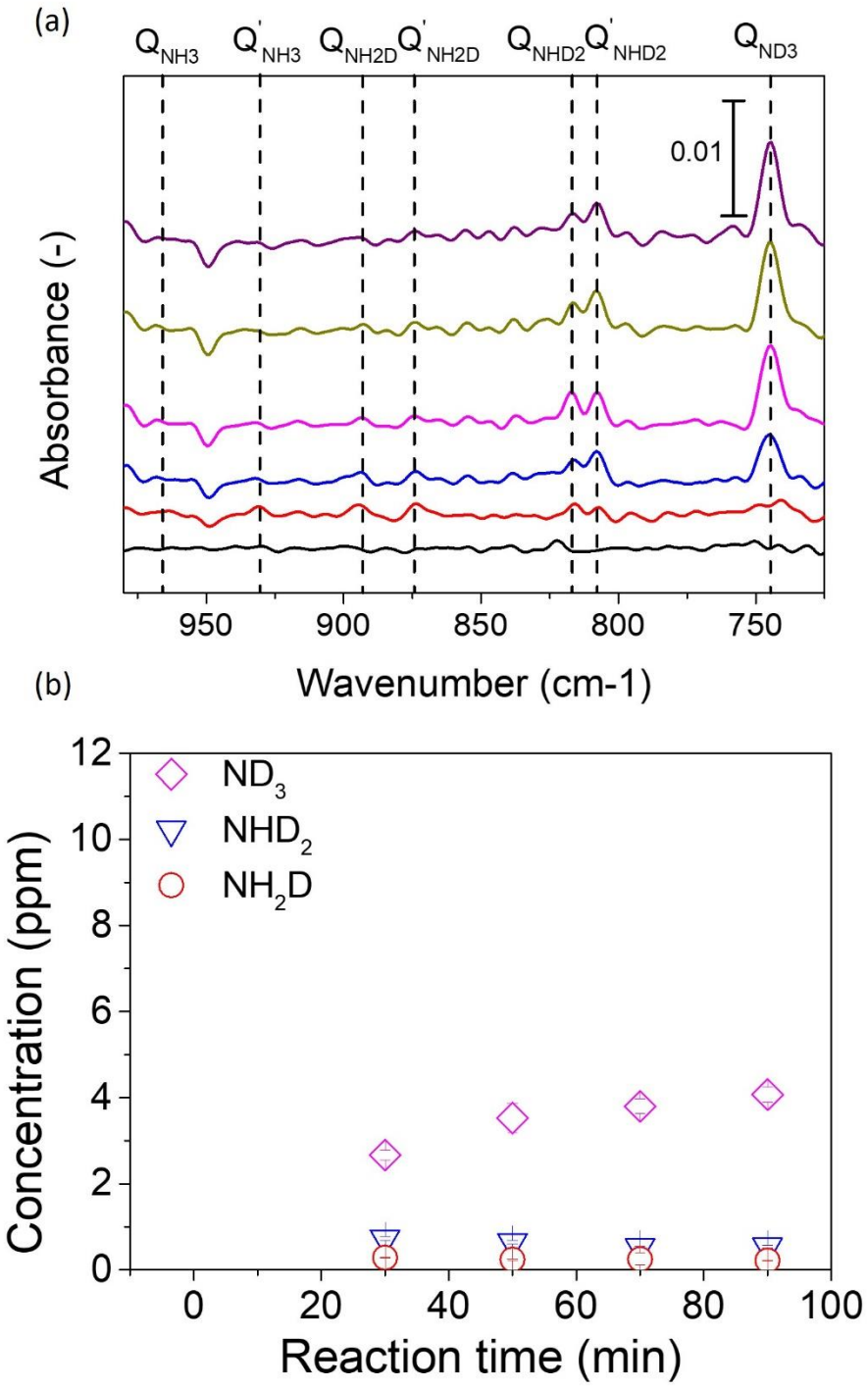

Fig. 5-5 (a) FTIR spectra changes with reaction time, and (b) is the concentrations of the ND_xH_{3-x} using porous pure Fe in 5% D_2−45% Ar−50% N_2 at rest potential.

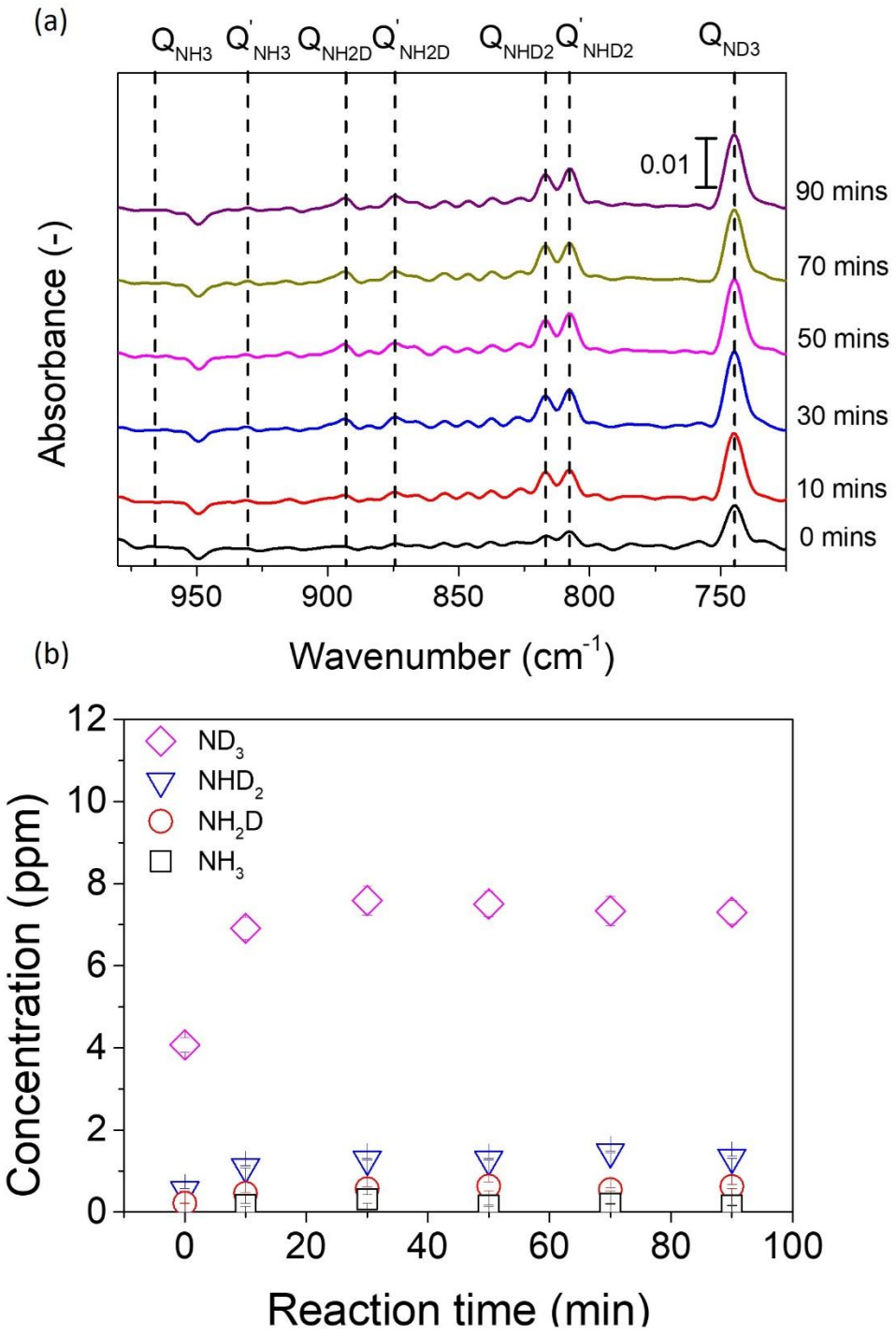

Fig. 5-6 (a) FTIR spectra changes with reaction time, and (b) was the concentrations of the ND_xH_{3-x} using porous pure Fe in 5% D_2−45% Ar−50% N_2 at −1V.

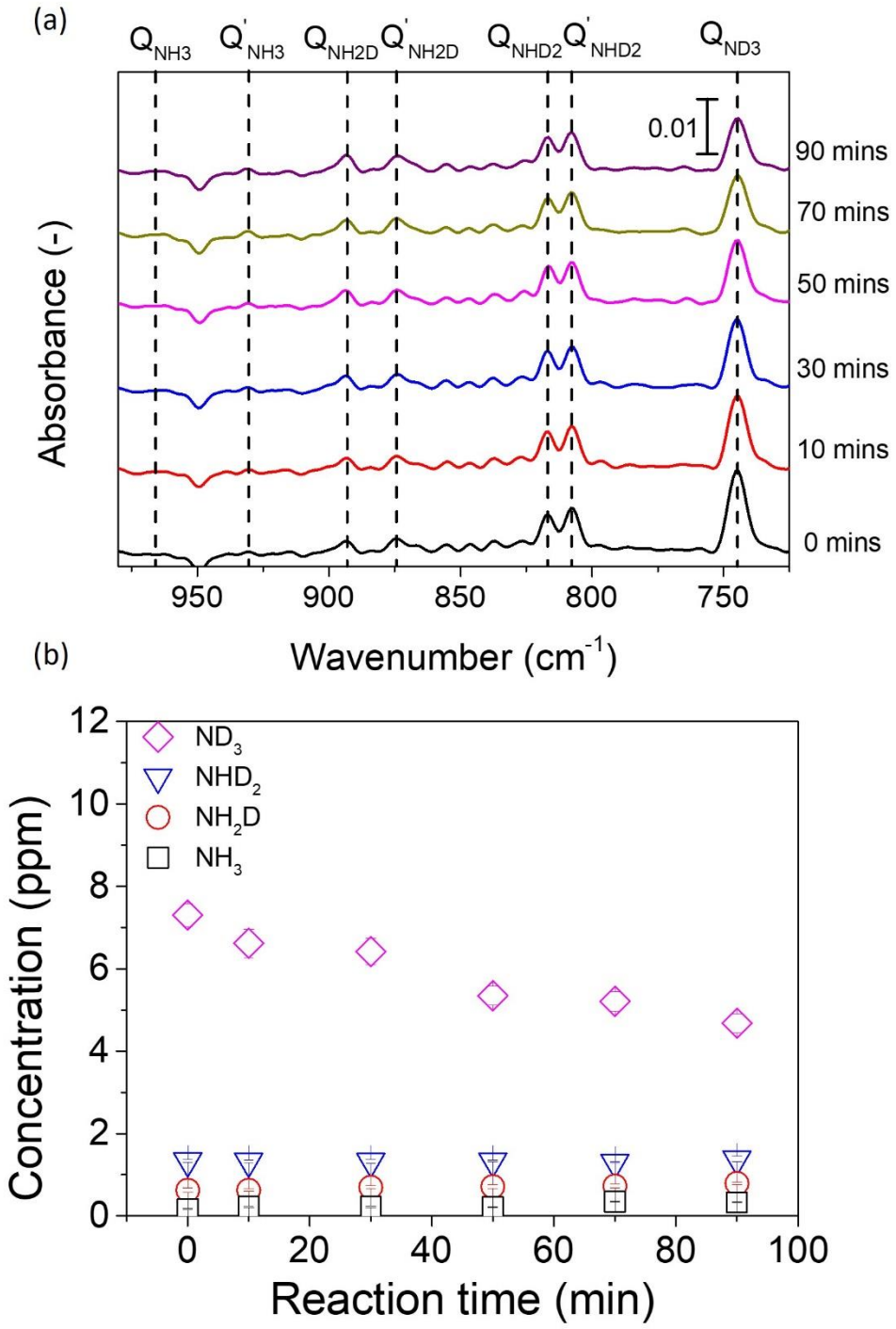

Fig. 5-7 (a) FTIR spectra changes with reaction time, and (b) is the concentrations of the ND_xH_{3-x} using porous pure Fe in 5% D_2−45% Ar−50% N_2 in the closed cell.

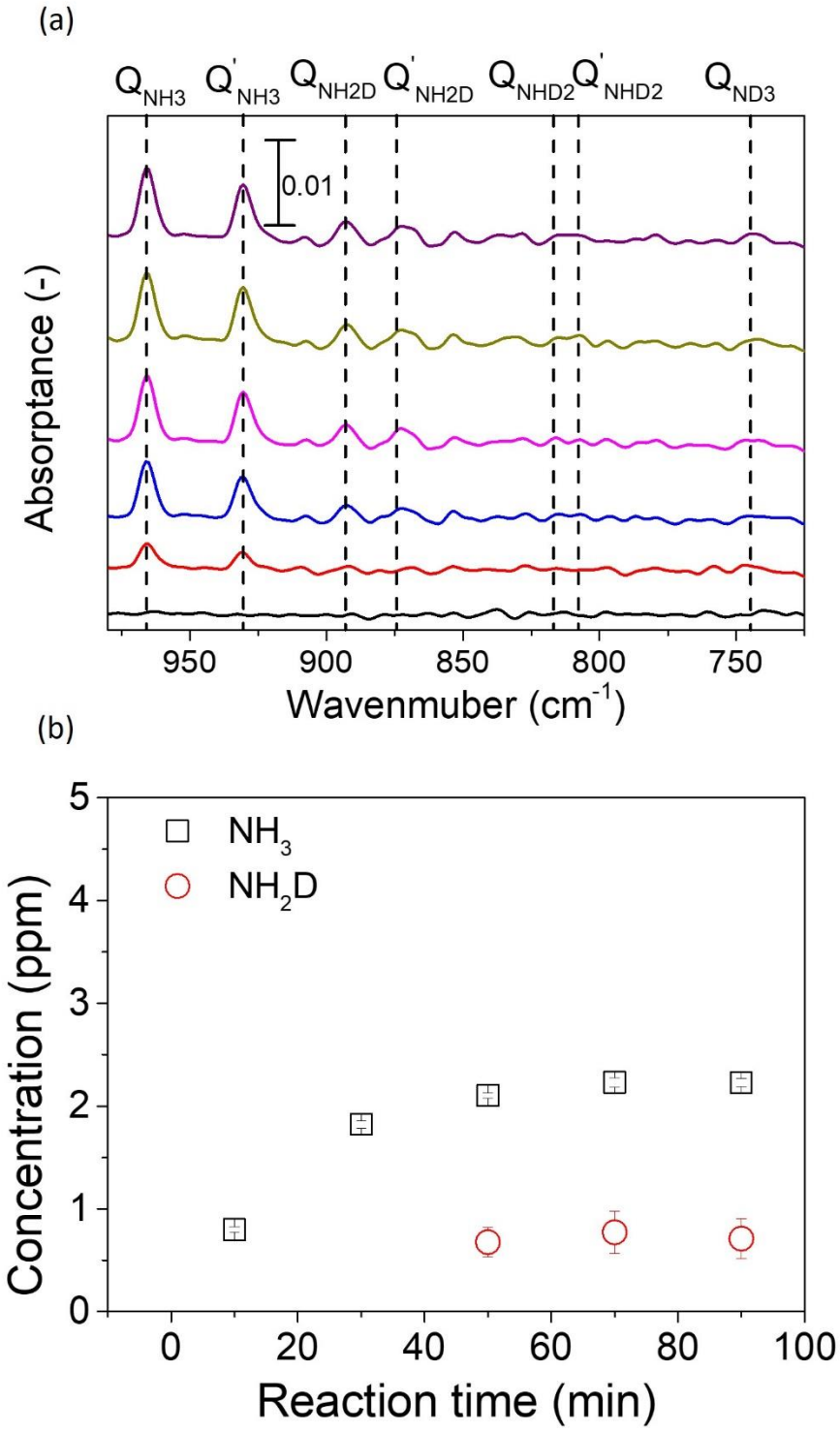

Fig. 5-8 (a) FTIR spectra changes with reaction time, and (b) is the concentrations of the ND_xH_{3-x} using porous pure Fe in 5% H_2−95% N_2 at rest potential.

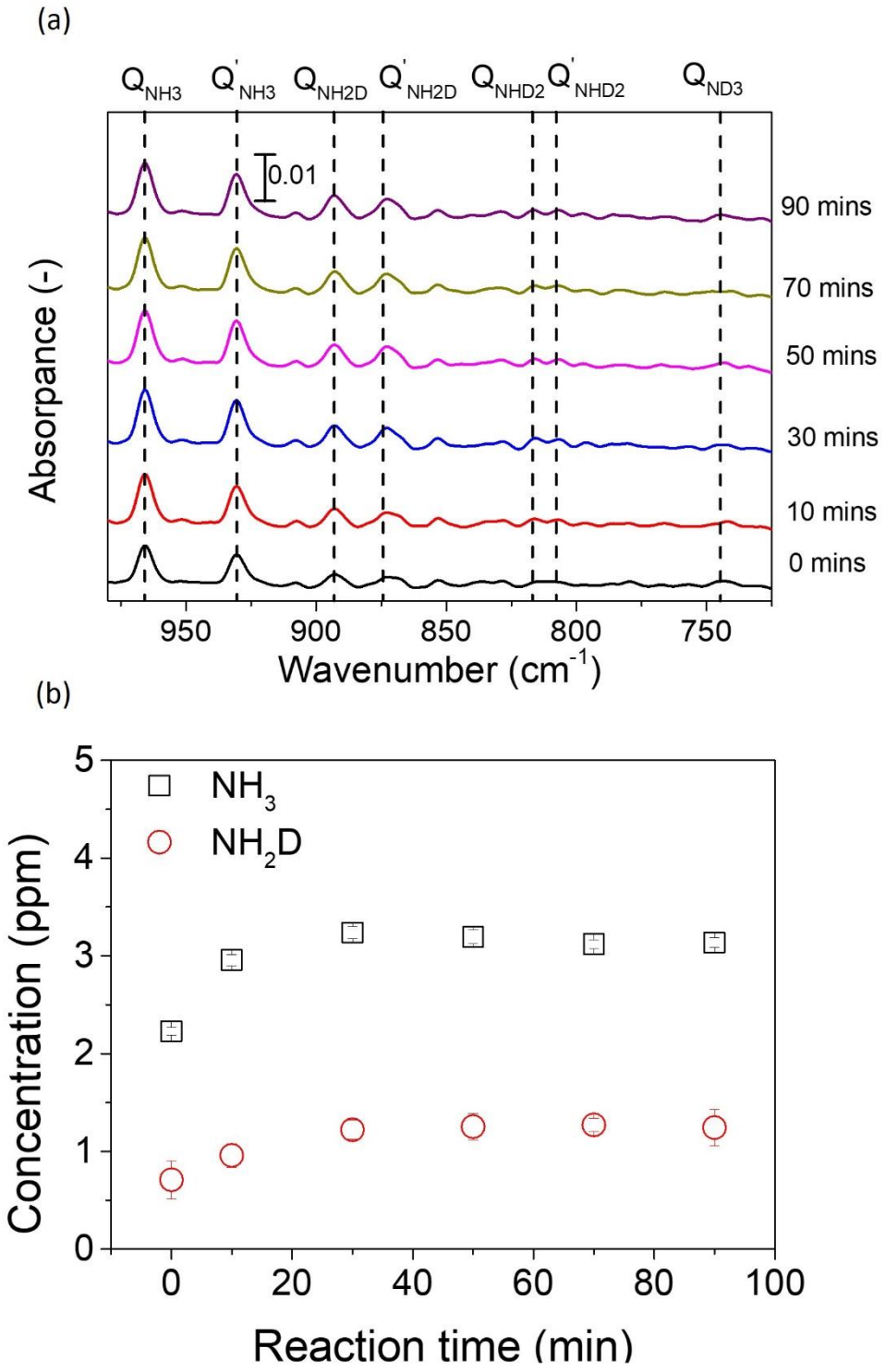

Fig. 5-9 (a) FTIR spectra changes with reaction time, and (b) is the concentrations of the ND_xH_{3-x} using porous pure Fe in 5% H_2−95% N_2 at −1V.

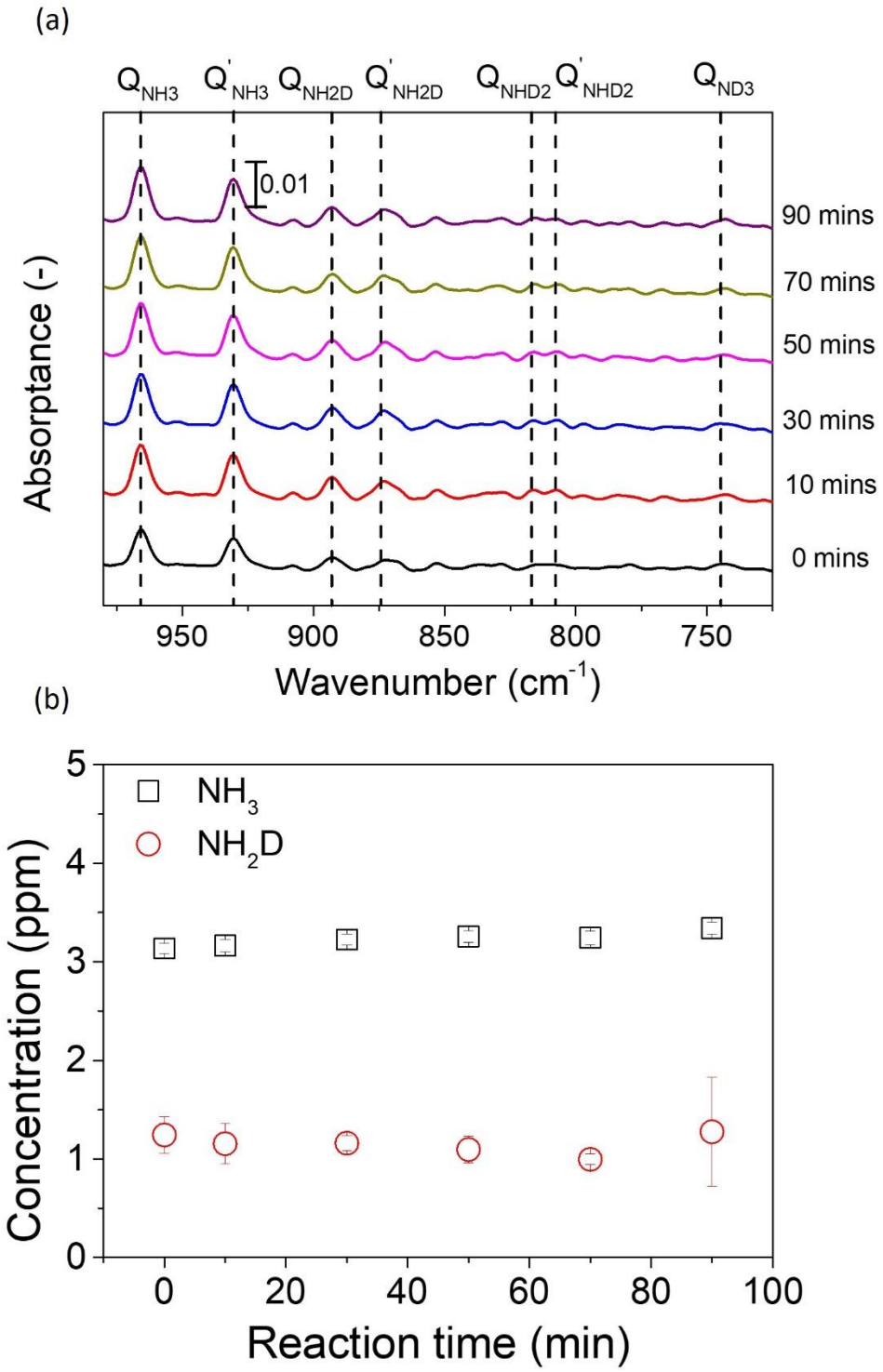

Fig. 5-10 (a) FTIR spectra changes with reaction time, and (b) is the concentrations of the ND_xH_{3-x} using porous pure Fe in 5% H_2–95% N_2 in the closed cell.

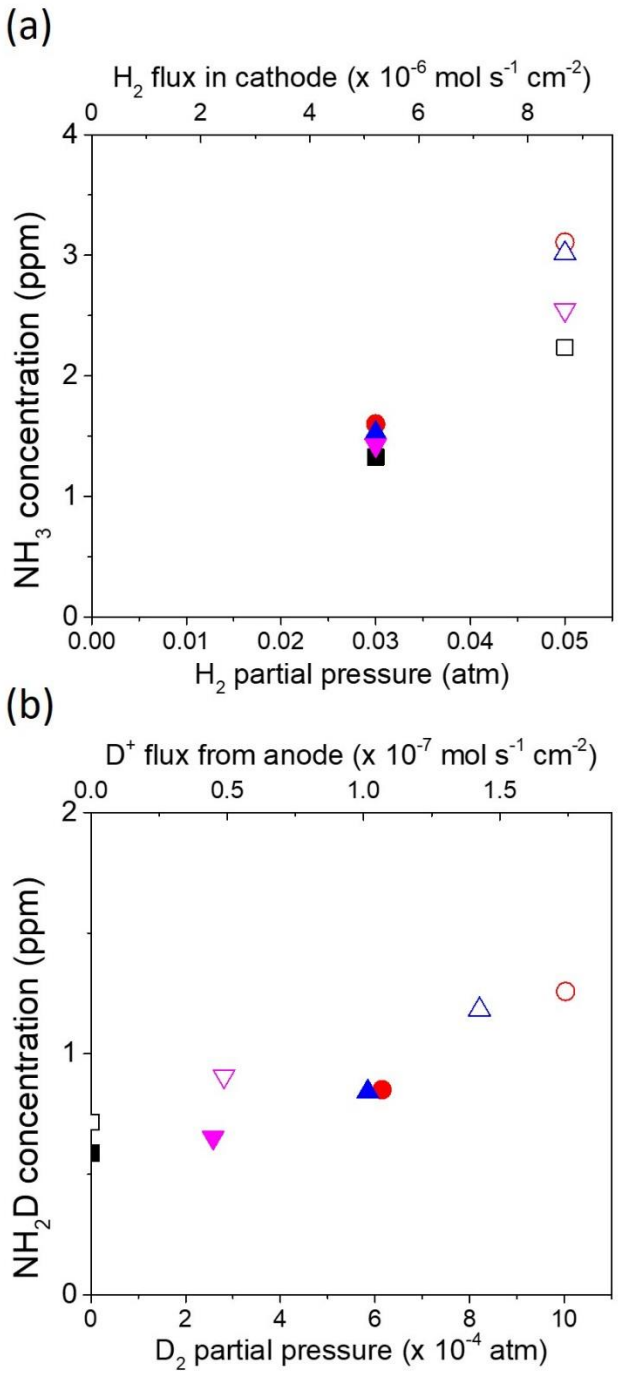

Fig. 5-11 (a) The concentration of NH_3 , and (b) the concentration of NH_2D are at rest potential, −0.3, −0.7, and −1 V in 5% H_2−95% N_2 and 3% H_2−97% N_2, respectively. □ 5% H_2−95% N_2 at the rest potential. ■ 3% H_2−97% N_2 at the rest potential. ○ 5% H_2−95% N_2 at −1V. ● 3% H_2−97% N_2 −1V. △ 5% H_2−95% N_2 at −0.7V. ▲ 3% H_2−97% N_2 at −0.7V. ▽ 5% H_2−95% N_2 at −0.3V. ▼ 3% H_2−97% N_2 at −0.3V.

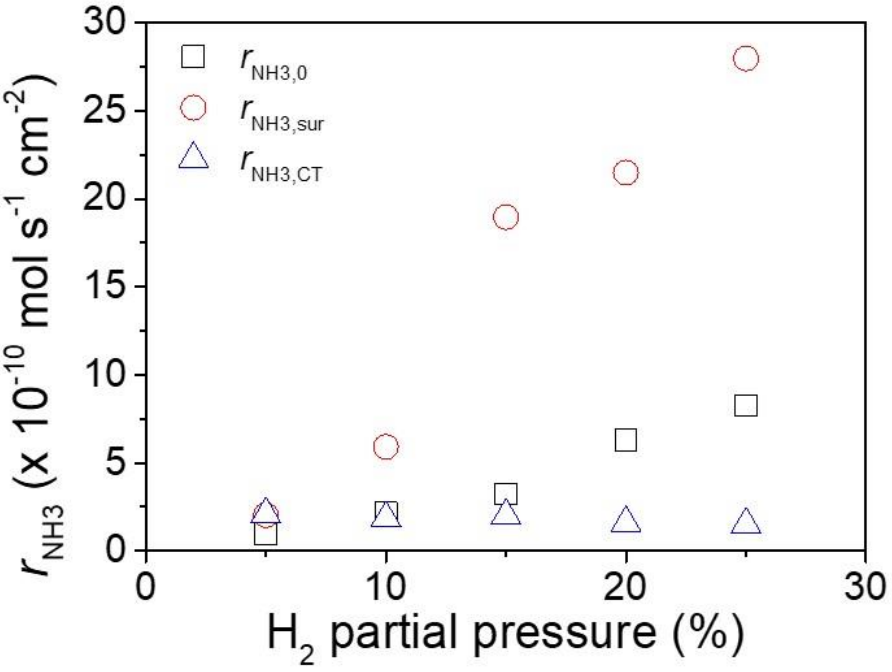

Fig. 5-12 Ammonia formation rate and concentrations at −1.3 V and different H_2 partial pressures.

6. Mechanism of the electrochemical reaction in ammonia synthesis

6.1. Introduction

In chapters 3–5, the mechanism of electrochemical promotion of ammonia formation via the surface reaction is confirmed. Furthermore, 10Fe−YSZ shows a pretty low ammonia formation rate with cathodic polarization, which indicates that the promotion of ammonia formation needs proton supply (Appendix J). The details were discussed in the next section. and then, a possible mechanism, EPOC, was proposed to explain the behavior of electrochemical ammonia formation by comparing the performances and reaction surface area for 10Fe−BCY and porous pure Fe cathodes.

6.2. Summary of result about electrochemical ammonia formation

In chapter 3, the effect of W addition into Fe–BCY cathode was examined. After W addition into Fe–BCY cathode, ammonia formation rate was slightly improved, and the current density decreased by 40%. This result indicates that the electrochemical promotion of ammonia formation rate is dependent on electrode potential rather than current density. Also, with a comparison with porous pure Fe and (W−)Fe−BCY cathodes, porous pure Fe cathode showed a better performance of ammonia formation with cathodic polarization, which indicates that ammonia is not formed by charge-transfer reaction at TPB. In chapter 4, the reaction orders of hydrogen and nitrogen at rest potential did not change after applying a negative voltage, which implies that the reaction mechanism with cathodic polarization is the same as that at the rest potential, i.e. surface reaction. Furthermore, the relationship between ammonia formation rate and H_2 partial pressure in the cathode was examined. Ammonia formation rate increased with increasing H_2 partial pressure in the cathode, which shows that the ammonia formation is not followed by charge-transfer reaction because the ammonia formation via charge-transfer reaction is independent of H_2 partial pressure. In chapter 5, the deuterium isotope analysis was used to examine the electrochemical reaction mechanism. The main product $NH_{3-x}D_x$ shows a high correlation to the species of H_2 (D_2) in the cathode with cathodic polarization, i.e., NH_3 (ND_3) is formed in H_2 (D_2) with cathodic polarization. This result shows that ammonia is formed via the surface reaction with cathodic polarization. In Appendix J, the ammonia formation rate was examined using a cell of Pt |YSZ| 10Fe−YSZ. No

promotion of ammonia formation rate was overserved with cathodic polarization, which indicates that the promotion of ammonia formation needs proton supply. Table 6-1 summarizes the results in chapters 3–5 and Appendix J. Based on these results, a possible reaction mechanism, electrochemical promotion of ammonia formation (EPOC), was proposed, which is discussed in the next section.

6.3. Electrochemical promotion of ammonia formation

6.3.1. Electrochemical promotion of catalyst effect

To investigate the electrochemical reaction, the conventional system of a solid electrode and a liquid electrolyte was considered. After applying a negative voltage, the formation of a double layer was observed at the interface.[111] Charge carriers were accumulated at the interface and caused a very strong electric field. A previous study pointed out that the value of double-layer capacitance was around 20 μF/cm^2.[112] On the other hand, for the system consisting of a solid electrode (pt) and a solid electrolyte (YSZ: O^{2-} conductor), previous studies proposed that there was an effective double layer formation on the metal surface and that the value of capacitance was around 200 μF/cm^2.[87, 113] This result implied that there is a strong electric field in the effective double layer. Also, the effective double layer can be formed using a Na^+ ion conductor, which represents that the effective double layer can also be formed using a cation conductor.[88, 114, 115] The effective double layer can induce an effect of EPOC to promote the reaction rates.[88, 115] Based on the conclusions of previous studies, the results in chapters 3–5, and Appendix J, the electrochemical ammonia formation is probably via the surface reaction with EPOC. Vayenas et al. proposed an EPOC effect model to explain an increase in reaction rate.[86-88] The work function of metal catalyst can be altered by the effective double layer, which is formed via spillover of mobile ions origination from charge carriers in the electrolyte, on the metal surface with cathodic/anodic polarization. The changed work function can promote the electron donation/backdonation reaction study, which can be described by Eq. 6-1:

$$\ln\left(\frac{r_{\mathrm{NH3}}}{r_{\mathrm{NH3,0}}}\right) = \alpha_{\mathrm{N}}\frac{\Delta\Phi}{k_{\mathrm{b}}T} \qquad 6\text{-}1$$

where $r_{\mathrm{NH3,0}}$, α_{N}, $\Delta\Phi$, and k_{b} are the ammonia formation rate at rest potential, reaction constant, overpotential-induced change in the Fe work function, and Boltzmann's constant, respectively.

In this study, the ammonia formation rate was improved using Fe catalyst with cathodic polarization. Therefore, the effective double layer formed via H+ spillover on the Fe surface decreases the work function of Fe to promote the electron backdonation, which is induced by electron transfer from the Fe Fermi level to the N_2 antibonding orbital of π_{2p}*, in Fig. 6-1. This hypothesis supports the result that a low ammonia formation rate using 10Fe−YSZ cathode because it cannot form the effective double layer on the Fe surface (Appendix J). Therefore, the effective double layer on Fe catalyst plays an important role in the electrochemical promotion of ammonia synthesis. To estimate the area of effective double layer, the performance and cathode structure for 10Fe−BCY and porous pure Fe cathodes are discussed in the next section.

6.4. Estimation of surface area and triple phase boundary length

For estimation of the area of effective double layer in 10Fe–BCY and porous pure Fe cathodes, the following parameters were stated below:

l_i (i= Fe–BCY or Fe): TPB length.

$l_{eff,i}$ (i = Fe–BCY or Fe): effective TPB length, which is determined by Fe particles connected with a network structure of electrons.

A_i (i = Fe–BCY or Fe): physical surface area, i.e. total surface area, of Fe particles.

S_i (i = Fe–BCY or Fe): effective surface area of Fe particles, i.e. Fe particles connected with a network structure of electrons, as shown in Fig. 6-2.

$S^*_{eff,i}$ (i = Fe–BCY or Fe): the area of effective double layer, which was covered by protons on $S_{Fe\text{-}BCY}$ or S_{Fe}, for promoting N_2 dissociation and subsequent ammonia formation, as shown in Fig. 6-3.

6.4.1. Estimation of TPB length and Fe surface area in 10Fe–BCY

To estimate the Fe surface area and TPB length in 10Fe–BCY, the semicircular shape of Fe particles formed on the BCY surface was assumed, as shown in Fig. 6-4. Therefore, the physical surface area, $A_{Fe–BCY}$, and the total triple phase boundary length, $l_{Fe\text{-}BCY}$, can be estimated by Eqs. 6-2 and 6-3.

$$A_{\mathrm{Fe-BCY}} = \frac{m_{\mathrm{Fe-BCY}}}{\frac{\frac{4\pi}{3}(\frac{D_{\mathrm{Fe-BCY}}}{2})^3}{2} d} \frac{4\pi(\frac{D_{\mathrm{Fe-BCY}}}{2})^2}{2} \quad 6\text{-}2$$

$$l_{\mathrm{Fe-BCY}} = \frac{M_{\mathrm{Fe-BCY}}}{\frac{\frac{4\pi}{3}(\frac{D_{\mathrm{Fe-BCY}}}{2})^3}{2} d} \pi D_{A'} \quad 6\text{-}3$$

where $m_{\mathrm{Fe\text{-}BCY}}$, $D_{\mathrm{Fe\text{-}BCY}}$, and d are Fe weight in the cathode, Fe particle average diameter, and Fe density (7.874 g^{-1} cm^{-3}). The average diameter of Fe particles is calculated by the FE−SEM image of Fe particles in 10Fe−BCY cathode after the electrochemical measurement. The size distribution is shown in Fig. 6-5. The resultant values in 10Fe–BCY cathode are summarized in Fig. 6-6 and Table 6-2.

6.4.2. Estimation of Fe surface area and TPB length in porous pure Fe

The physical surface area, A_{Fe}, was estimated by the BET measurement, as shown in Fig. 6-7. The observed specific surface area (S_t) of Fe particles in type B was 0.71 m^2/g, which is obtained by Eq. 6-4.

$$S_t = \frac{\frac{1}{m_{BET} + I_{BET}} N_{\mathrm{A}} \sigma}{M} \quad 6\text{-}4$$

where m_{BET}, I_{BET}, N_{A}, σ, and M are the slope and intercept in the BET measurement, Avogadro's number, the adsorption cross section of the adsorbing species, and the molecule weight of the adsorbate gas.

The weight of porous pure Fe cathode is 0.7 mg, and the resultant value of A_{Fe} is 5.0 cm^2. To estimate TPB length in porous pure Fe, l_{Fe}, the average Fe particle size is determined by the FE−SEM image of Fe particles in porous pure Fe after the electrochemical measurement. The Fe size distribution is shown in Fig. 6-8. Then, to simplify the estimation of l_{Fe}, that Fe particles accumulate to form a columnar structure was assumed, as shown in Fig. 6-9. Therefore, the porosity of the cathode is the same as the coverage of Fe particles on the BCY electrolyte. The TPB length is the total interfacial circumference of the Fe column and BCY electrolyte, which is calculated by Eq. 6-5.

$$l_{Fe} = \frac{A_{ele}\,(1-\varphi)}{\pi {D_{\mathrm{Fe}}}^2}\pi D_{Fe} \qquad 6\text{-}5$$

where φ, D_{Fe}, and A_{ele} are porosity, Fe particle average diameter in porous pure Fe, and the area of the electrode, which is a semi-circle with 10 mm diameter, as shown in Fig. 2-1.

$$A_{\mathrm{ele}} = \frac{\pi\,(\frac{D_{ele}}{2})^2}{2} \qquad 6\text{-}6$$

where D_{ele} is the diameter of electrode (10 mm).

The TPB length is summarized in Fig. 6-10. The resultant values are summarized in Table 6-3.

6.5. Estimation of the area of effective double layer and proton diffusion length

In chapter 3, the ammonia formation rate for porous pure Fe is higher than that for 10Fe−BCY. However, porous pure Fe cathode has a smaller physical surface area for Fe particles than 10Fe−BCY (see Table 6-2−Table 6-3). This situation is probably caused by two possibilities: 1) the ammonia formation cannot be promoted via isolated Fe particles that do not connect with the network structure of electrons in 10Fe−BCY cathode with cathodic polarization (Fig. 6-2). 2) the active hydrogen evolution reaction hinders the nitrogen reduction reaction at the TPB region because the active sites occupied by H adatoms are not available to N_2 adsorption and dissociation (Fig. 6-11).

6.5.1. First possibility: isolated Fe particles in 10Fe-BCY

The current density in 10Fe–BCY is 1.6 times higher than that in pure porous Fe cathode at 600°C (Fig. 3-9a and Fig. 3-12b), whereas the TPB length in 10Fe−BCY cathode is 243 times longer than that in porous pure Fe cathode. Supposing that the current density is proportional to the effective TPB length, l_{eff}, this discrepancy is probably caused by that a part of the Fe particles on BCY surface do not connect with a network structure of electrons in 10Fe−BCY cathode, as shown in Fig. 6-2. Therefore, the physical surface area, $A_{\mathrm{Fe–BCY}}$, is not equal to the effective surface area, $S_{\mathrm{Fe–BCY,}}$ ($A_{\mathrm{Fe–BCY}} \neq S_{\mathrm{Fe–BCY}}$), and the TPB length, $l_{\mathrm{Fe–BCY}}$, is not equal to the effective TPB length, $l_{\mathrm{eff,\ Fe–BCY}}$, as well ($l_{\mathrm{Fe–BCY}} \neq l_{\mathrm{eff,\ Fe–BCY}}$). For porous pure Fe, all Fe particles connecting with a network structure of electrons is assumed. Therefore, the physical surface area is the same as the effective physical surface area ($A_{\mathrm{Fe}} = S_{\mathrm{Fe}}$), and the triple TPB length is the same as the effective TPB length in porous pure Fe ($l_{\mathrm{Fe}} = l_{\mathrm{eff,Fe}}$). Combined with the condition of effective TPB length

and current density, $l_{\text{eff, Fe–BCY}}$ can be obtained by Eq. 6-*7*, assuming that the current density is proportional to the effective TPB length. Then, $S_{\text{Fe–BCY}}$ can be obtained by Eq. 6-*8*.

$$\frac{i_{\text{Fe–BCY}}}{i_B} = \frac{l_{eff,\text{Fe–BCY}}}{l_{eff,B}} \quad \text{6-7}$$

$$\frac{l_{\text{Fe–BCY}}}{A_{\text{Fe–BCY}}} = \frac{l_{eff,\text{Fe–BCY}}}{S_{\text{Fe–BCY}}} \quad \text{6-8}$$

where $i_{\text{Fe-BCY}}$ and i_{Fe}, are the current densities at 600°C using 10Fe−BCY and porous pure Fe cathodes, respectively. The effective TPB length $l_{\text{eff, Fe–BCY}}$ and the effective surface area of Fe particles $S_{\text{Fe–BCY}}$ were 6.2×10^4 cm and 0.13 cm^2 in 10Fe−BCY, respectively.

S_{Fe} (5 cm^2) was 38 times larger than $S_{\text{Fe–BCY}}$ (0.13 cm^2), whereas the ammonia formation rate in porous pure Fe was 2.1 times than that in 10Fe−BCY. The discrepancy is probably caused by that the effective surface area is not equal to the effective double layer, S^*_{eff}. Thus, a rough estimation of the effective double layer, S^*_{eff}, was conducted by combining the ammonia formation rate and the effective surface area in of 10Fe–BCY and porous pure Fe cathodes. Also, a new parameter of proton diffusion length, *h*, which is the diffusion length of spillover proton in electrode, was introduced for the estimation.

To calculate the proton diffusion length and the area of the effective double layer, three assumptions are proposed. #1. Proton diffusion length on Fe surface is adequately long. Therefore, protons can cover all Fe surface in 10Fe−BCY because the Fe particles grow on the BCY particles and the diameter of Fe particles is around 40 nm, as shown in Fig. 6-12a. Thus, the effective surface area is the same as the area of effective double layer in 10Fe−BCY cathode $S^*_{\text{eff,Fe–BCY}} = S_{\text{Fe–BCY}}$. #2. Because the electrode thickness is 12.5 μm in porous pure Fe cathode, the proton diffusion length, *h*, should be less than or equal to the thickness of porous pure Fe cathode, *H*. Therefore, the proton diffusion length could be described by Eq. 6-9:

$$h = H\tau \quad \text{6-9}$$

where τ is a constant between 0 and 1. Therefore, the area of effective double layer can be described by Eq. 6-10. And the effective double layer is formed in a part of the porous pure Fe cathode via proton diffusion, as shown in Fig. 6-12b.

$$S^*_{\text{eff,Fe}} = S_{\text{Fe}}\tau \quad \text{6-10}$$

#3. Because the same catalyst (Fe) and gas were used in the electrochemical reaction for both the cathodes, the reaction rate constants for them were the same. Therefore, the relationship between the ammonia formation rate and the area of the effective double layer can be simplified as Eq. 6-11:

$$\left(\frac{r_{\mathrm{NH3,Fe-BCY}}}{r_{\mathrm{NH3,Fe}}}\right) = \frac{\left(S^{*}_{\mathrm{eff,Fe-BCY}}\right)}{\left(S^{*}_{\mathrm{eff,Fe}}\right)} = \frac{\left(S_{\mathrm{Fe-BCY}}\right)}{\left(S_{\mathrm{Fe}}\tau\right)} \qquad 6\text{-}11$$

where $r_{\mathrm{NH3,Fe\text{-}BCY}}$ and $r_{\mathrm{NH3,Fe}}$, are the ammonia formation rates.

Based on our order-of-magnitude calculation, the value of τ was around 0.08 when the average diameter of Fe particles in both the cathodes was used. The relevant values are summarized in Table 6-4. Therefore, the proton diffusion length was about 1 μm. Fig. 6-13 shows that the relationship between the effective proton diffusion length and the diameter of Fe particles in 10Fe-BCY and porous pure Fe. If the standard deviation of the Fe particles diameter is considered, the proton diffusion length is between sub-micrometer to several micrometers in porous pure Fe. Therefore, the effective double layer can be formed in a part of the Fe electrode (sub-micrometer to several micrometers distance from BCY electrolyte).

6.5.2. The second possibility: TPB suppression ammonia formation

Another possibility is that the active H_2 evolution reaction at TPB prevented N_2 dissociation (Fig. 6-11). This phenomenon of hydrogen poisoning is also reported by Kosaka et al. using Ru doped BCY cathode catalyst in the electrochemical reaction.[75] To estimate the reaction area for NH_3 formation, the area of effective double layer should subtract the area of TPB region for hydrogen evolution reaction, which is described by Eq. 6-12.

$$r_{NH3} \propto \left(A_{\mathrm{EDL}} - l_{\mathrm{TPB}} w_{\mathrm{TPB}}\right) \qquad 6\text{-}12$$

where A_{EDL}, l_{TPB} and w_{TPB} were the area of effective double layer, the length, and the width of TPB. Because the electrochemical reaction of ammonia formation in 10Fe−BCY and porous pure Fe is operated using Fe-based catalysts and at the same H_2 and N_2 partial pressure, Eq. 6-12 could be simplified to Eq. 6-13. Here, assumptions #1−#3 in the first possibility were used as well. Therefore, the Eq. 6-13 can be described by Eq. 6-14.

$$\left(\frac{r_{\mathrm{NH3,Fe-BCY}}}{r_{\mathrm{NH3,Fe}}}\right) = \frac{\left(S^{*}_{\mathrm{eff,Fe-BCY}}\right)}{\left(S^{*}_{\mathrm{eff,Fe}}\right)} \qquad 6\text{-}13$$

$$\frac{\left(S^{*}_{\mathrm{eff,Fe-BCY}}\right)}{\left(S^{*}_{\mathrm{eff,Fe}}\right)} = \frac{\left(S_{\mathrm{Fe-BCY}} - l_{\mathrm{TPB,Fe-BCY}} w_{\mathrm{TPB}}\right)}{\left(S_{\mathrm{Fe}}\tau - l_{\mathrm{TPB,Fe}} w_{\mathrm{TPB}}\right)} \quad \text{6-14}$$

where w_{TPB} was the width of TPB. Because the value of the width of TPB is unclear, according to the previous studies, the width of TPB changed with overpotential. Here, the width is assumed as 20 nm, and the value of τ is 0.4, which indicated that the effective proton diffusion length is around 5 μm in type B. Therefore, the protons from electrolyte can migrate for several micrometers to form the effective double layer for improving ammonia formation in porous pure Fe cathode. This result indicated that the thickness of electrode should be decreased because the Fe surface without effective double layer prevents ammonia from escaping out of the electrode, and that makes ammonia reverse into H_2 and N_2.

6.6. **Conclusion**

1. Protons diffusing from electrolyte can migrate sub-micrometer to several micrometers to form an effective double layer, which can promote the reaction for ammonia formation.
2. The electrode thickness is too thick in the porous pure Fe cathode because the Fe surface without effective double layer formation prevents the ammonia from escaping out of the electrode, and that makes ammonia reverse into H_2 and N_2.

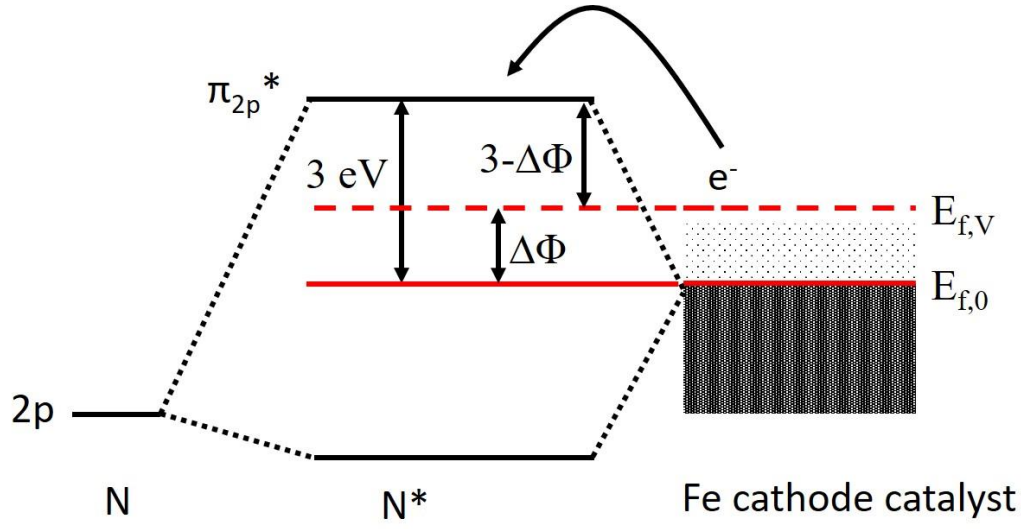

Fig. 6-1 Energy diagram about N–N bonding is weakened by increasing the metal Fermi level as applied a negative voltage.

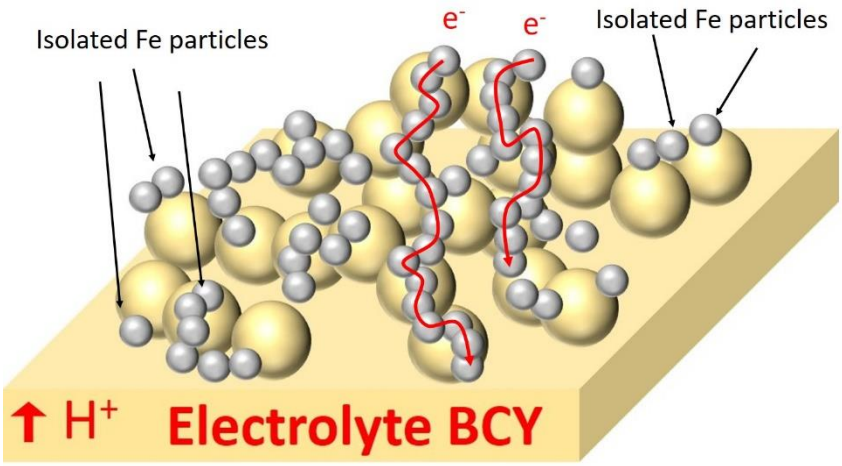

Fig. 6-2 A schematic image of Fe particles on BCY particles connected with a network structure of electron and isolated Fe particles on BCY particles in 10Fe−BCY cathode.

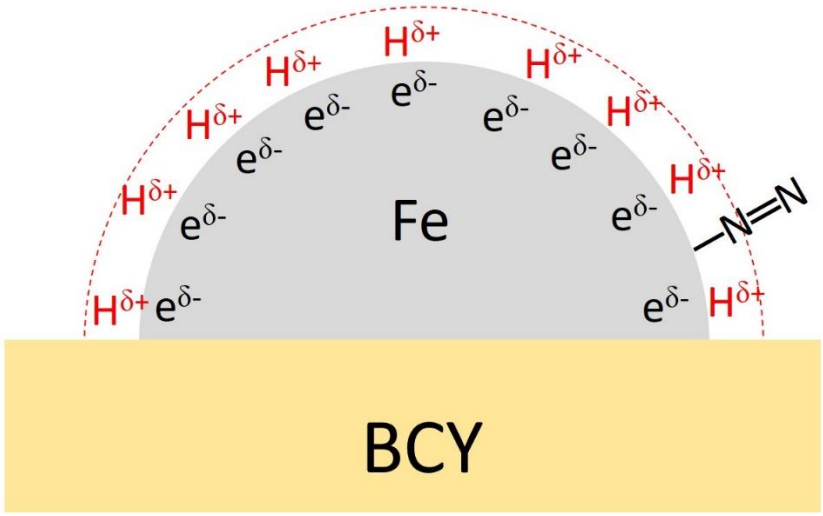

Fig. 6-3 A schematic image of effective double layer on Fe surface.

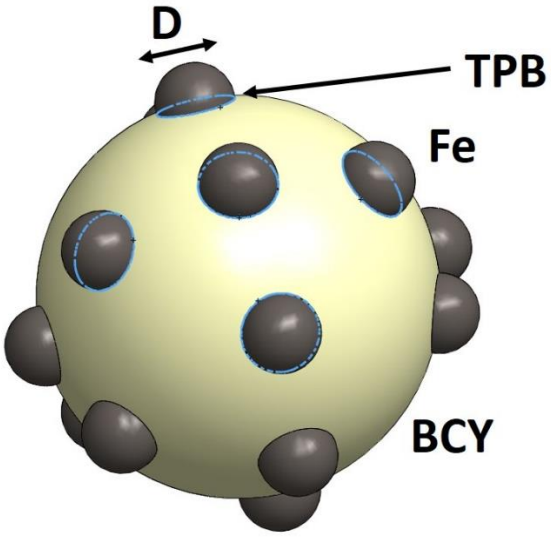

Fig. 6-4 A schematic image of 10Fe–BCY structure. Fe particle is semi-circle shape on BCY surface.

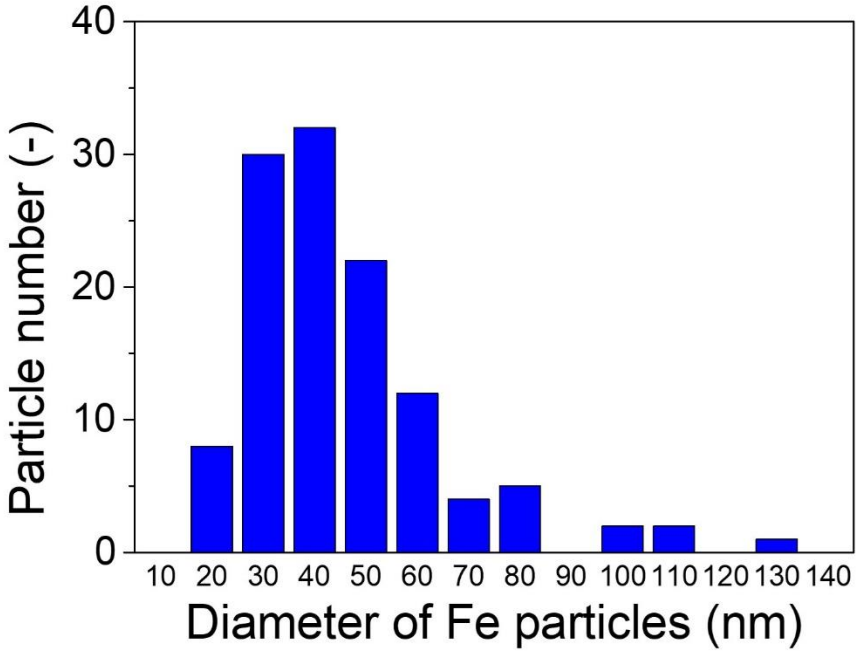

Fig. 6-5 Distribution of Fe particle diameter in 10Fe−BCY cathode.

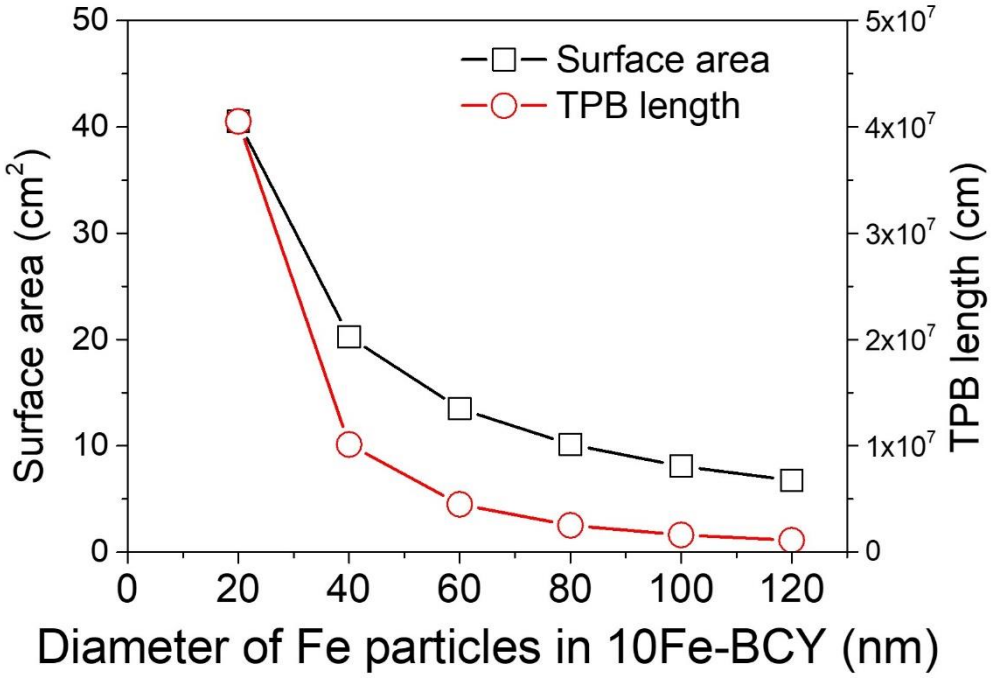

Fig. 6-6 Relationship among TPB length, surface area, and Fe particle diameter in 10Fe−BCY.

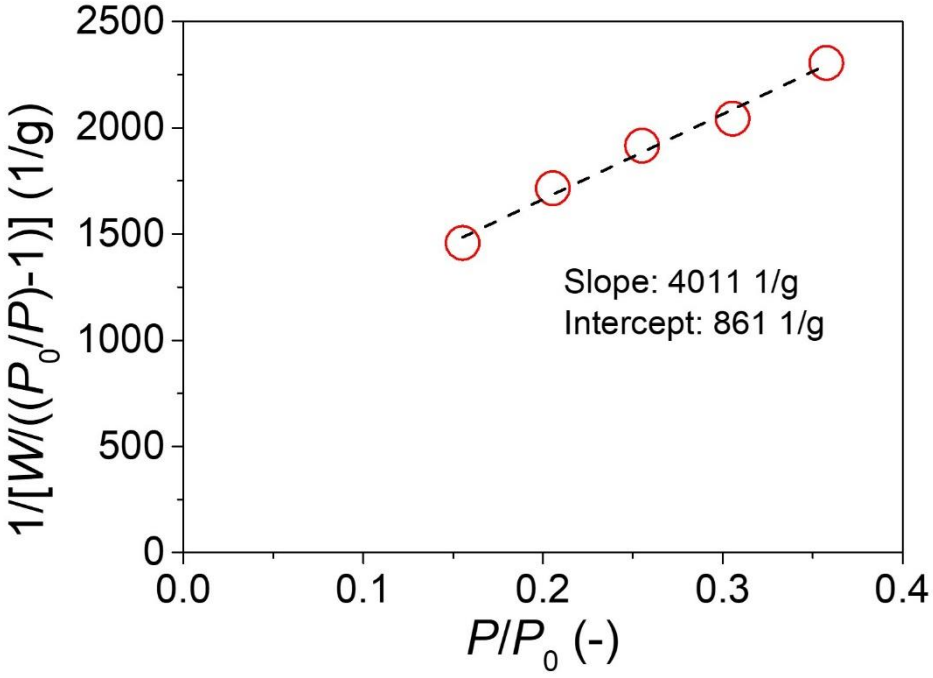

Fig. 6-7 BET measurement for porous pure Fe cathode.

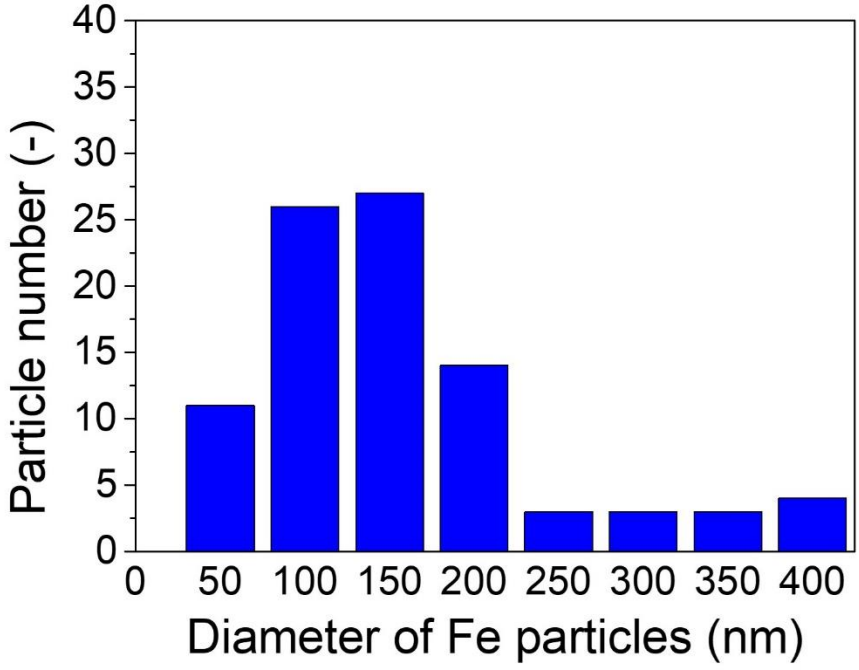

Fig. 6-8 The distribution of Fe particle diameter in porous pure Fe.

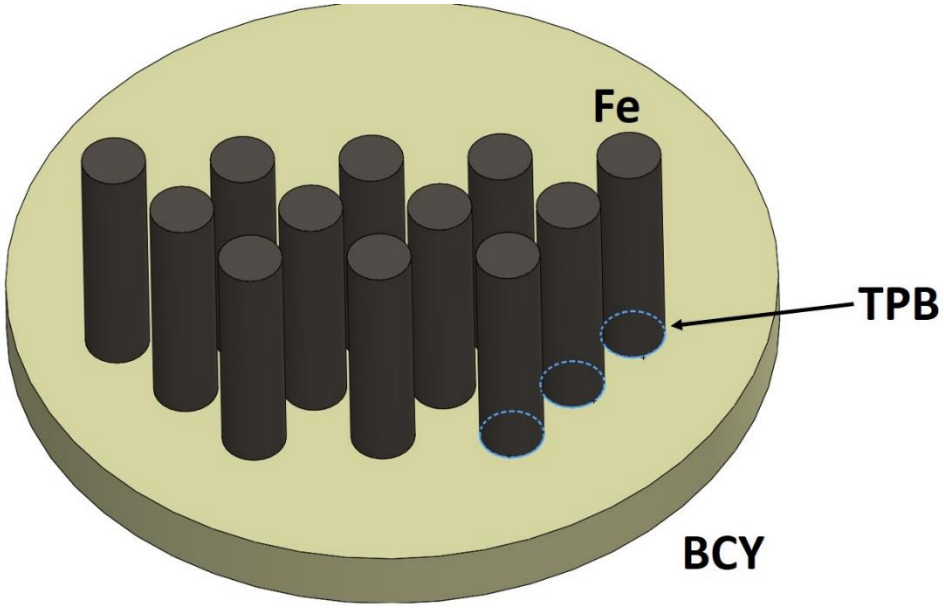

Fig. 6-9 A schematic image of column structure in porous pure Fe cathode.

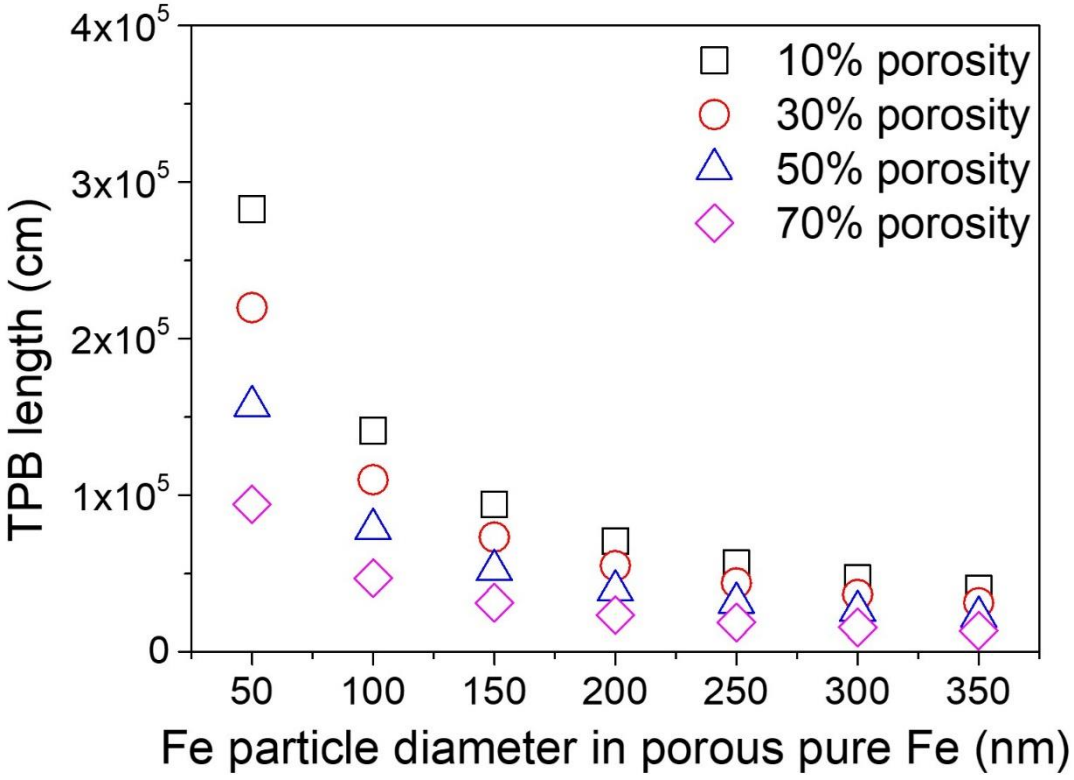

Fig. 6-10 Relationship between TPB length and Fe particle diameter in porous pure Fe cathode.

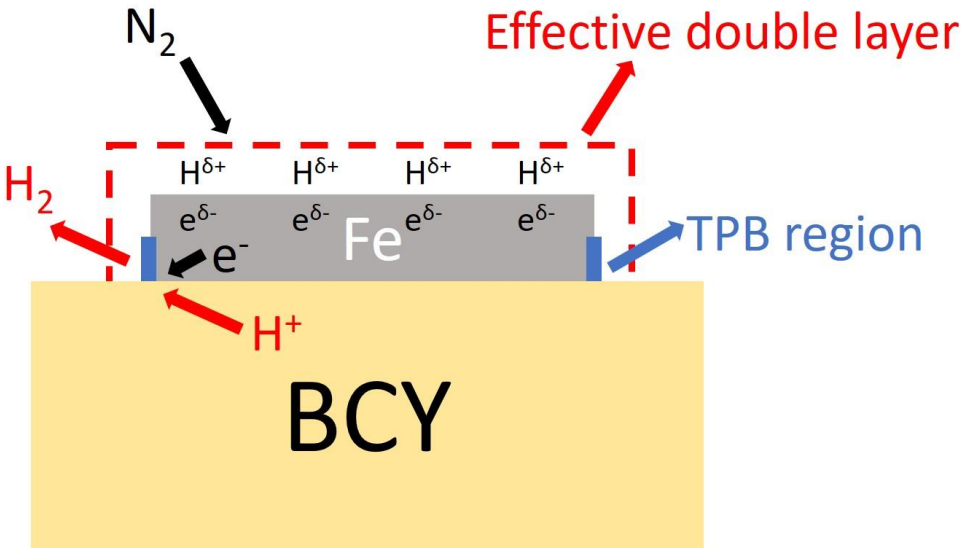

Fig. 6-11 A schematic image of N2 dissociation on the effective double layer and H2 formation at TPB.

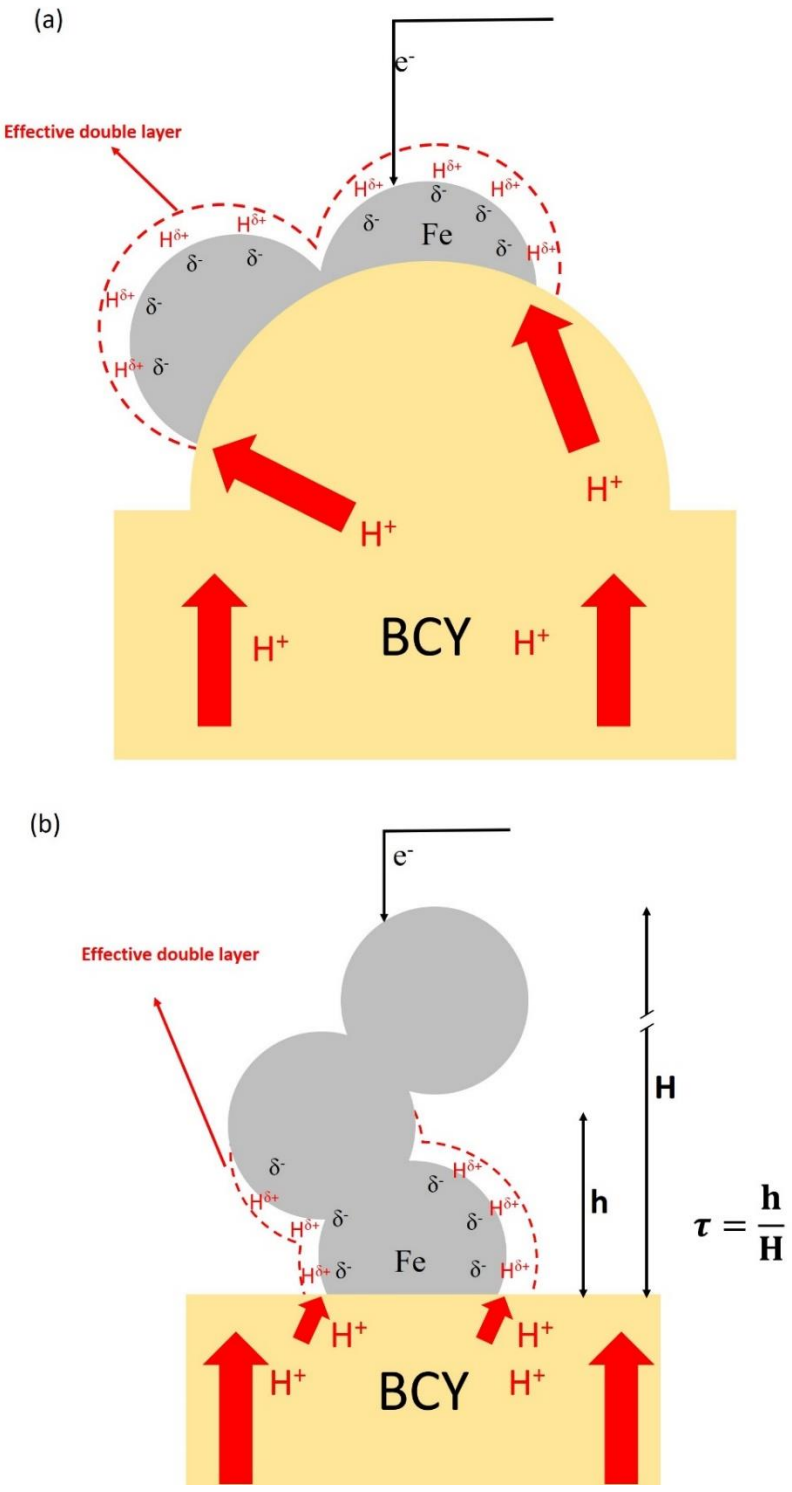

Fig. 6-12 Schematic images of effective double layer on Fe surface in (a) 10Fe–BCY and (b) porous pure Fe cathodes. *H*, *h*, and *τ*, are the electrode thickness, proton diffusion length, and the ratio of proton diffusion length to electrode thickness, respectively.

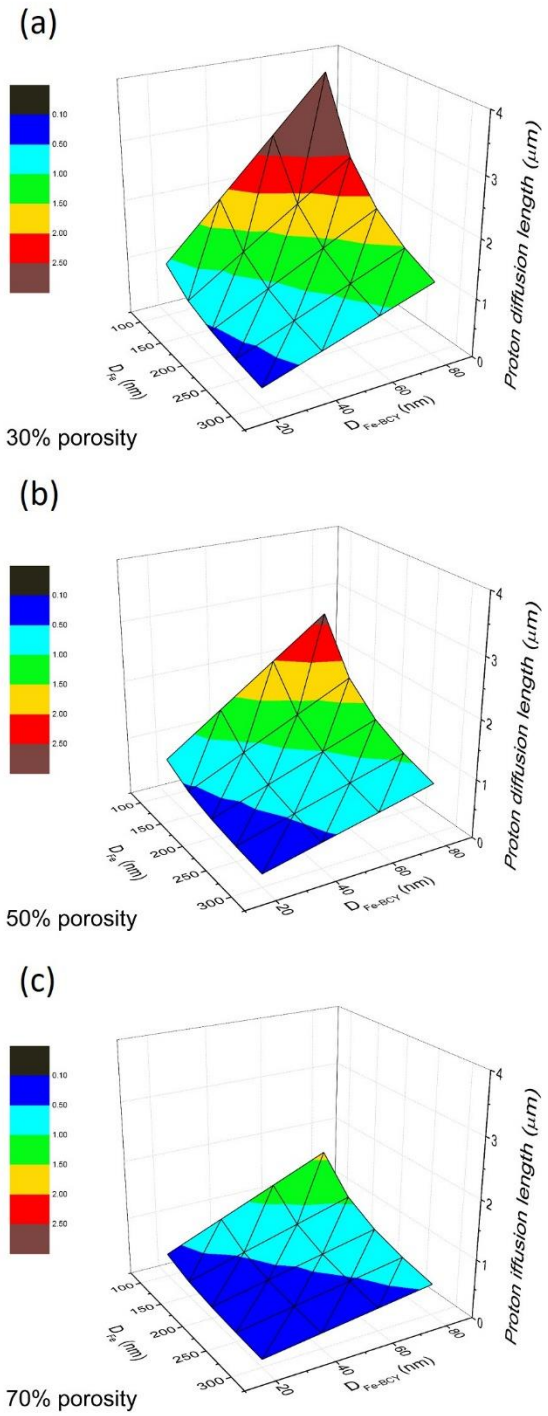

Fig. 6-13 The relationship among proton diffusion length, Fe particle diameter in 10Fe−BCY, and Fe particle diameter in porous pure Fe with (a) 30% porosity, (b) 50% porosity, and (c) 70% porosity in porous pure Fe, respectively.

Table 6-1 Summaries in chapters 3-5 and appendix J

Ch. 3	Cathode structures (Porous pure Fe cathode shows higher ammonia formation rate than cermet cathode)	Not charge-transfer reaction	1. Surface reaction 2. Not charge-transfer reaction 3. H_2 supply in the cathode
	W addition (W−Fe−BCY shows higher ammonia formation rate but lower current density than Fe−BCY)	Promotion of ammonia formation is dominant by electrode potential.	
Ch. 4	Reaction orders of hydrogen (α) and nitrogen (β) (α and β do not change after applying a negative voltage)	Surface reaction	
	H_2 partial pressure in the cathode (ammonia formation rate is dependent on H_2 partial pressure)	Not charge-transfer reaction	
Ch. 5	Deuterium isotope analysis ($NH_{3-x}D_x$ composition has a strong correlation to H_2 (D_2) species in the cathode)	Large contribution of surface reaction in the cathode.	
Appendix J	YSZ electrolyte (No promotion of ammonia formation in YSZ electrolyte)	Proton supply is needed.	Proton supply

Table 6-2 Relevant parameters in 10Fe-BCY

$m_{Fe\text{-}BCY}$	Counted particle number	$D_{Fe\text{-}BCY}$	$A_{Fe\text{-}BCY}$	$l_{Fe\text{-}BCY}$
(mg)	(-)	(nm)	(cm^2)	(cm)
0.1	120	42 ± 25	19.1 ± 14.3	9.0 ± 5.3

Table 6-3 Relevant parameters in porous pure Fe

m_{Fe}	φ	D_{Fe}	A_{Fe}	l_{Fe}
(mg)	(%)	(nm)	(cm^2)	(cm)
0.7	91	190 ± 108	5.0	5.8 ± 3.3

Table 6-4 Estimation of the proton diffusion length, τ, and relevant parameters in the porosity of 30%.

	D_i (cm)	$S^*_{eff,i}$ (cm^2)*	h (μm)*	τ (-)*
10Fe−BCY	42 ± 25	0.20 ± 0.02	-	-
Porous pure Fe	190 ± 108	0.41 ± 0.04	1.03 ± 0.11	0.08 ± 0.01

7. Systems design of ammonia electrochemical synthesis

7.1. Introduction

Based on the result in chapters 3-6, that the effect of EPOC is dominant in the electrochemical ammonia formation in our system is found. Compared with the electrochemical process which introduces pure N_2 into the cathode, to achieve the high ammonia formation rate, extra H_2 supply is necessary in the cathode. In chapter 1.4, two processes for electrochemical ammonia formation were mentioned: 1) the conventional electrochemical process (case 1) using N_2 and H_2O as reactants (i.e. without H_2 supply in the cathode). 2) EPOC dominated electrochemical process (case 2) using N_2 and H_2 as reactants (i.e. with H_2 supply in the cathode. In this chapter, the energy consumptions, reactor designing, and advantages are discussed for two electrochemical processes.

7.2. Energy consumption for ammonia formation rate

To estimate the energy consumption in the electrochemical process using a single compartment reactor and a dual compartment reactor, a continuous stirred-tank reactor (CSTR) was considered. Under this condition, the reactor design was ignored, and assumed the ammonia partial pressure was assumed to be 95% of the equilibrium ammonia partial pressure in the single compartment reactor (X_{equ} = 95%). Besides, no ammonia recycle stream was considered. The parameters were summarized in Table 7-1. Then, the symbols are summarized as below:

$\dot{m}_{i,j}$	Molar flow rate of compound i in steam or gas j (mol h^{-1})
$W_{com,N2}$	Work for compressing N_2 gas.
$C_{v,i}$	Heat capacity at constant volume of compound i
$C_{p,i}$	Heat capacity at constant pressure of compound i
T_j	Temperature in steam or gas j (K)
p_j	Pressure in steam or gas j (atm)
γ	The ratio of $\frac{C_p}{C_v}$

r_{NH3}	Rate of the electrochemical reaction of NH_3 formation
$W_{sep,N2}$	Work for N_2 separation.
R	Gas constant.
$W_{heat,H2O}$	Heat for heating water to water vapor.
$\Delta H_{vap,H2O}$	Enthalpy of vaporization for H_2O
$W_{com,H2O}$	Work for compressing water vapor.
$W_{ele,H2O}$	Work for water electrolysis
V_{th}	Theoretical voltage for water electrolysis
H	Overpotential for water electrolysis
$W_{ele,H2O}$	Work for electrochemical reaction of NH_3 formation
V_{app}	Applied voltage for NH_3 formation in this study
$\Delta H_{heat,4}$	Heat for heating the gaseous mixture to T_5 in case 1
$\Delta H_{cool,6}$	Heat for cooling the gaseous mixture to T_7 in case 1
$\Delta H_{heat,14}$	Heat for heating the water vapor to T_{15} in case 1
$\Delta H_{cool,16}$	Heat for cooling the gaseous mixture to T_{17} in case 1
$\Delta H_{heat,8}$	Heat for heating the gaseous mixture to T_9 in case 2
$\Delta H_{heat,6}$	Heat for heating the water vapor to T_7 in case 2
$\Delta H_{cool,11}$	Heat for cooling the gaseous mixture to T_{12} in case 2

The process for case 1 is shown in Fig. 7-1. The equations for case 1 are summarized as below:

$$\dot{m}_{N2,1} = \frac{0.79}{0.21}\dot{m}_{O2,1}$$

$$W_{com,N2} = \dot{m}_{N2,1}C_{v,N2}T_2[(\frac{p_3}{p_2})^{\frac{\gamma-1}{\gamma}}\text{-}1]$$

$$\dot{m}_{N2,3} + \dot{m}_{N2,10} = \dot{m}_{N2,4}$$

$$W_{sep,N2} = (\dot{m}_{N2,1} + \dot{m}_{O2,1})RT_1[\frac{\dot{m}_{N2,1}}{\dot{m}_{N2,1}+\dot{m}_{O2,1}}\ln\left(\frac{\dot{m}_{N2,1}}{\dot{m}_{N2,1}+\dot{m}_{O2,1}}\right) + \frac{\dot{m}_{O2,1}}{\dot{m}_{N2,1}+\dot{m}_{O2,1}}\ln\left(\frac{\dot{m}_{N2,1}}{\dot{m}_{N2,1}+\dot{m}_{O2,1}}\right)]$$

$$W_{com,H2O} = \dot{m}_{H2O,12}C_{v,H2O}T_{12}[(\frac{p_2}{p_1})^{\frac{\gamma-1}{\gamma}}\text{-}1]$$

$$\dot{m}_{H2O,13} + \dot{m}_{H2O,19} = \dot{m}_{H2O,14}$$

$$(\dot{m}_{N2,5}C_{v,N2} + \dot{m}_{NH3,5}C_{v,NH3} + \dot{m}_{H2,5}C_{v,H2})(T_6\text{-}T_5) + (\dot{m}_{N2,9}C_{v,N2})(T_{10}\text{-}T_9) = 0$$

$\Delta H_{heat,4} = (\dot{m}_{N2,4}C_{v,N2})(T_5\text{-}T_4)$

$\Delta H_{heat,14} = (\dot{m}_{H2O,14}C_{v,H2O})(T_{15}\text{-}T_{14})$

$\Delta H_{cool,6} = (\dot{m}_{N2,9}C_{v,N2} + \dot{m}_{NH3,9}C_{v,NH3} + \dot{m}_{H2,9}C_{v,H2})(T_7\text{-}T_6)$

$\Delta H_{cool,16} = (\dot{m}_{H2O,16}C_{v,H2O} + \dot{m}_{O2,16}C_{v,O2})(T_{17}\text{-}T_{16})$

$\dot{m}_{N2,4} - 0.5r_{NH3} = \dot{m}_{N2,5}$

$\dot{m}_{H2O,14} - 1.5r_{NH3} - r_{H2} = \dot{m}_{H2O,15}$

$W_{heat,H2O} = \dot{m}_{H2O,11}[C_{v,H2O}(T_{12}\text{-}T_{11}) + \Delta H_{vap,H2O}]$

$W_{ele,NH3} = 1.576I$

$\dot{m}_{N2,5}C_{v,N2}(T_6\text{-}T_5) + \dot{m}_{N2,9}C_{v,N2}(T_{10}\text{-}T_9) + \dot{m}_{H2,5}C_{v,H2}(T_6\text{-}T_5) + \dot{m}_{NH3,5}C_{v,H2}(T_6\text{-}T_5) = 0$

$\dot{m}_{H2O,15}C_{v,H2O}(T_{16}\text{-}T_{15}) + \dot{m}_{H2O,18}C_{v,H2O}(T_{19}\text{-}T_{18}) + \dot{m}_{O2,15}C_{v,O2}(T_{16}\text{-}T_{15}) = 0$

The process for case 2 is shown in Fig. 7-2. The equations for case 2 are summarized as below:

$\dot{m}_{N2,1} = \frac{0.79}{0.21}\dot{m}_{O2,1}$

$W_{com,N2} = \dot{m}_{N2,1}C_{v,N2}T_2[(\frac{p_3}{p_2})^{\frac{\gamma-1}{\gamma}}\text{-}1]$

$\dot{m}_{N2,3} + \dot{m}_{N2,13} = \dot{m}_{N2,8}$

$W_{sep,N2} = (\dot{m}_{N2,1} + \dot{m}_{O2,1})RT_1[\frac{\dot{m}_{N2,1}}{\dot{m}_{N2,1}+\dot{m}_{O2,1}}\ln\left(\frac{\dot{m}_{N2,1}}{\dot{m}_{N2,1}+\dot{m}_{O2,1}}\right) + \frac{\dot{m}_{O2,1}}{\dot{m}_{N2,1}+\dot{m}_{O2,1}}\ln\left(\frac{\dot{m}_{N2,1}}{\dot{m}_{N2,1}+\dot{m}_{O2,1}}\right)]$

$W_{com,H2O} = \dot{m}_{H2O,5}C_{v,H2O}T_5[(\frac{p_2}{p_1})^{\frac{\gamma-1}{\gamma}}\text{-}1]$

$\dot{m}_{H2,7} + \dot{m}_{H2,15} = \dot{m}_{H2,8}$

$(\dot{m}_{N2,9}C_{v,N2} + \dot{m}_{NH3,9}C_{v,NH3} + \dot{m}_{H2,9}C_{v,H2})(T_{10}\text{-}T_9) + (\dot{m}_{N2,12}C_{v,N2} + \dot{m}_{H2,12}C_{v,H2})(T_{14}\text{-}T_{15}) = 0$

$(\dot{m}_{N2,9}C_{v,N2} + \dot{m}_{NH3,9}C_{v,NH3} + \dot{m}_{H2,9}C_{v,H2})(T_{11}\text{-}T_{10}) + (\dot{m}_{N2,12}C_{v,N2} + \dot{m}_{H2,12}C_{v,H2})(T_{13}\text{-}T_{14}) = 0$

$\Delta H_{heat,8} = (\dot{m}_{N2,8}C_{v,N2} + \dot{m}_{H2,8}C_{v,H2})(T_9\text{-}T_8)$

$\Delta H_{cool,11} = (\dot{m}_{N2,11}C_{v,N2} + \dot{m}_{NH3,11}C_{v,NH3} + \dot{m}_{H2,11}C_{v,H2})(T_{12}\text{-}T_{11})$

$\dot{m}_{N2,8} - 0.5r_{NH3} = \dot{m}_{N2,9}$

$W_{heat,H2O} = \dot{m}_{H2O,4}[C_{v,H2O}(T_5\text{-}T_4) + \Delta H_{vap,H2O}]$

$W_{ele,H2O} = 1.4I$

$W_{ele,NH3} = 0.494I$

$\dot{m}_{N2,3}C_{v,N2}(T_8\text{-}T_3) + \dot{m}_{N2,13}C_{v,N2}(T_8\text{-}T_{15}) + \dot{m}_{H2,9}C_{v,H2}(T_8\text{-}T_7) + \dot{m}_{H2,13}C_{v,H2}(T_8\text{-}T_{15}) = 0$

$$\Delta H_{heat,6} = \dot{m}_{H2O,8} C_{v,H2O}(T_7 - T_6)$$

$$C_{v,i} = A + B\frac{T}{1000} + C\frac{T^2}{1000^2} + D\frac{T^3}{1000^3} + E\frac{1000^2}{T^2}$$

Table Parameters of C_v for N_2, H_2, H_2O, and NH_3.[116]						
	A	B	C	D	E	Temperature range
N_2 (g)	28.98641	1.853978	-9.647459	16.63537	0.000117	100 – 500K
N_2 (g)	19.50583	19.88705	-8.598535	1.369784	0.527601	500 – 2000K
H_2 (g)	33.066178	-11.363	11.432816	-2.772874	-0.158558	298 – 1000K
H_2O (l)	-203.606	1523.29	-3196.413	2474.455	3.855326	298 – 500K
H_2O (g)	30.092	6.83251	6.793435	-2.53448	0.082139	500 – 1700K
NH_3 (g)	19.99563	49.77119	-15.37599	1.921168	0.189174	298 – 1400K
O_2 (g)	31.32234	-20.235	57.8664	-36.50624	-0.007374	100 – 700K

In case 1, H_2O and N_2 are used to react to ammonia directly. Pure H_2O is introduced into the anode, and pure N_2 is introduced into the cathode. Therefore, the reactor in case 1 needs to have two compartments for ammonia formation. In case 2, the reactor for ammonia formation can be a single compartment, where a gaseous mixture of 50% N_2–50% H_2 are introduced. However, to reduce carbon emissions, H_2 must be obtained by the water electrolysis process, which indicates that another reactor is needed for the water electrolysis process.

In the next section, the energy consumption for water electrolysis, N_2 separation, and electrochemical ammonia formation are discussed, respectively.

7.2.1. Water electrolysis

In case 1, because H_2O is used directly to form ammonia, the process does not need the water electrolysis process. Water is evaporated to form steam and isentropically compressed to 10 atm. Then, the steam (steam 13 in Fig. 7-1) mixed with recycled steam (steam 19 in Fig. 7-1) is flowed into the anode.

In case 2, for the process of water electrolysis, the applied voltage of 1.4 V using solid oxide electrolysis cell (SOEC) technology is assumed. To obtain the ammonia production of 2.45×10^5 mol h^{-1}, the needed amount of water is 3.68×10^5 mol in an hour. Steam is produced from the water feedstock and compressed isentropically to 10 atm, which causes the steam temperature to increase to 654.5K. Then, the steam is flowed into the SOEC device. The water electrolysis process costs 99283.07 MJ, which is the multiple of the applied voltage (1.4 V) and current, and release 8195.62 MJ as heat. The reactant gas is heated from 654.5K to 973K by heat recycling, which is around 44% of heat in the water electrolysis. The energy costs for heating to water vapor, isentropic compression, and hydrogen production are 16789.65 MJ, 2802.78 MJ, and 99283.07 MJ in an hour, respectively. Then, the H_2 gas (gas 7 in Fig. 7-2) mixed with N_2 gas (gas 3 in Fig. 7-2) and recycled gas (gas 13 in Fig. 7-2) is introduced into the reactor for ammonia formation.

7.2.2. N_2 separation

In case 1 and case 2, the needed amount of N_2 is the same as 1.23×10^5 mol in an hour. Pure nitrogen is obtained by separating N_2 from air. The energy consumption for N_2 separation is calculated by thermodynamics, which is the product of the operating temperature and the difference in entropy. Therefore, the energy consumption for N_2 separation is 197.45 MJ in an hour. Then, the N_2 gas is isentropically compressed to 10 atm with the gas temperature increasing from 298K to 575K, which costs 715.82 MJ in an hour. In case 1, the N_2 gas (gas 3 in Fig. 7-1) mixed with the recycled N_2 (gas 10 in Fig. 7-1) is introduced into the cathode in the reactor for ammonia formation. In case 2, a gaseous mixture of the N_2 gas mixed with H_2 gas and the recycled gases is introduced into the reactor for ammonia formation.

7.2.3. Electrochemical reaction of ammonia formation

In case 1, the pure N_2 and H_2O are introduced into the cathode and anode, respectively. Then, the power supply for ammonia electrosynthesis is determined by the product of the applied voltage and current. Here, the applied voltage of 1.59 V and the current efficiency of 65% are assumed, which indicates that H_2 is also formed in the cathode. The energy consumption for ammonia electrosynthesis is 173267.35 MJ in an hour, and release 89010.16 MJ as heat. The reactant stream or gas are heated to 823K by the heat recycling (gas 4 and steam 14 in Fig. 7-1).

In case 2, a gaseous mixture of 50% N_2−50% H_2 is introduced into the reactor for ammonia formation. Here, the applied voltage of 0.53 V and the current efficiency of 65% are assumed. The low applied voltage is caused by H_2 using as a reactant. The required voltage using N_2 and H_2O as reactants is much larger than that using N_2 and H_2 as reactants by thermodynamics (Fig. 1-3). The energy consumption for ammonia electrosynthesis is 58213.73 MJ in an hour, and release 71350.88 MJ heat. The reactant gas is heated from 640.5K to 823K by heat recycling (gas 8 in Fig. 7-2). Notably, two heat recycle systems are used in case 2 to reduce heat loss because the low NH_3 partial pressure needs to be collected at very low temperature.

7.3. Comparison with Haber-Bosch process and electrochemical reaction of ammonia formation

In case 1, the main energy consumption process is the electrochemical ammonia formation, which utilizes 83% of the total energy consumption. In case 2, the main energy consumption process is water electrolysis, which consumes 56% of the total energy. The process of electrochemical ammonia formation only uses 33% of the total energy consumption. Fig. 7-3 shows a comparison with the energy consumption in case 1, case 2, and the Haber-Bosch process at different current efficiencies. The energy consumption for the Haber-Bosch process is the same at different current efficiencies. With increasing the current efficiency for ammonia formation, the total energy consumptions decrease in case 1 and case 2. Notably, the energy consumption in case 2 at 50% current efficiency is mostly comparable to that in the Haber-Bosch process.

On the other hand, Fig. 7-4 shows the required Fe mass with the ammonia production of 100 tons/day. In this study, the ammonia formation rate is 1800 μg mg^{-1} h^{-1} at 0.1 MPa and 550°C with a flow rate of 700 sccm, respectively, which is comparable to that in the Haber−Bosch process (976 μg mg^{-1} h^{-1} at 10 MPa and 400°C). The corresponding required Fe mass is between 3 tons for the electrochemical process. In the practical application, the operating pressure needs to be increased to achieve a high ammonia concentration at equilibrium, which increases the ammonia formation rate as well. To estimate the ammonia formation rate at high operating pressure, two approaches, kinetic and thermodynamic analysis, are performed. 1) In the kinetic analysis, a previous study pointed out that the reaction order of hydrogen was 0.76 using Fe catalyst when H_2 partial pressure was between 5 and 15 atm and N_2 pressure was fixed at 5 atm.[117] This result indicates that hydrogen poisoning does not occur on Fe catalyst at high hydrogen partial pressure.

Therefore, based on Eq. 4-2, the ammonia formation rate in 50% H_2−50% N_2 could reach around 5500 μg mg^{-1} h^{-1} at 0.2 MPa and the corresponding required Fe mass is about 1 ton. 2) On the other hand, in the thermodynamic analysis, a previous study pointed out that the ratio of obtained ammonia partial pressure to the ammonia partial pressure at equilibrium does not change when the operating pressure increased from 3 to 15 MPa.[8] In this study, the ratio is around 7% at 0.1 MPa. Supposing that the ratio is the same as 7% at 0.2 MPa, the ammonia formation rate will increase from 1800 μg mg^{-1} h^{-1} at 0.1 MPa to 7152 μg mg^{-1} h^{-1} at 0.2 MPa. Therefore, considering the energy consumption, ammonia formation rate, and required Fe mass, the electrochemical process can compete with the Haber−Bosch process.

In terms of the reactor design, the ammonia production is hard to alter in the Haber-Bosch process because when the operating pressure is changed, it takes a long time for the reaction to reach a new equilibrium state. Therefore, the Haber-Bosch process is difficult to integrate with renewable energy because of its unstable nature. Therefore, the process of electrochemical ammonia formation at 1 MPa (10 atm) is suitable to combine with renewable energy. Between the reactors in case 1 and case 2 for the electrochemical ammonia formation, the reactor is two compartments in case 1, and that is a single compartment in case 2. In case 2, a single compartment reactor has several advantages including an easy change in operating pressure, avoidance of gas flow leakage, and enhancement of catalytic reaction area. In two compartments reactor, the gas flows in the cathode and in the anode need to be separated, which requires the cell electrolyte to have no cracks. Therefore, when a change of operating pressure is desired, the pressures in the cathode and anode need to be changed at the same time to avoid crack formation due to pressure difference. Also, the gas seal between the atmosphere and cathode or anode also needs to be concerned at high operating pressure. Besides, the two compartment reactor is difficult to increase the reaction area of catalyst for ammonia formation. On the other hand, for the single compartment reactor, the issues motioned above can be avoided. However, a disadvantage in case 2 is that another reactor for water electrolysis is needed.

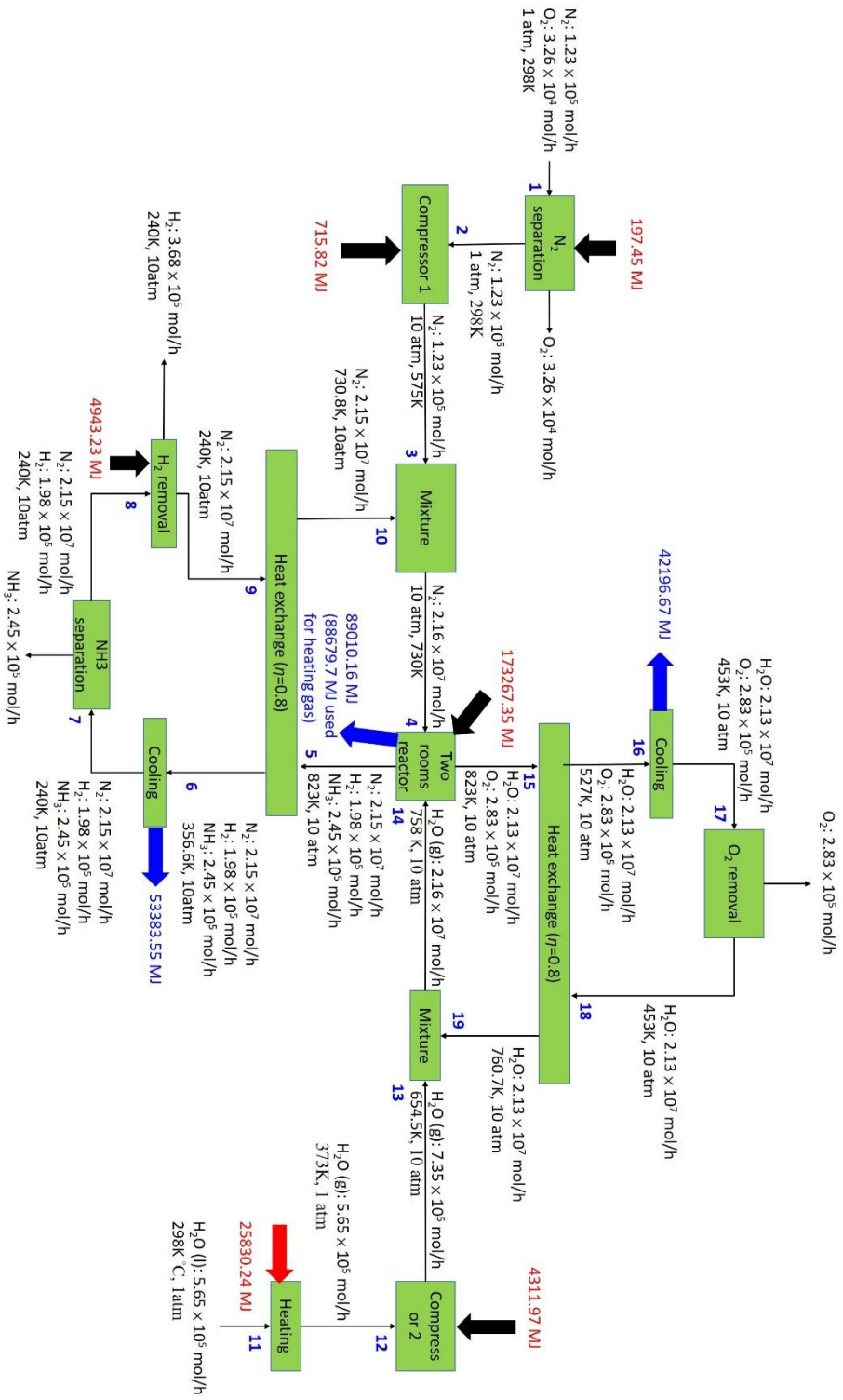

Fig. 7-1 Quantitative representation of case 1 with 65% current efficiency for an ammonia production of 100 ton/day

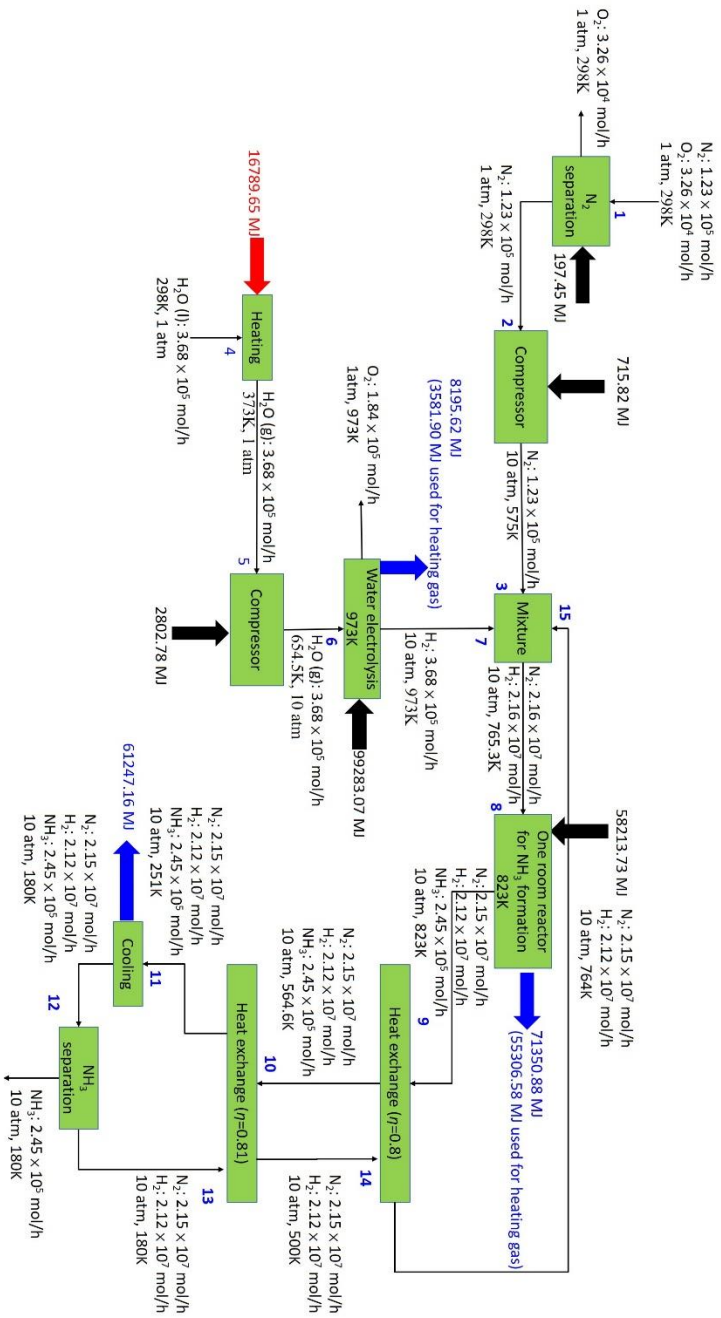

Fig. 7-2 Quantitative representation of case 2 with 65% current efficiency for an ammonia production of 100 ton/day.

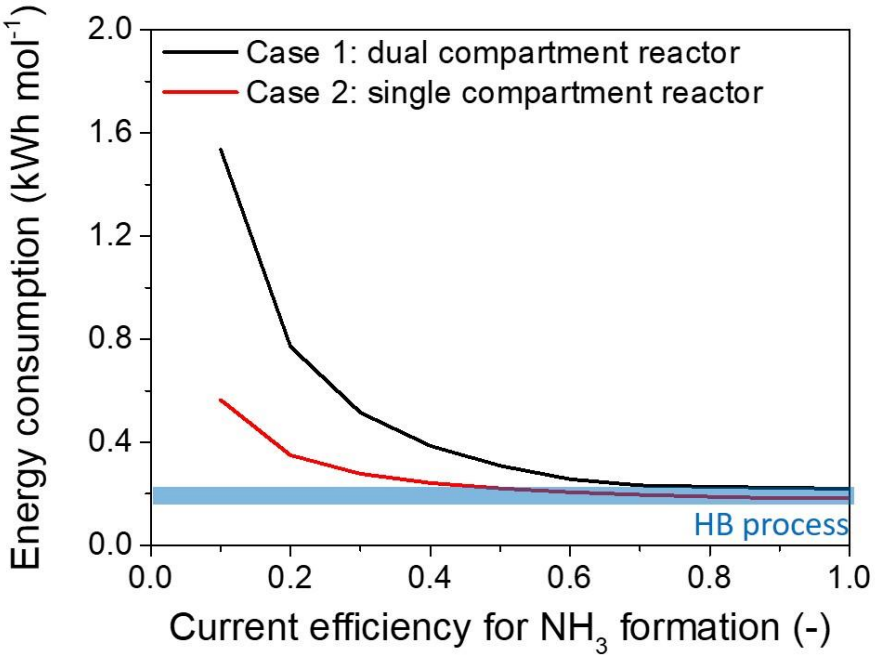

Fig. 7-3 Energy consumption for case 1, case 2, and the Haber-Bosch process with different current efficiencies.

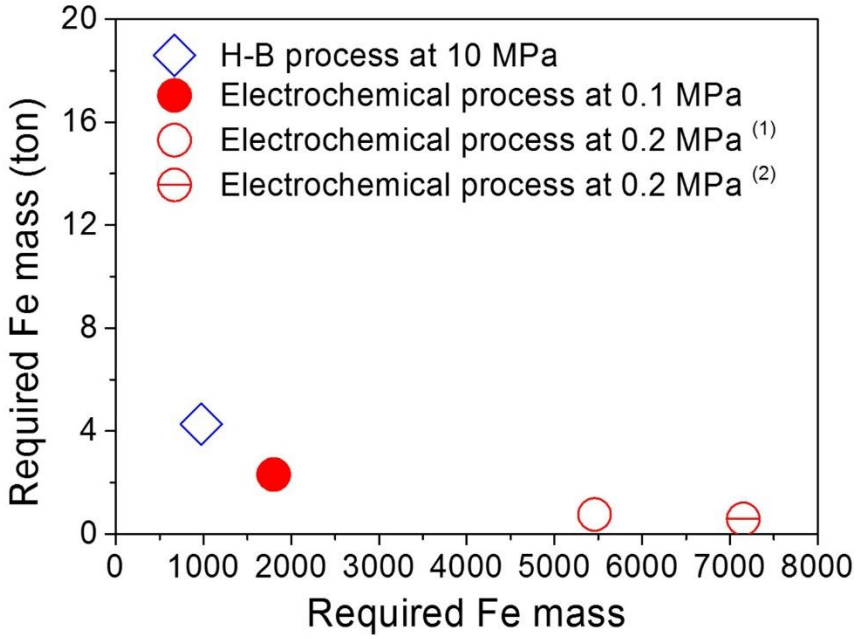

Fig. 7-4 Required Fe mass for the electrochemical process and Haber-Bosch. (1) and (2) are estimated by the kinetic and thermodynamic analysis, respectively.

Table 7-1 Parameters in CSTR for a production rate of 100 tons ammonia per day.

	Case 1 (dual compartment reactor)	Case 2 (single compartment reactor)	Remarks
Temperature	823K	823K	
Pressure	10 atm	10 atm	
Ammonia formation rate[*1] (mol s^{-1} cm^{-2})	2.19×10^{-6}	2.19×10^{-6}	$r = k[p_{H2}]^{\alpha}[p_{N2}]^{\beta}$ $r = 5.5 \times 10^{-8}$ at 1 atm in this study.
Ammonia formation rate[*1] (μg mg^{-1} h^{-1})	7.52×10^{4}	7.52×10^{4}	$r = k[p_{H2}]^{\alpha}[p_{N2}]^{\beta}$ $r = 1800$ at 1 atm in this study.
Required Fe mass (kg)	50	50	
Required electrode area (m^2)	3100	3100	
X_{equ}	-	95%	
Current efficiency[*2]	65%	65%	The efficiency is 65% in this study.
Current (A)	1.97×10^{7}	1.97×10^{7}	
By product H_2 recycle	No	Yes	
Heat recycle	Yes	Yes	

[*1]: Supposed that the ammonia formation rate does not change at high flow rate. The ammonia formation rate in case 1 is the same as that in case 2.

[*2]: Supposed that current efficiency does not change at high flow rate. The current efficiency in case 1 is the same as that in case 2.

8. Summary

8.1. Concluding remarks

In this study, for the practical applications of electrochemical ammonia formation, the mechanism of electrochemical promotion, performance, and energy consumption for ammonia formation were discussed. The reaction mechanism was investigated by using different cathode structures, kinetics analysis, controlling H_2 and N_2 partial pressure in the cathode, and deuterium isotope analysis. Based on the results, four points are summarized: 1) The effect of electrode potential on ammonia formation is more important than that of current density. 2) The reaction is dominated by the surface reaction rather than the charge-transfer reaction. 3) H_2 supply in the cathode can efficiently improve ammonia formation rate. 4) Proton supply from the electrolyte is significant for ammonia formation.

In chapter 3, that the ammonia formation rate can be significantly improved with cathodic polarization was found. In a comparison of the performance of ammonia formation for different cathode structures, porous pure Fe cathode, which has short TPB length, has a better performance than (0.5W−)10Fe−BCY cermet electrode. Also, the effect of increasing Fe amount cannot improve the ammonia formation rate in the electrochemical reaction. This result implies that ammonia is formed via the surface reaction with EPOC rather than the charge-transfer reaction at the TPB.

In chapter 4, that the values of reaction orders of hydrogen and nitrogen do not change with applying voltage was found, suggesting that the surface reaction with EPOC is dominating in the electrochemical reaction. Furthermore, through increasing H_2 partial pressure and the flow rate in the cathode, the performance of ammonia formation is improved in porous pure Fe cathode, which implies that the electrochemical ammonia formation is dominated by the surface reaction with EPOC. An outstanding ammonia formation rate of around 1800 μg mg^{-1}_{Fe} h^{-1} in a gaseous mixture of 50% H_2−50% N_2 with 700 sccm at 550°C was found, which is comparable to the ammonia formation rate in the H-B process.

In chapter 5, the deuterium isotope analysis is used to investigate the mechanism of electrochemical promotion. Through observation of ammonia compositions ($NH_{3-x}D_x$), that surface reaction is dominant in the electrochemical ammonia formation because the H (or D) atoms in main ammonia product correspond to the species of H_2 (or D_2) in the cathode is confirmed. Also,

that surface reaction is dependent on the applied voltage and H_2 partial pressure in the cathode was found in the electrochemical reaction. At high H_2 partial pressures, the surface reaction was observed to have a much higher contribution to the ammonia formation than the charge transfer reaction.

In chapter 6, a possible reaction mechanism, EPOC, was proposed. Furthermore, based on the performance of ammonia formation for 10Fe−BCY and porous pure Fe cathodes, two possibilities and a new parameter, proton diffusion length, were proposed. For the first approach, the current density for 10Fe−BCY is 40% larger than that for porous pure Fe, whereas the TPB length for 10Fe−BCY is 243 times longer than that for porous pure Fe. Therefore, that there are isolated Fe particles in 10Fe−BCY, which is not connecting with the network structure of electrons, was assumed. For the second approach, the assumption that the active H_2 evolution reaction occurring in the TPB region hinders N_2 adsorption and dissociation on the Fe surface near to the TPB region was proposed. Therefore, the surface area for ammonia formation should be modified by subtracting the area for the H_2 evolution reaction, i.e. the TPB region. The results of two mechanisms point out that the proton diffusion length is around several micrometers, which indicates that the thickness is too long for the porous pure Fe.

Based on the results in chapters 3-6, that the mechanism of electrochemical promotion of ammonia formation is caused by the surface reaction with EPOC was confirmed. A possible direction for designing cathode structure, i.e. reducing the TPB length and the thickness of electrode to several micrometers, was proposed. Also, an outstanding ammonia formation of around 1800 $\mu g\ mg^{-1}_{Fe}\ h^{-1}$ was observed, which has the potential to be implemented.

In chapter 7, the energy consumptions for the Haber−Bosch process and the process of electrochemical ammonia formation were compared. When the current efficiency achieves over 50% in the electrochemical ammonia formation, the energy consumption is mostly similar to that in the Haber-Bosch process. Also, for cooperation with renewable energy, the reactor needs a property of flexible operation for ammonia production, which can adjust production rate, quick start-up, and shut-down. Therefore, the process of electrochemical ammonia formation with low operating pressure is perfect for cooperation with renewable energy. On the other hand, in the electrochemical process of ammonia formation, it can be divided into a dual compartment reactor using H_2O and N_2 and a single compartment reactor using H_2 and N_2. To achieve a high ammonia formation rate, the single compartment reactor operating under a gaseous mixture of H_2 and N_2

into the cathode is considered. The ammonia formation rate can reach 5500−7000 μg mg^{-1} h^{-1} (1.7×10^{-7} – 2.1×10^{-7} mol s^{-1} cm^{-2}) in a gaseous mixture of H_2−N_2 at 0.2 MPa by the kinetic analysis and thermodynamic kinetic analysis, which is much better than that in the Haber−Bosch process at 10 MPa. Furthermore, the advantages of the single compartment reactor possess changing operating pressure, avoiding leakage of flow gas, and increasing the reaction area for ammonia formation.

Through the investigation of the reaction mechanism, these results can improve the cathode design. Based on our predictions of energy efficiency and ammonia formation rate at high operating pressure, we conclude that the electrochemical process has the potential to replace the Haber−Bosch process and achieve a high ammonia formation rate with low amounts of Fe. Our research can significantly help the reactor designing for ammonia formation and has the potential to be implemented.

8.2. Future outlook

In this thesis, an alternate electrochemical process, in which uses H_2 and N_2 as reactants, was proposed to achieve a very high ammonia formation rate. Furthermore, considering the energy consumption and reactor design, this electrochemical process has several advantages in a comparison with the conventional electrochemical process, which using N_2 and H_2O as reactants. The results in this study can significantly help the reactor designing of electrochemical ammonia formation integrated with renewable energy in decentralized and small-scale plants.

To accelerate the practical implementation, a decrease in operating temperature and an increase in operating temperature must be developed. In the Haber−Bosch process, the operating temperature and pressure are around 450°C and 10 MPa. If the operating temperature in the electrochemical process decreases from 550 to 450°C, it can significantly increase the ammonia partial pressure and decrease the energy consumption in the process of ammonia gas separation. Also, as mentioned in chapter 7, when the operating pressure is increased to 0.2 MPa in the electrochemical process, the ammonia formation rate can be significantly increased, which is around 5–7 times larger than that in the Haber–Bosch process.

In this study, the possible mechanism for electrochemical ammonia formation, i.e. EPOC, was proposed. To further understand the mechanism, it is necessary to prove the existence of effective double layer and explore proton diffusion length. The result can help cathode design, i.e. cathode thickness, and improve ammonia formation rate in the electrochemical reaction.

In terms of engineering, in a comparison with a dual compartment reactor, a single compartment reactor is more suitable for the electrochemical process using H_2 and N_2 as reactants. Also, a single compartment reactor has some advantages including low cost and flexible adjustment of operating pressure. The single compartment reactor with the electrochemical process has the potential to be implemented and replace the Haber−Bosch process for ammonia synthesis.

Appendix

A. The relationship between the area of NH_3 FTIR spectra and gas tubing temperature

The area of NH_3 FTIR spectra was examined at different gas tubing temperatures, as shown in Fig. A. The gaseous mixture of NH_3−N_2 was introduced into an optical cell directly. It showed that the NH_3 area did not change between the gas tubing temperature of 80 − 200°C. This result indicates that the amount of NH_3 adsorption on the surface of gas tubing can be ignored.

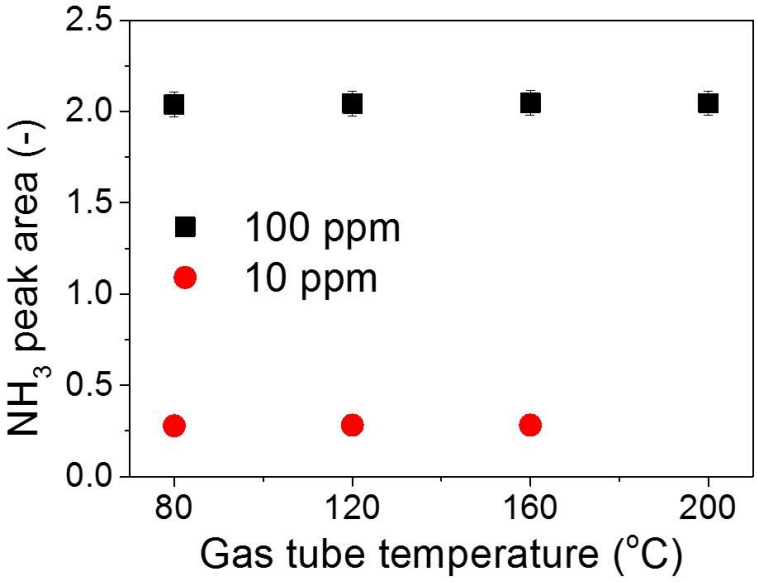

Fig. A Obtained NH_3 area at different gas tubing temperature.

B. Ammonia decomposition reaction test

Because the reaction was performed at high temperature, according to the thermodynamics, ammonia probably decomposed into N_2 and H_2 on the quartz tube and cell. Therefore, a test for ammonia decomposition reaction was conducted using an Al_2O_3 plate (i.e., a dummy cell without the cathode) and a single cell with porous pure Fe electrode, as shown in Fig. B.

First, a gaseous mixture of 50 ppm NH_3–5% D_2–45% Ar–50% N_2 was introduced into the captured solution at ambient temperature. Then, the gaseous mixture was introduced into the device using the Al_2O_3 plate, as shown in Fig. B(a). The ammonia concentration at 600°C decreased by 10% as that at ambient temperature, which indicated that ammonia could slightly decompose on the quartz tube or the Al_2O_3 plate at/below 600°C

Second, a test for ammonia decomposition reaction on porous pure Fe was performed. The gaseous mixture was changed to 100 ppm NH_3–N_2, and the obtained ammonia concentration was 81 ppm at ambient temperature, which suggested that a part of ammonia was adsorbed on the gas tubing surface. Subsequently, the gaseous mixture was introduced into the porous pure Fe cathode at 500°C–600°C, as shown in Fig. B(b). The obtained ammonia concentrations were 25 ppm at 600°C and 50 ppm at 500°C, which suggests that the reverse reaction of NH_3 occurred on the Fe electrode between 500–600°C.

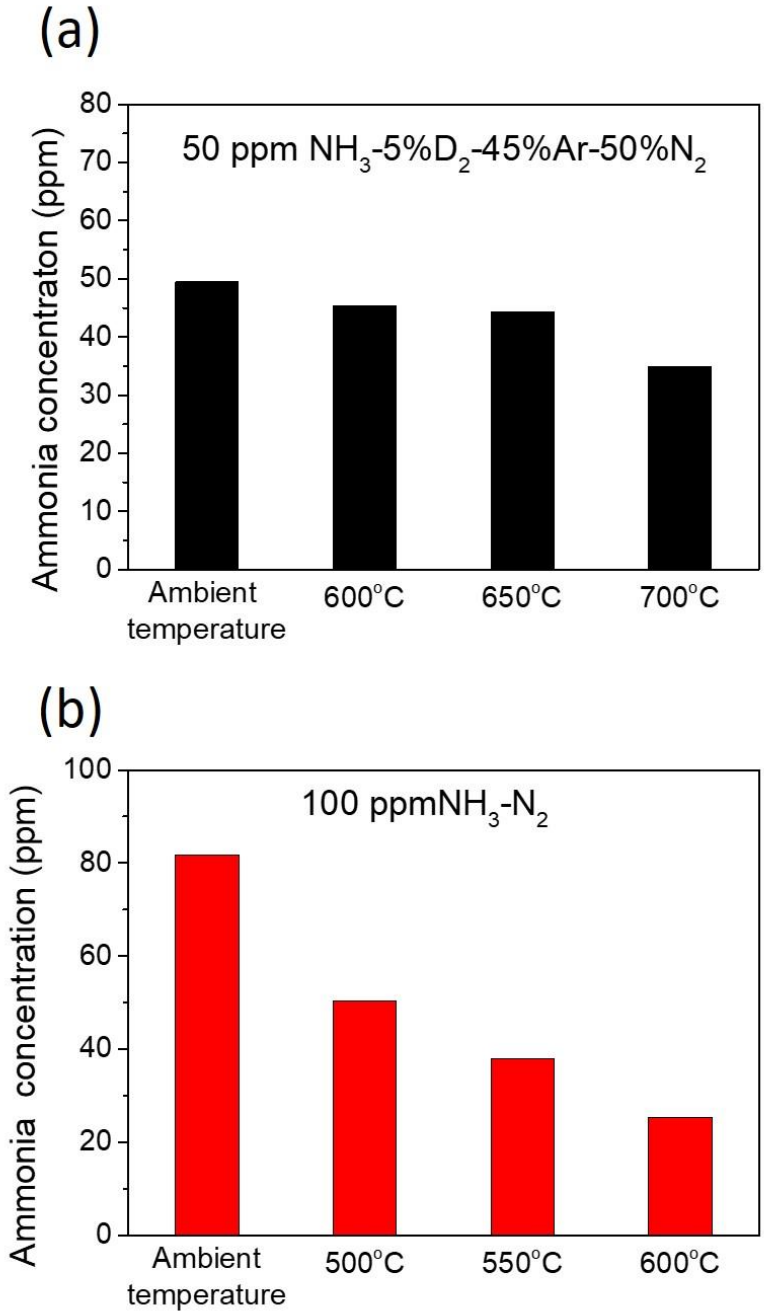

Fig. B Tests for ammonia decomposition reaction using (a) Al_2O_3 plate without cell in 50 ppm NH_3–5% D_2–45% Ar–50% N_2 and (b) porous pure Fe cathode in 100 ppm NH_3–N_2.

C. TG measurement for Fe_2O_3 powder

The reduction reaction of Fe_2O_3 powder was conducted by TG-DTA in 3%H_2, as shown in Fig. C. The Fe_2O_3 weight was decreased by around 30% at 900°C, which corresponded to the weight loss of Fe_2O_3 reduction to Fe. After reduction, the sample was decreased from 900°C to 550°C, and the weight loss of 30% did not change, which suggests that the metallic Fe phase will be maintained in the cathode at the operating temperature of around 550°C for the electrochemical ammonia formation.

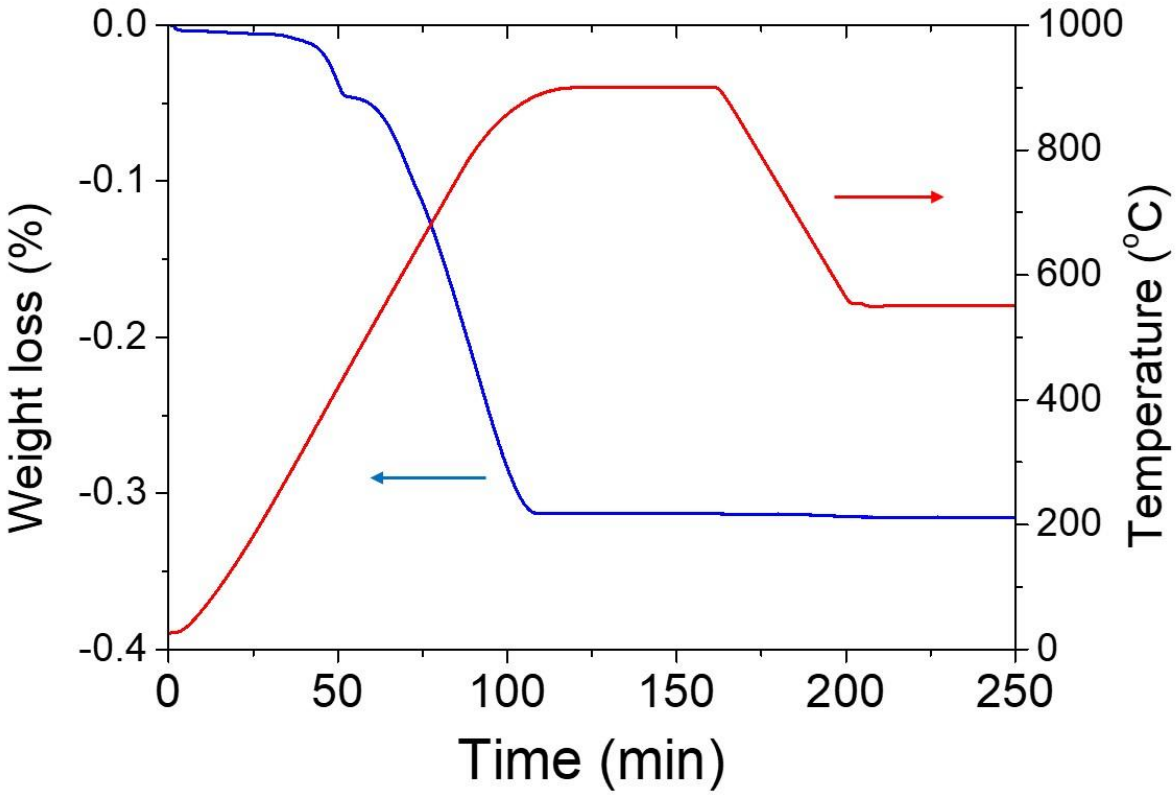

Fig. C TG-DTA measurement for Fe_2O_3 powder in dry 3% H_2/Ar and temperature with heating rate of 10°C/min.

D. Blank test for ammonia electrosynthesis

Experimental condition

Gas in the cathode: 10% H_2–90% Ar with 40 sccm

Gas in the anode: wet 20% H_2–80% Ar with 30 sccm

Temperature: 550°C

Catalyst: porous pure Fe (15 μm)

Fig. D shows a blank test in a gaseous mixture of 10% H_2–90% Ar using porous pure Fe (15 μm). A low ammonia formation rate of around 2×10^{-12} mol cm^{-2} s^{-1} was obtained at different applied voltages. However, the detection limit of ammonia formation rate was around 2×10^{-12} mol cm^{-2} s^{-1} for HPLC equipment. Therefore, no ammonia formation was observed under the condition of 10% H_2–90% Ar at 550°C.

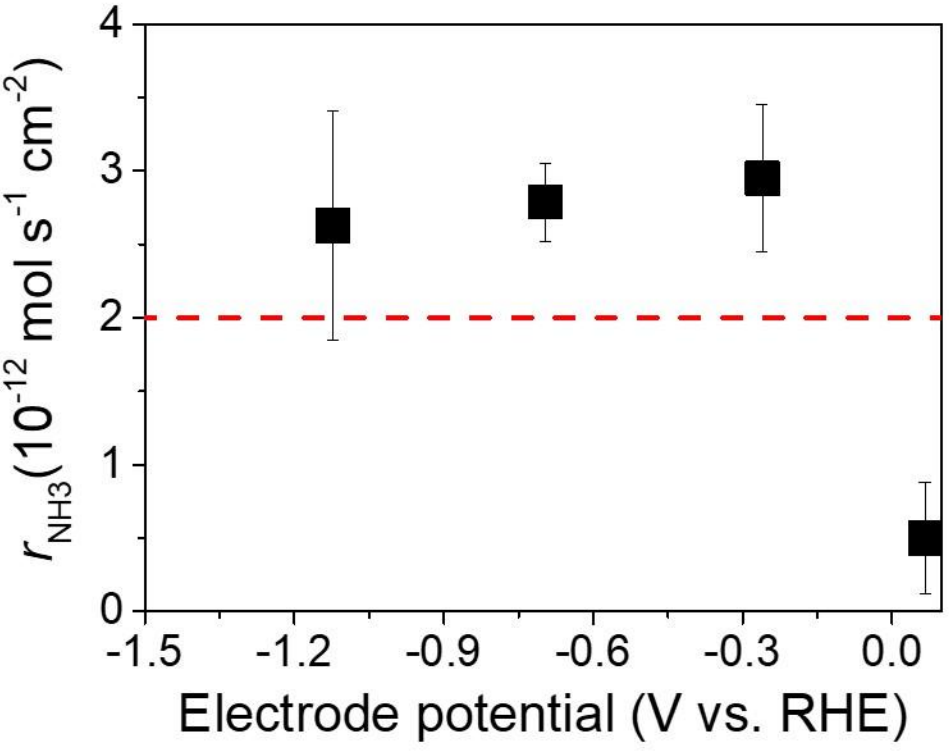

Fig. D Blank test in 10% H_2–90% Ar using porous pure Fe cathode at 550°C. The red broken line is the detection limit of HPLC.

E. Reversible test for ammonia electrochemical synthesis

Experimental condition

Gas in the cathode: 10% H_2–90% N_2 with 40 sccm

Gas in the anode: wet 20% H_2–80% Ar with 30 sccm

Temperature: 550°C

Catalyst: porous pure Fe (30 μm)

To check the effect of electrochemical promotion of ammonia formation, a reversible test with forward and reverse changes of electrode potential was conducted at 550°C in a gaseous mixture of 10% H_2–90% N_2, as shown in Fig. E. The ammonia formation rate has a positive correlation with cathodic polarization, which suggests that the promotion of ammonia formation rate in this study was caused by the electrochemical promotion and not just by the reduction of the Fe electrode itself.

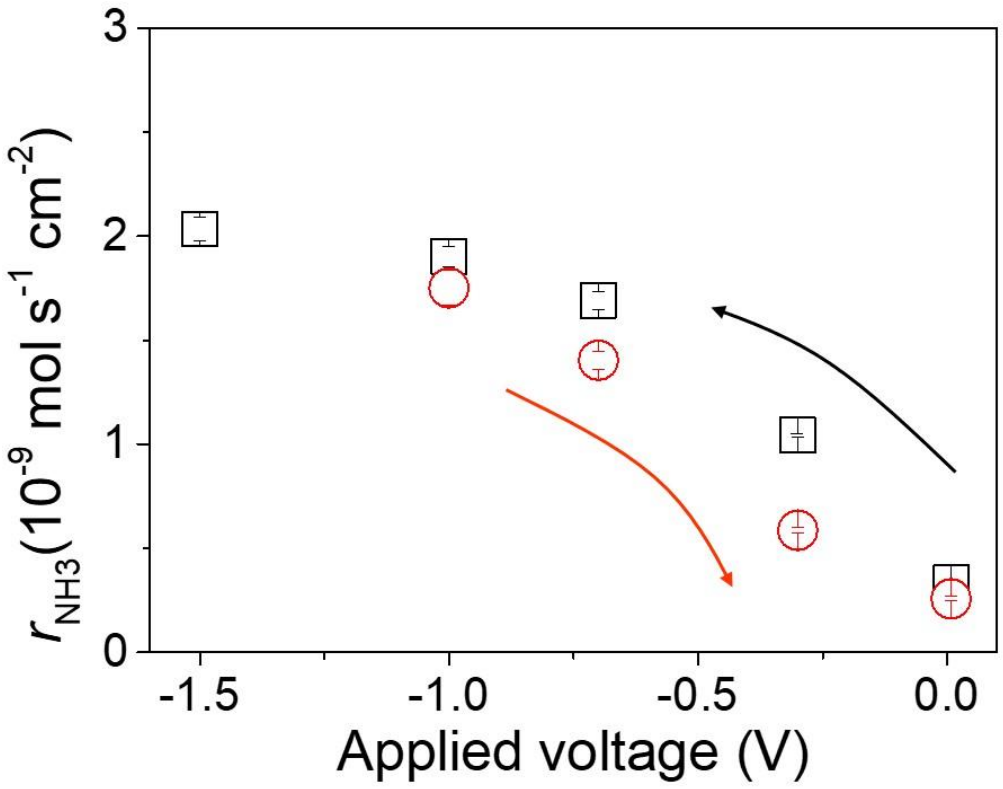

Fig. E Electrochemically reversible test using porous pure Fe cathode (30 μm) in 10% H_2–90% N_2 (40 sccm) at 550°C.

F. Stability for ammonia electrochemical synthesis

Experimental condition

Gas in the cathode: 10% H_2–90% N_2 with 40 sccm

Gas in the anode: wet 20% H_2–80% Ar with 30 sccm

Temperature: 550°C

Catalyst: porous pure Fe (15 μm)

To check the stability of porous pure Fe cathode, a stability test was performed at −1 V and 550°C, as shown in Fig. F. Although the current density decreased with elapsed time, a stable ammonia formation rate of around 1.7×10^{-9} mol cm^{-2} s^{-1} was obtained for 12 hours.

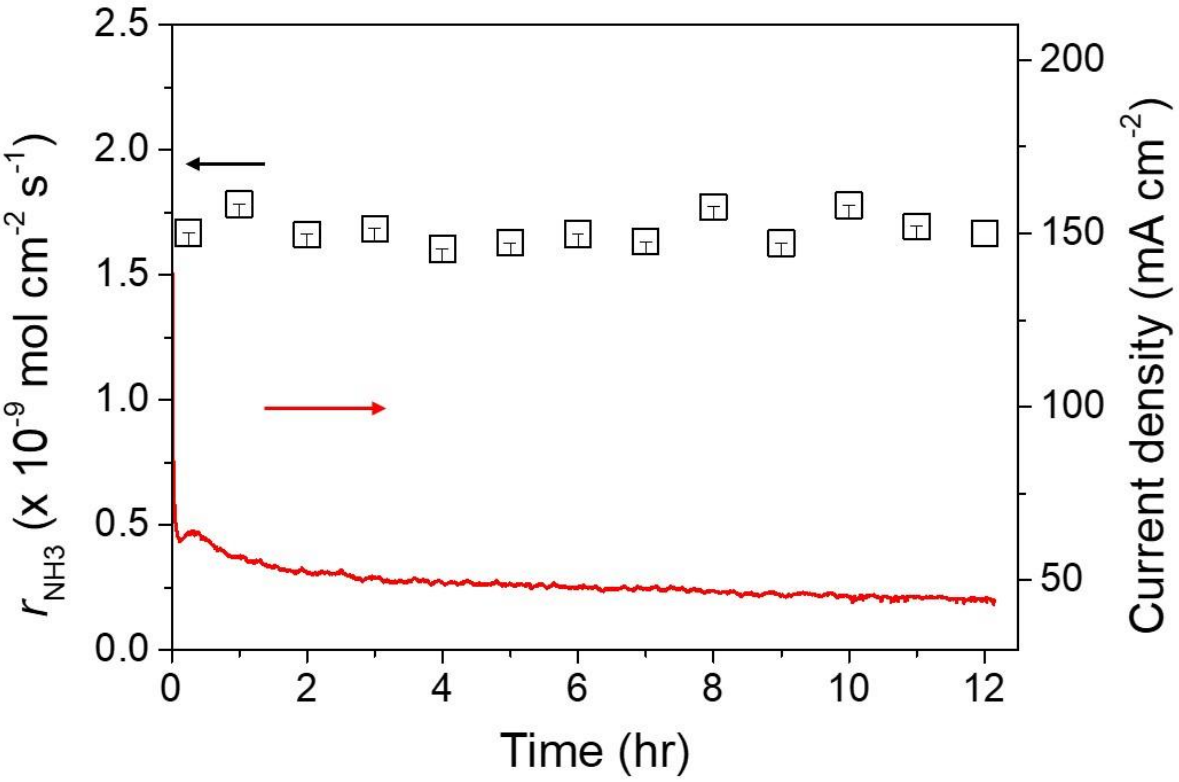

Fig. F Stability test using porous pure Fe in 10% H_2−90% N_2 at −1V and 550°C.

G. The current efficiency for hydrogen pumping

Experimental condition

Gas in the cathode: Ar with 40 sccm

Gas in the anode: wet 20% H_2–80% Ar with 30 sccm

Temperature: 550°C

Catalyst: porous pure Fe (15 μm)

To understand the hydrogen evolution reaction, a test was conducted in pure Ar at 550°C, as shown in Fig. G. When a voltage was applied, only the H_2 evolution reaction ($2H^+ + 2e^- \rightarrow H_2$) occurred. The current efficiencies for hydrogen evolution reaction were around 80–85% at electrode potentials between 0.085 V and 0.052 V (corresponding applied voltages between −0.2 V and −0.35 V). The main reason for the loss is probably caused by the leakage current, which is induced by hole and/or electron conduction through the electrolyte membrane.

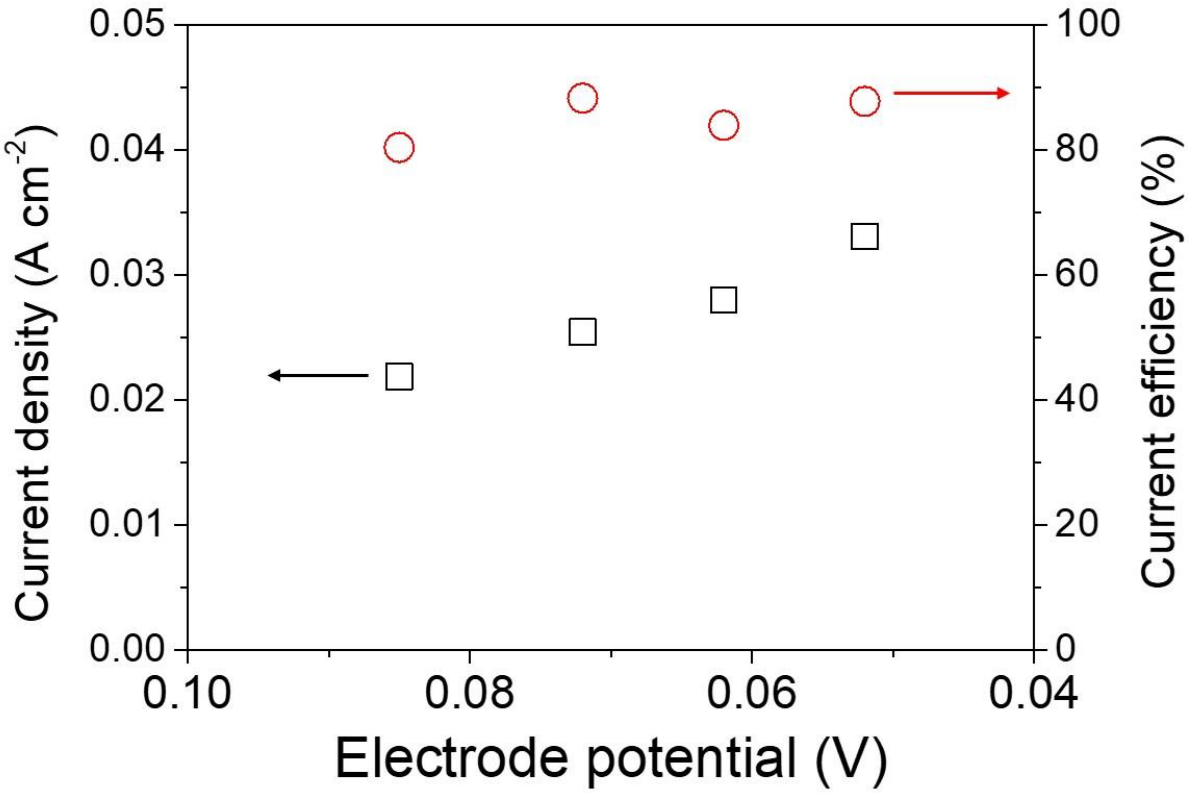

Fig. G Hydrogen pumping test using the cell of 20% H_2−80% Ar, Pt |BCY| Fe, Ar at 550°C.

H. Rotational-Vibrational states for $NH_{3-x}D_x$

The Eq. H-1 is used to calculate the rotational-vibrational energy levels, E. And the parameters for $NH_{3-x}D_x$ are shown in Table H-1 and Table H-2.[118-121]

$$E = v + 1/2(A+B)[J(J+1) - K^2] + CK^2 - D_J J^2(J+1)^2 - D_{JK} J(J+1)K^2 - D_K K^4 \quad \text{H-1}$$

Table H-1 Parameters for NH_3 and NH_2D.

	NH_3				NH_2D			
	Ground state		v_2 state		Ground state		v_2 state	
	Symmetry state	Asymmetry state	Symmetry state	Asymmetry state	Symmetry state	Asymmetry state	Symmetry state	Asymmetry state
v	0	0.793	932.434	968.122	0	0.406	876.374	896.562
A	9.947	9.9415	10.07	9.89	9.678	9.674	9.827	9.699
B	9.947	9.9415	10.07	9.89	6.411	6.41	6.408	6.359
C	6.227	6.228553	6.087	6.159	4.696	4.697	4.618	4.649
D_J	0.000849	0.000832	0.001131	0.000697	0.000527	0.000521	0.0006628	0.000466
D_{JK}	-0.001578	-0.00153	-0.00242	-0.00123	-0.0008	-0.0007852	-0.0010441	-0.0007
D_K	0.0010107	0.000979	0.001617	0.000811	0.000365	0.0003579	0.0004802	0.000311

Table H-2 Parameters for NHD_2 and ND_3.

	NHD_2				ND_3			
	Ground state		v_2 state		Ground state		v_2 state	
	Symmetry state	Asymmetry state	Symmetry state	Asymmetry state	Symmetry state	Asymmetry state	Symmetry state	Asymmetry state
v	0	0.171	810.227	819.565	0	0.053	745.597	749.1448
A	5.344	5.344	5.312	5.296	5.143	5.1428265	5.224	5.216
B	7.446	7.445	7.529	7.48	5.143	5.1428265	5.224	5.216
C	3.753	3.753	3.705	3.718	3.124	3.12408768	3.088	3.094
D_J	0.000332	0.0003304	0.0003766	0.000312	0.000197	0.00019651	0.0002306	0.000219
D_{JK}	-0.00045	-0.0004463	-0.0006086	-0.00043	-0.00035	-0.00034794	-0.0004162	-0.00038
D_K	0.000157	0.000156	0.0003079	0.000187	0	-6.3944E-07	-0.0000382	0.000008

Table H-3−Table H-6 show Q, P, and R branches for $NH_{3-x}D_x$ ν_2 state. i, and i' (i=R, P, and Q) represented the energy from symmetric state to asymmetric state and from asymmetric state to symmetric state, respectively.

Table H-3 Q, Q', P, P', R and R' branches for NH_3 ν_2 state

R branch at $K = 0$ (cm^{-1})			P branch at $K = 0$ (cm^{-1})			Q branch (cm^{-1})		
J	R	R'	J	P	P'	J	Q	Q'
0	987.8992	951.7765	1	948.2314	911.7613	1	967.9971	931.6279
1	1007.546	972.1406	2	928.2478	892.1574	2	967.7364	931.3322
2	1027.05	993.4597	3	908.1952	872.8421	3	967.3398	930.754
3	1046.401	1013.41	4	888.1012	853.821	4	966.8076	929.8922
4	1065.594	1034.226	5	867.9973	835.0926	5	966.1401	928.7447
5	1084.627	1055.09	6	847.9183	816.6481	6	965.3378	927.3083

Table H-4 Q, Q', P, P', R and R' branches for NH_2D ν_2 state

R branch at $K = 0$ (cm^{-1})			P branch at $K = 0$ (cm^{-1})			Q branch (cm^{-1})		
J	R	R'	J	P	P'	J	Q	Q'
0	912.6181	892.2003	1	880.4751	859.8861	1	896.4996	875.9643
1	928.6323	908.5672	2	864.3701	843.9671	2	896.3436	875.8022
2	944.5949	925.4405	3	848.2611	828.2202	3	896.0947	875.4811
3	960.4975	941.6239	4	832.1638	812.651	4	895.7539	875.0008
4	976.3333	958.2649	5	816.0951	797.2618	5	895.3223	874.3606
5	992.0972	974.9427	6	800.0736	782.0515	6	894.8016	873.5598

Table H-5 Q, Q', P, P', R and R' branches for NHD_2 ν_2 state

R branch at $K = 0$ (cm^{-1})			P branch at $K = 0$ (cm^{-1})			Q branch (cm^{-1})		
J	R	R'	J	P	P'	J	Q	Q'
0	832.3398	822.8955	1	806.7763	797.2683	1	819.523	810.034
1	845.0931	835.7778	2	793.9817	784.5404	2	819.4108	809.9158
2	857.818	848.8607	3	781.1895	771.879	3	819.2275	809.7006
3	870.5078	861.6289	4	768.4088	759.2899	4	818.9716	809.3866

4	883.1566	874.5742	5	755.6488	746.7777	5	818.6408	808.9712
5	895.7586	887.515	6	742.9193	734.3459	6	818.2323	808.451

Table H-6 Q, Q', P, P', R and R' branches for ND_3 ν_2 state

R branch at K = 0 (cm^{-1})			P branch at K= 0 (cm^{-1})			Q branch (cm^{-1})		
J	R	R'	J	P	P'	J	Q	Q'
0	759.5759	755.9911	1	738.8596	735.2591	1	749.1878	745.5891
1	770.1477	766.5948	2	728.725	725.1412	2	749.1706	745.563
2	780.8544	777.4009	3	718.7453	715.1941	3	749.0931	745.4682
3	791.6896	788.2461	4	708.924	705.4209	4	748.9552	745.3091
4	802.6466	799.2785	5	699.2644	695.8238	5	748.7566	745.0917
5	813.718	810.4373	6	689.769	686.4044	6	748.4972	744.8236

I. H^+ or (D^+) cations diffusion through BCY electrolyte at rest potential

The proton diffusion from the anode to the cathode by the driving force of a H_2 concentration gradient. Here, Fick's first law and Fick's second law are considered, which are described by Eqs. I-1−I-2. The boundary conditions are a fixed concentration of 10% H_2 at the anode boundary and a fixed concentration of 0 % H_2 at the cathode boundary. At the steady state, the term of $\frac{\partial c_{H2}}{\partial t}$ should be zero. Therefore, J_H is a constant at the steady state, which can be obtained by Eq. I-3.

$$J_H = -D_H \frac{\partial c_{H2}}{\partial x} \quad \text{I-1}$$

$$\frac{\partial c_{H2}}{\partial t} = D_H \frac{\partial^2 c_{H2}}{\partial x^2} \quad \text{I-2}$$

$$J_H = -D_H \frac{c_{H2,anode} - c_{H2,cathode}}{L} \quad \text{I-3}$$

where D_H, c_{H2}, $c_{H2,anode}$, $c_{H2,cathode}$, and L are the diffusion coefficient for H^+ in BCY, H_2 concentration, H_2 concentration in the anode, H_2 concentration in the cathode, and the thickness of BCY electrolyte, respectively. For the operation condition of 10% H_2−90% Ar in the anode and 5% D_2−45% Ar−50% N_2, the parameters were summarized in Table I-1. J_H is about 1.86×10^{-10} mol cm^{-2} s^{-1}. The H_2 partial pressure, p_{H2}, in the cathode was obtained by Eq. I-4.

$$p_{H2} = \frac{J_H ART}{f} \quad \text{I-4}$$

where A, R, T, and f are the electrode area, gas constant, temperature, and flow rate.

$$D_D = \frac{D_H}{\sqrt{2}} \quad \text{I-5}$$

The same as calculation was conducted tor the operation condition of 10% D_2−90% Ar in the anode and 5% H_2−95% N_2. The diffusion coefficient for deuterium in BCY, D_D, was described by Eq. I-5. The parameters were summarized in Table I-2. J_D is about 1.31×10^{-10} mol cm^{-2} s^{-1}. The D_2 partial pressure in the cathode, p_{D2}, was also obtained by Eq. I-3.

Table I-1 Parameters for calculation the H^+ flux

D_H (m^2 s^{-1})	$c_{H2,\ anode}$ (mol l^{-1})	$c_{H2,cathode}$ (mol l^{-1})	L (mm)
1.0×10^{-9}	0.00148	0	0.08

Table I-2 Parameters for calculation the D^+ flux

D_D (m^2 s^{-1})[122]	$c_{D2,\ anode}$ (mol l^{-1})	$c_{D2,cathode}$ (mol l^{-1})	L (mm)
7.1×10^{-10}	0.00148	0	0.08

J. Fe–YSZ cermet working electrode (cathode) preparation

J.A. Preparation for 10Fe-YSZ cathode on YSZ electrolyte

Fe−YSZ electrode on YSZ electrolyte was fabricated by the doctor-blade method. The steps were described as below:

1. YSZ powder was mixed with the slurry in section 2.2.2.
2. The mixed slurry was pasted onto the YSZ electrolyte and calcined at 1300°C in air to obtain a porous pure YSZ cathode.
3. $Fe(NO_3)_3 \cdot 9H_2O$ was stoichiometrically dissolved in water to form a 0.5M iron nitrate solution.
4. The mixture solution was poured onto the YSZ porous cathode and dried at 80°C for 5 mins.
5. The sample was annealed at 500°C in air.
6. Repeat steps 4-5 to obtain 10 wt.% Fe.
7. The sample was annealed at 900°C in 3% H_2−97% Ar to obtain the 10 wt.%Fe–YSZ (10Fe−YSZ).

J.B. The performances of the electrochemical ammonia synthesis using Fe–YSZ cathode

Experimental condition

Gas in the cathode: 10% H_2–90% N_2 with 20 sccm

Gas in the anode: wet 20% H_2–80% Ar with 30 sccm

Temperature: 550−700°C

Fig. J-1 shows a schematic image of the structure of 10Fe−YSZ cathode. Fig. J-2 shows the XRD spectra of 10Fe−YSZ. Fig. J-3 shows that 10Fe–YSZ cathode exhibited a low ammonia formation rate (5×10^{-11} mol s^{-1} cm^{-2}). Based on Eq. 2-1, the electrode potential in 10Fe–YSZ is closed to the applied voltage because of a low value of current multiplied by ohmic resistance. Therefore, proton supply from the anode plays an important role in the electrochemical reaction of ammonia synthesis.

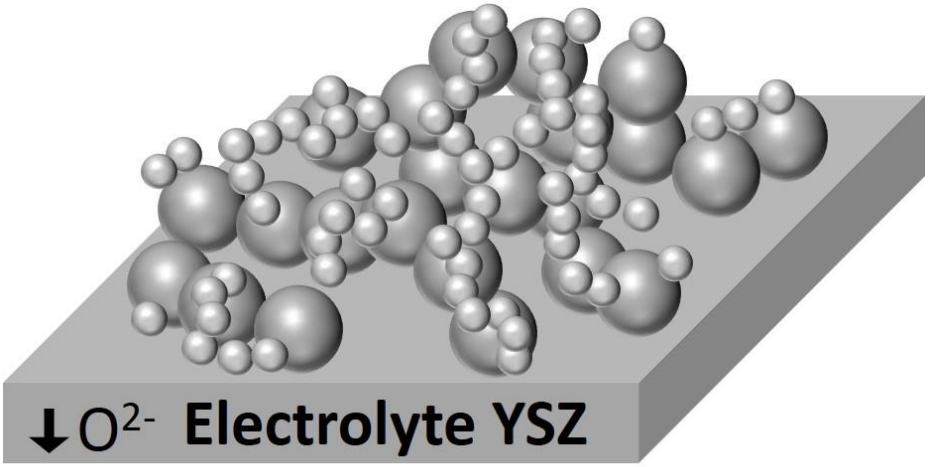

Fig. J-1 Schematic image of cathode structures of Fe−YSZ cathode.

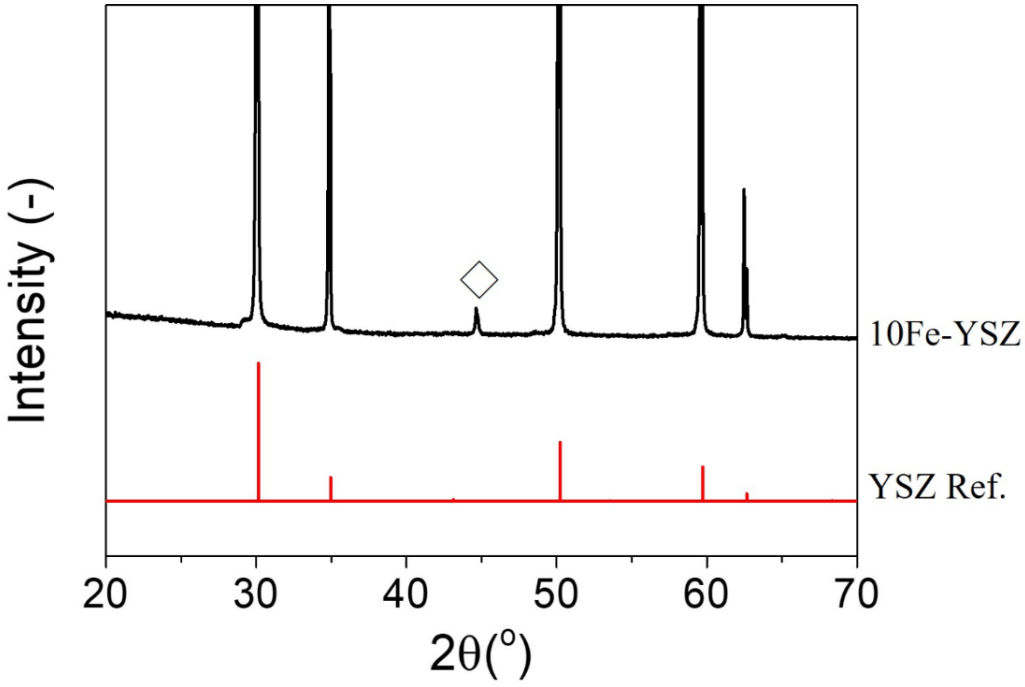

Fig. J-2 XRD spectra of 10Fe–YSZ cathode on YSZ electrolyte.

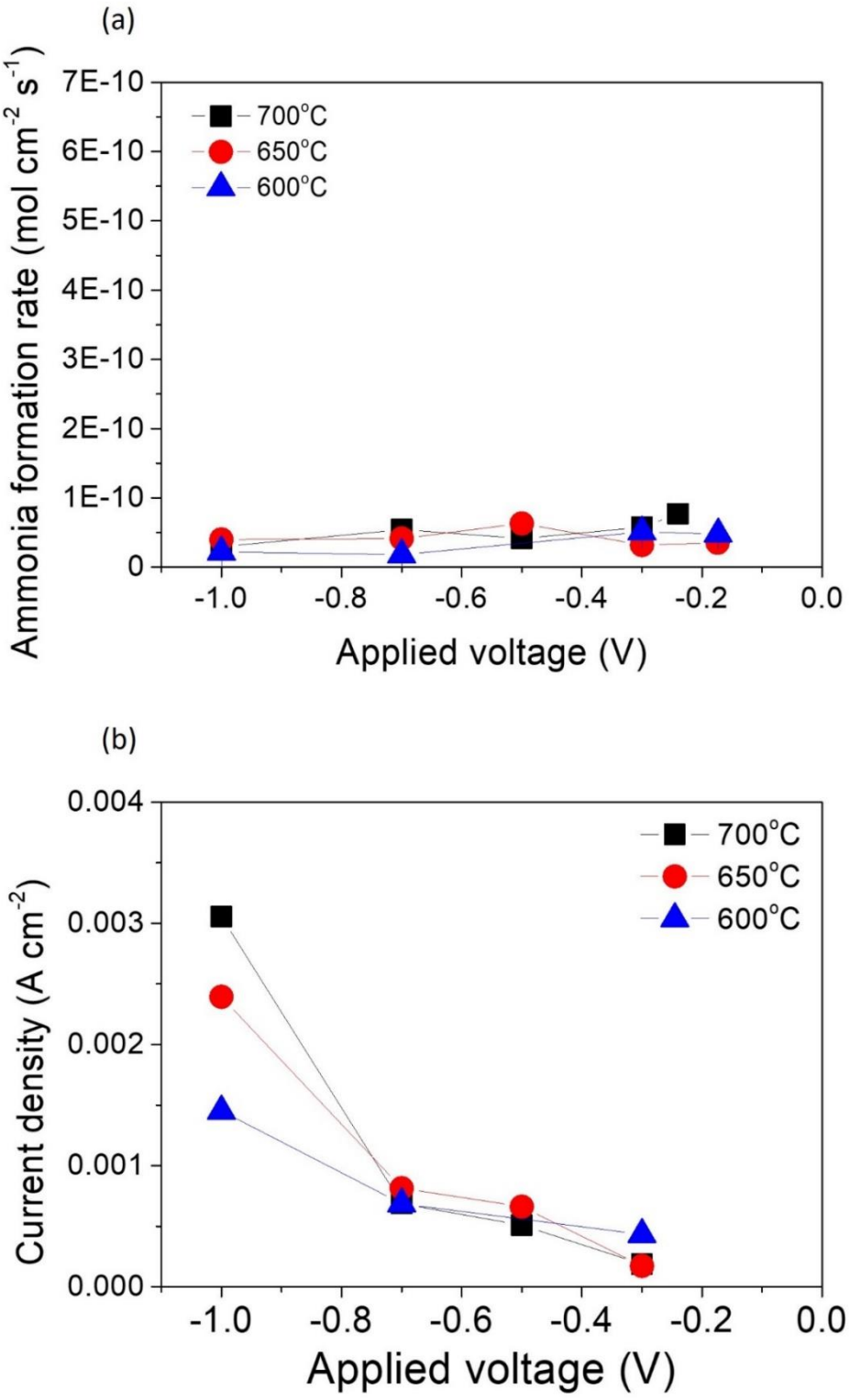

.

Fig. J-3 (a) ammonia formation rate and (b) current density for 10Fe−YSZ at different temperatures.

References

1. J. W. Erisman, M. A. Sutton, J. Galloway, Z. Klimont and W. Winiwarter, *Nature Geoscience*, 2008, **1**, 636.
2. I. P. o. C. Change, *Global warming of 1.5°C*, 2018.
3. I. R. E. Agency, *<IRENA_Renewable_energy_statistics_2019.pdf>*, 2019.
4. M. Cimenti and J. Hill, *Energies*, 2009, **2**, 377-410.
5. *Fuel Cells Bulletin*, 2020, **2020**, 5-6.
6. C. Smith, A. K. Hill and L. Torrente-Murciano, *Energy & Environmental Science*, 2020, **13**, 331-344.
7. M. Appl, *Ammonia: Principles and Industrial Practice*, 2007.
8. H. Liu, *Ammonia synthesis catalysts : innovation and practice*, World Scientific, Singapore, 2013.
9. J. A. Dumesic and A. A. Trevino, *Journal of Catalysis*, 1989, **116**, 119-129.
10. B. Fastrup, *Journal of Catalysis*, 1997, **168**, 235-244.
11. Y. Bicer, I. Dincer, C. Zamfirescu, G. Vezina and F. Raso, *Journal of Cleaner Production*, 2016, **135**, 1379-1395.
12. *Sustainable Ammonia Synthesis*, 2016.
13. G. Marnellos and M. Stoukides, *Science*, 1998, **282**, 98.
14. X. Lu, T. M. M. Heenan, J. J. Bailey, T. Li, K. Li, D. J. L. Brett and P. R. Shearing, *Journal of Power Sources*, 2017, **365**, 210-219.
15. E. Skulason, T. Bligaard, S. Gudmundsdottir, F. Studt, J. Rossmeisl, F. Abild-Pedersen, T. Vegge, H. Jonsson and J. K. Norskov, *Physical chemistry chemical physics : PCCP*, 2012, **14**, 1235-1245.
16. S. Back and Y. Jung, *Physical chemistry chemical physics : PCCP*, 2016, **18**, 9161-9166.
17. D. Bao, Q. Zhang, F. L. Meng, H. X. Zhong, M. M. Shi, Y. Zhang, J. M. Yan, Q. Jiang and X. B. Zhang, *Advanced materials*, 2017, **29**.
18. J. Wang, L. Yu, L. Hu, G. Chen, H. Xin and X. Feng, *Nature communications*, 2018, **9**, 1795.
19. H.-M. Liu, S.-H. Han, Yue-Zhao, Y.-Y. Zhu, X.-L. Tian, J.-H. Zeng, Jia-Xing, Jiang, B. Y. Xia⋆bc, Y. Chen⋆a and *Journal of Materials Chemistry A* 2018, **6**, 3211.

20. S. Mukherjee, D. A. Cullen, S. Karakalos, K. Liu, H. Zhang, S. Zhao, H. Xu, K. L. More, G. Wang and G. Wu, *Nano Energy*, 2018, **48**, 217-226.
21. Y. Song, D. Johnson, R. Peng, D. K. Hensley, P. V. Bonnesen, L. Liang, J. Huang, F. Yang, F. Zhang, R. Qiao, A. P. Baddorf, T. J. Tschaplinski, N. L. Engle, M. C. Hatzell, Z. Wu, D. A. Cullen, H. M. M. III, B. G. Sumpter and A. J. Rondinone, *science Advances*, 2018, **4**, e1700336.
22. C. Lv, C. Yan, G. Chen, Y. Ding, J. Sun, Y. Zhou and G. Yu, *Angewandte Chemie International Edition* 2018, **57**, 6073.
23. S. J. Li, D. Bao, M. M. Shi, B. R. Wulan, J. M. Yan and Q. Jiang, *Advanced materials*, 2017, **29**.
24. X. Zhang, R. M. Kong, H. Du, L. Xia and F. Qu, *Chem Commun (Camb)*, 2018, **54**, 5323-5325.
25. L. Zhang, X. Ji, X. Ren, Y. Ma, X. Shi, Z. Tian, A. M. Asiri, L. Chen, B. Tang and X. Sun, *Advanced materials*, 2018, **30**, e1800191.
26. D. Wang, L. M. Azofra, M. Harb, L. Cavallo, X. Zhang, B. H. R. Suryanto and D. R. MacFarlane, *ChemSusChem*, 2018, **11**, 3416-3422.
27. G. F. Chen, X. Cao, S. Wu, X. Zeng, L. X. Ding, M. Zhu and H. Wang, *Journal of the American Chemical Society*, 2017, **139**, 9771-9774.
28. H. Cheng, L. X. Ding, G. F. Chen, L. Zhang, J. Xue and H. Wang, *Advanced materials*, 2018, **30**, e1803694.
29. X. Xiang, Z. Wang, X. Shi, M. Fan and X. Sun, *ChemCatChem*, 2018, **10**.
30. Y. Liu, Y. Su, X. Quan, X. Fan, S. Chen, H. Yu, H. Zhao, Y. Zhang and J. Zhao, *ACS Catalysis*, 2018, **8**, 1186.
31. D. Yang, T. Chen and Z. Wang, *Journal of Materials Chemistry A*, 2017, **5**, 18967.
32. X. Wang, W. Wang, M. Qiao, G. Wu, W. Chen, T. Yuan, Q. Xu, M. Chen, Y. Zhang, X. Wang, J. Wang, J. Ge, X. Hong, Y. Li, Y. Wu and Y. Li, *Science Bulletin*, 2018, **63**, 1246-1253.
33. M. M. Shi, D. Bao, B. R. Wulan, Y. H. Li, Y. F. Zhang, J. M. Yan and Q. Jiang, *Advanced materials*, 2017, **29**.
34. R. Zhang, Y. Zhang, X. Ren, G. Cui, A. M. Asiri, B. Zheng and X. Sun, *ACS Sustainable Chemistry & Engineering*, 2018, **6**, 9545-9549.

35. W. Qiu, X. Y. Xie, J. Qiu, W. H. Fang, R. Liang, X. Ren, X. Ji, G. Cui, A. M. Asiri, G. Cui, B. Tang and X. Sun, *Nature communications*, 2018, **9**, 3485.
36. H. Wang, L. Wang, Q. Wang, S. Ye, W. Sun, Y. Shao, Z. Jiang, Q. Qiao, Y. Zhu, P. Song, D. Li, L. He, X. Zhang, J. Yuan, T. Wu and G. A. Ozin, *Angewandte Chemie International Edition*, 2018, **17**, 12360.
37. J. Han, Z. Liu, Y. Ma, G. Cui, F. Xie, F. Wang, Y. Wu, S. Gao, Y. Xu and X. Sun, *Nano Energy*, 2018, **52**, 264-270.
38. W. Guo, Z. Liang, J. Zhao, B. Zhu, K. Cai, R. Zou and Q. Xu, *Small Methods*, 2018, **2**, 1800204.
39. X. Cui, C. Tang, X. M. Liu, C. Wang, W. Ma and Q. Zhang, *Chemistry*, 2018, **24**, 18494-18501.
40. M. A. Shipman and M. D. Symes, *Electrochimica Acta*, 2017, **258**, 618-622.
41. F. Zhou, L. M. Azofra, M. Ali, M. Kar, A. N. Simonov, C. McDonnell-Worth, C. Sun, X. Zhang and D. R. MacFarlane, *Energy & Environmental Science*, 2017, **10**, 2516.
42. K. Kim, N. Lee, C.-Y. Yoo, J.-N. Kim, H. C. Yoon and J.-I. Han, *Journal of The Electrochemical Society*, 2016, **163**, F610-F612.
43. K. Kim, C.-Y. Yoo, J.-N. Kim, H. C. Yoon and J.-I. Han, *Journal of The Electrochemical Society*, 2016, **163**, F1523-F1526.
44. B. H. R. Suryanto, C. S. M. Kang, D. Wang, C. Xiao, F. Zhou, L. M. Azofra, L. Cavallo, X. Zhang and D. R. MacFarlane, *ACS Energy Letters*, 2018, **3**, 1219-1224.
45. X. Zhao, F. Yin, N. Liu, G. Li, T. Fan and B. Chen, *Journal of Materials Science*, 2017, **52**, 10175-10185.
46. S. Chen, S. Perathoner, C. Ampelli, C. Mebrahtu, D. Su and G. Centi, *Angewandte Chemie*, 2017, **56**, 2699-2703.
47. J. Kong, A. Lim, C. Yoon, J. H. Jang, H. C. Ham, J. Han, S. Nam, D. Kim, Y.-E. Sung, J. Choi and H. S. Park, *ACS Sustainable Chemistry & Engineering*, 2017, **5**, 10986-10995.
48. X. Yang, J. Nash, J. Anibal, M. Dunwell, S. Kattel, E. Stavitski, K. Attenkofer, J. G. Chen, Y. Yan and B. Xu, *Journal of the American Chemical Society*, 2018, **140**, 13387-13391.
49. Z. Zhang, Z. Zhong and R. Liu, *Journal of Rare Earths*, 2010, **28**, 556-559.
50. S. Chen, S. Perathoner, C. Ampelli, C. Mebrahtu, D. Su and G. Centi, *ACS Sustainable Chemistry & Engineering*, 2017, **5**, 7393-7400.

51. Y. Yao, J. Wang, U. B. Shahid, M. Gu, H. Wang, H. Li and M. Shao, *Electrochemical Energy Reviews*, 2020, **3**, 239-270.
52. K. Kim, C.-Y. Yoo, J.-N. Kim, H. C. Yoon and J.-I. Han, *Korean Journal of Chemical Engineering*, 2016, **33**, 1777-1780.
53. Y. Bicer and I. Dincer, *International Journal of Energy Research*, 2017, **41**, 1987-2000.
54. B. Cui, J. Zhang, S. Liu, X. Liu, W. Xiang, L. Liu, H. Xin, M. J. Lefler and S. Licht, *Green Chemistry*, 2017, **19**, 298-304.
55. Y. Bicer and I. Dincer, *Journal of The Electrochemical Society*, 2017, **164**, H5036-H5042.
56. F. F. Li and S. Licht, *Inorganic chemistry*, 2014, **53**, 10042-10044.
57. G. Qing, R. Kikuchi, S. Kishira, A. Takagaki, T. Sugawara and S. T. Oyama, *Journal of The Electrochemical Society*, 2016, **163**, E282-E287.
58. K. Imamura and J. Kubota, *Sustainable Energy & Fuels*, 2019, **3**, 1406-1417.
59. K. Imamura, M. Matsuyama and J. Kubota, *ChemistrySelect*, 2017, **2**, 11100-11103.
60. K. Imamura and J. Kubota, *Sustainable Energy & Fuels*, 2018, **2**, 1278.
61. S. Kishira, G. Qing, S. Suzu, R. Kikuchi, A. Takagaki and S. T. Oyama, *International Journal of Hydrogen Energy*, 2017, **42**, 26843-26854.
62. M. Ouzounidou, A. Skodra, C. Kokkofitis and M. Stoukides, *Solid State Ionics*, 2007, **178**, 153-159.
63. Z. Li, R. Liu, Y. Xie, S. Feng and J. Wang, *Solid State Ionics*, 2005, **176**, 1063-1066.
64. Y. Xie, J.-D. Wang, R.-Q. Liu, X.-T. Su, Z.-P. Sun and Z.-J. Li, *Solid State Ionics*, 2004, **168**, 117-121.
65. M. Zhang, J. Xu and G. Ma, *Journal of Materials Science*, 2011, **46**, 4690-4694.
66. F. Zhang, Q. Yang, B. Pan, R. Xu, H. Wang and G. Ma, *Materials Letters*, 2007, **61**, 4144-4148.
67. J.-D. Wang, Y.-H. Xie, Z.-F. Zhang, R.-Q. Liu and Z.-J. Li, *Materials Research Bulletin*, 2005, **40**, 1294-1302.
68. A. Skodra and M. Stoukides, *Solid State Ionics*, 2009, **180**, 1332-1336.
69. W. B. Wang, X. B. Cao, W. J. Gao, F. Zhang, H. T. Wang and G. L. Ma, *Journal of Membrane Science*, 2010, **360**, 397-403.
70. E. Vasileiou, V. Kyriakou, I. Garagounis, A. Vourros and M. Stoukides, *Solid State Ionics*, 2015, **275**, 110-116.

71. D. S. Yun, J. H. Joo, J. H. Yu, H. C. Yoon, J.-N. Kim and C.-Y. Yoo, *Journal of Power Sources*, 2015, **284**, 245-251.
72. E. Vasileiou, V. Kyriakou, I. Garagounis, A. Vourros, A. Manerbino, W. G. Coors and M. Stoukides, *Topics in Catalysis*, 2015, **58**, 1193-1201.
73. J. Otomo, N. Noda and F. Kosaka, *ECS Transactions*, 2015, **68**, 2663.
74. F. Kosaka, T. Nakamura, A. Oikawa and J. Otomo, *ACS Sustainable Chemistry & Engineering*, 2017, **5**, 10439-10446.
75. F. Kosaka, T. Nakamura and J. Otomo, *Journal of The Electrochemical Society*, 2017, **164**, F1323-F1330.
76. E. Vasileiou, V. Kyriakou, I. Garagounis, A. Vourros, A. Manerbino, W. G. Coors and M. Stoukides, *Solid State Ionics*, 2016, **288**, 357-362.
77. F. Kosaka, N. Noda, T. Nakamura and J. Otomo, *Journal of Materials Science*, 2016, **52**, 2825-2835.
78. N. SHIMODA, Y. KOBAYASHI, Y. KIMURA, G. NAKAGAWA and S. SATOKAWA, *Journal of the Ceramic Society of Japan*, 2017, **125**, 252.
79. Z. Li, R. Liu, J. Wang, Z. Xu, Y. Xie and B. Wang, *Science and Technology of Advanced Materials*, 2016, **8**, 566-570.
80. Y. Guo, B. Liu, Q. Yang, C. Chen, W. Wang and G. Ma, *Electrochemistry Communications*, 2009, **11**, 153-156.
81. R. Liu, Y. Xie, J. Wang, Z. Li and B. Wang, *Solid State Ionics*, 2006, **177**, 73-76.
82. J. Liu, Y. Li, W. Wang, H. Wang, F. Zhang and G. Ma, *Journal of Materials Science*, 2010, **45**, 5860-5864.
83. W. B. Wang, J. W. Liu, Y. D. Li, H. T. Wang, F. Zhang and G. L. Ma, *Solid State Ionics*, 2010, **181**, 667-671.
84. C. Chen and G. Ma, *Journal of Alloys and Compounds*, 2009, **485**, 69-72.
85. J. Díez-Ramírez, V. Kyriakou, I. Garagounis, A. Vourros, E. Vasileiou, P. Sánchez, F. Dorado and M. Stoukides, *ACS Sustainable Chemistry & Engineering*, 2017, **5**, 8844-8851.
86. C. G. Vayenas, S. Bebelis and S. Ladas, *Nature*, 1990, **343**, 625-627.
87. D. Tsiplakides and C. G. Vayenas, *Journal of The Electrochemical Society*, 2001, **148**, E189-E202.
88. C. G. Vayenas and S. Brosda, *Topics in Catalysis*, 2014, **57**, 1287-1301.

89. J. N. Renner, L. F. Greenlee, A. M. Herring and K. E. Ayers, *The Electrochemical Society Interface*, 2015, **24**, 51-57.
90. T. Murakami, T. Nishikiori, T. Nohira and Y. Ito, *Journal of The Electrochemical Society*, 2005, **152**, D75.
91. I. A. Amar, C. T. G. Petit, L. Zhang, R. Lan, P. J. Skabara and S. Tao, *Solid State Ionics*, 2011, **201**, 94-100.
92. I. A. Amar, R. Lan, C. T. G. Petit, V. Arrighi and S. Tao, *Solid State Ionics*, 2011, **182**, 133-138.
93. R. Lan, K. A. Alkhazmi, I. A. Amar and S. Tao, *Electrochimica Acta*, 2014, **123**, 582-587.
94. I. A. Amar, C. T. G. Petit, G. Mann, R. Lan, P. J. Skabara and S. Tao, *International Journal of Hydrogen Energy*, 2014, **39**, 4322-4330.
95. I. A. Amar, R. Lan and S. Tao, *Journal of The Electrochemical Society*, 2014, **161**, H350-H354.
96. I. A. Amar, C. T. G. Petit, R. Lan, G. Mann and S. Tao, *RSC Adv.*, 2014, **4**, 18749-18754.
97. R. Lan, K. A. Alkhazmi, I. A. Amar and S. Tao, *Applied Catalysis B: Environmental*, 2014, **152-153**, 212-217.
98. R. Lan, K. A. Alkhazmi, I. A. Amar and S. Tao, *Faraday discussions*, 2015, **182**, 353-363.
99. I. A. Amar, R. Lan, C. T. G. Petit and S. Tao, *Electrocatalysis*, 2014, **6**, 286-294.
100. S. Licht, B. Cui, B. Wang, F. F. Li, J. Lau and S. Liu, *Science*, 2014, **345**, 637-640.
101. I. A. Amar, R. Lan, C. T. G. Petit and S. Tao, *International Journal of Electrochemcal Science*, 2015, **10**, 3757.
102. Z.-J. Li, R.-Q. Liu, J.-D. Wang, Y.-H. Xie and F. Yue, *Journal of Solid State Electrochemistry*, 2004, **9**, 201-204.
103. B. H. Wang, J. D. Wang, R. Liu, Y. H. Xie and Z. J. Li, *Journal of Solid State Electrochemistry*, 2005, **11**, 27-31.
104. C. Chen and G. Ma, *Journal of Materials Science*, 2008, **43**, 5109-5114.
105. J. K. Nørskov, T. Bligaard, A. Logadottir, J. R. Kitchin, J. G. Chen, S. Pandelov and U. Stimming, *Journal of The Electrochemical Society*, 2005, **152**, J23.
106. K.-I. Aika and A. Ozaki, *Journal of Catalysis*, 1969, **13**, 232-237.
107. K.-i. A. Ryoichi Kojima, *Applied Catalysis A: General*, 2001, **218**, 121.

108. S. Hagen, R. Barfod, R. Fehrmann, C. J. J. Jacobsen, H. T. Tenuissen and I. Chorkendorff, *Journal of Catalysis*, 2003, **214**, 327-335.
109. C. W. David, *Journal of Chemical Education*, 1996, **73**.
110. G. Laroche, J. Vallade, R. Bazinette, P. v. Nijnatten, E. Hernandez, G. Hernandez and F. Massines, *Review of Scientific Instruments*, 2012, **83**.
111. A. J. Bard and L. R. Faulker, *Electrochemical Methods: Fundamentals and Applications*, Wiley, 2000.
112. J. Huang, T. Zhou, J. Zhang and M. Eikerling, *The Journal of Chemical Physics*, 2018, **148**, 044704.
113. A. D. Frantzis, S. Bebelis and C. G. Vayenas, *Solid State Ionics*, 2000, **136-137**, 863-872.
114. A. Palermo, R. M. Lambert, I. R. Harkness, I. V. Yentekakis, O. Mar'ina and C. G.Vayenas, *Journal of Catalysis*, 1996, **161**, 471-479.
115. C. G. Vayenas, *Catalysis Letters*, 2013, **143**, 1085-1097.
116. *NIST Chemistry WebBook, NIST Standard Reference Database Number 69,*, National Institute of Standards and Technology, 2021.
117. D. R. Strongin and G. A. Somorijai, *Journal of Catalysis*, 1988, **109**, 51-60.
118. V. A. Job, S. B. Kartha, K. Singh and V. B. Kartha, *Journal of Molecular Spectroscopy*, 1987, **126**, 290-306.
119. V. A. Job, S. B. Kartha, V. B. Kartha and K. B. Thakur, *Journal of Molecular Spectroscopy*, 1986, **120**, 205-218.
120. S. B. Kartha, K. Singh, V. A. Job and V. B. Kartha, *Journal of Molecular Spectroscopy*, 1988, **129**, 86-98.
121. Š. Urban, D. Papoušek, J. Kauppinen, K. Yamada and G. Winnewisser, *101*, 1983.
122. S. Zhuang, N. Han, Q. Zou, S. Zhang and F. Song, *Membranes*, 2020, **10**, 164.

Acknowledgements

I would like to take this opportunity to thank many people who have offered invaluable assistance during these five years.

First and foremost, I greatly appreciate Associate Professor Otomo, my supervisor, who guided my thesis, for his teaching, concern, and help. Although the research in the first year was failed, Otomo Professor recommended another topic of ammonia synthesis and gave critical comments, constant encouragement, and guidance to encourage me. Without his patient and careful instruction, this thesis could not have reached its present stage.

Second, I would like to thank Professor Oshima, Professor Tabeta, Professor Tonokura, Associate Professor Kikuchi, and Assistant Akizuki, for attending my preliminary examination. Professor Oshima points out the problem of presentation structure and the reliability of estimation of ammonia formation rate at high operating pressure. Professor Tonokura gives some advice about ammonia adsorption on gas tubing in FTIR measurement. Associate Professor Kikuchi gives a comment on Fe catalyst stability in the electrochemical reaction. Professor Tabeta suggests that how to discuss and extend from the experiment results to reactor design for practical implementation. Assistant Akiziku suggests the reaction mechanism of electrochemical ammonia formation. I am deeply grateful to all Professors for pointing out my problems to make this thesis better.

I also want to appreciate the assistance from Technical Staff Hamane for helping SEM and TEM analysis, and from Dr. Yajima for and instruction in XRD from the Materials Design and Characterization Laboratory, Institute for Solid State Physics, The University of Tokyo.

I am also grateful to the member in Otomo lab. Dr. Kosaka, who is working in AIST now, gave instructions in sputter and HPLC. Dr. Matsuo helped to contact Associate Professor Inoue in Nippon Medical school for TEM analysis. I also thank the ammonia group members, Mr. Nakamura, Mr. Oikawa, Mr. Hasegawa, Mr. Yamamoto, and Mr. Fukuda, for discussing my data with me.

Finally, I would like to appreciate my parents for their continuous support and encouragement.